Volume 1 Issue 3, September 2022
ISSN: 2810-9635 (Online)

Materials Science in Additive Manufacturing

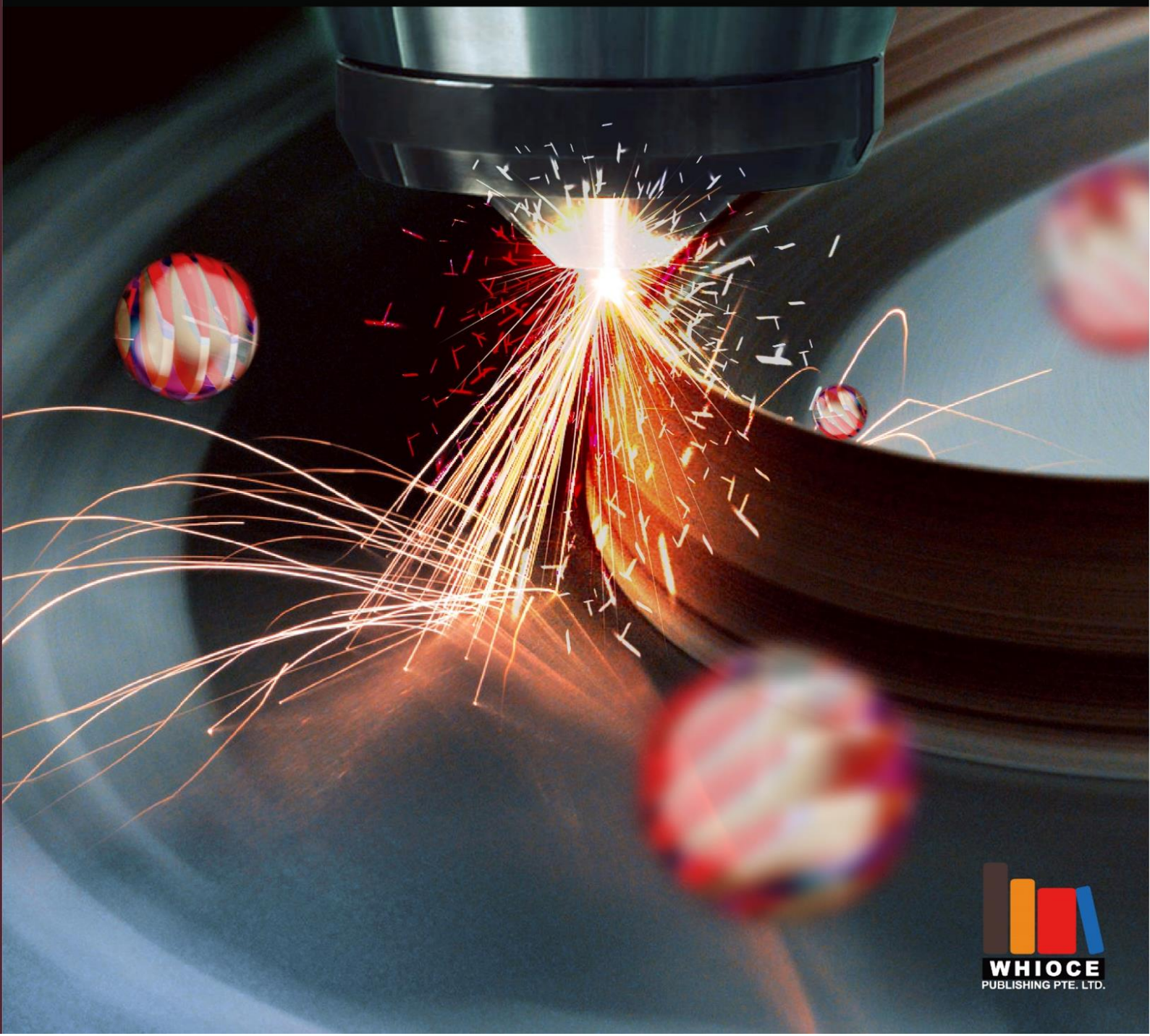

WHIOCE PUBLISHING PTE. LTD.

Materials Science in Additive Manufacturing

Online ISSN: 2810-9635

Materials Science in Additive Manufacturing aims to bridge the cutting-edge research between additive manufacturing and the entire spectrum of materials science. The journal covers all applied and fundamentals of processing, synthesis, structure, composition, properties and performance of materials designed or manipulated for additive manufacturing. The journal covers a wide scope of innovative techniques, processes, methods, and applications.

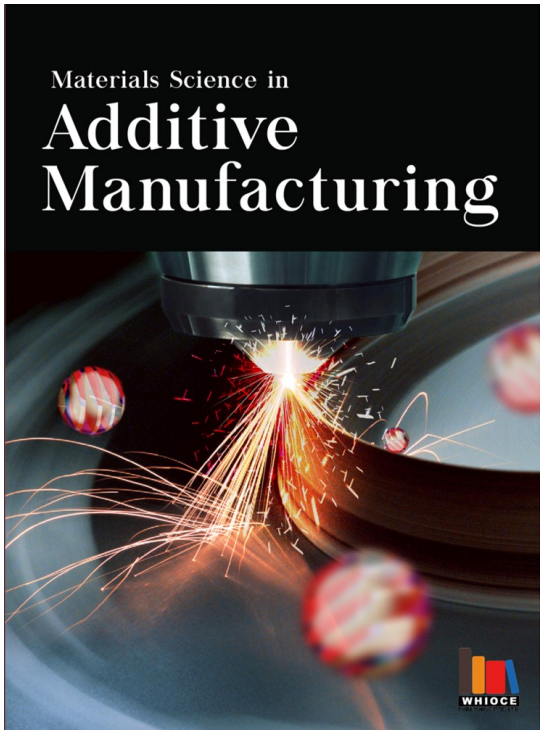

Scan to access website:

Scan to submit papers:

About Whioce Publishing

Whioce Publishing is a publishing company based in Singapore. We have in our portfolio a range of high-quality, open-access, peer-reviewed journals and books.

Contact Us

Managing Editor
Ian Wong
msam.editor@whioce.com

Whioce Publishing
8 Burn Road, #15-03 Trivex, Singapore 369977.

Editorial Office of *Materials Science in Additive Manufacturing*
30-2, Jalan BS 1/2, Olive Hill Business Park, 43300 Seri Kembangan, Selangor. Malaysia.

Volume 1 Issue 3 • September 2022
ISSN 2810-9635 (online)

MATERIALS SCIENCE IN ADDITIVE MANUFACTURING

Editor-in-Chief

Chee Kai Chua

Singapore University of Technology and Design, Singapore

WHIOCE PUBLISHING PTE. LTD.

Full issue copyright © 2022 Whioce Publishing
All rights reserved. Without permission in writing from the publisher, this full issue publication in its entirety may not be reproduced or transmitted for commercial purposes in any form or by any means, electronic or mechanical, including photocopying, recording, or any information storage and retrieval system. Permissions may be sought from info@whioce.com.

Article copyright © Respective Author(s)
See articles for copyright year. All articles in this full issue publication are open-access. There are no restrictions in the distribution and reproduction of individual articles, provided the original work is properly cited. However, permission to reuse copyrighted materials of an article for commercial purposes is applicable if the article is licensed under Creative Commons Attribution-NonCommercial License. Check the specific license before reusing.

MATERIALS SCIENCE IN ADDITIVE MANUFACTURING

ISSN: 2810-9635 (online)

Editorial and Production Credits

Publisher - Whioce Publishing
Managing Editor - Ian Wong
Editorial Assistant - Flora Kang
Production Editor - Ian Wong
Journal Development Editor - Felicia Wang
Article Layout and Typeset: Sinjore Technologies (India)
Cover Design: BUTTON GRAPHIC DESIGN STUDIO (Malaysia)

For all advertising queries, contact info@whioce.com.

Supplementary file

Supplementary files of articles can be obtained at https://msam.whioce.com/index.php/MSAM/issue/view/9.

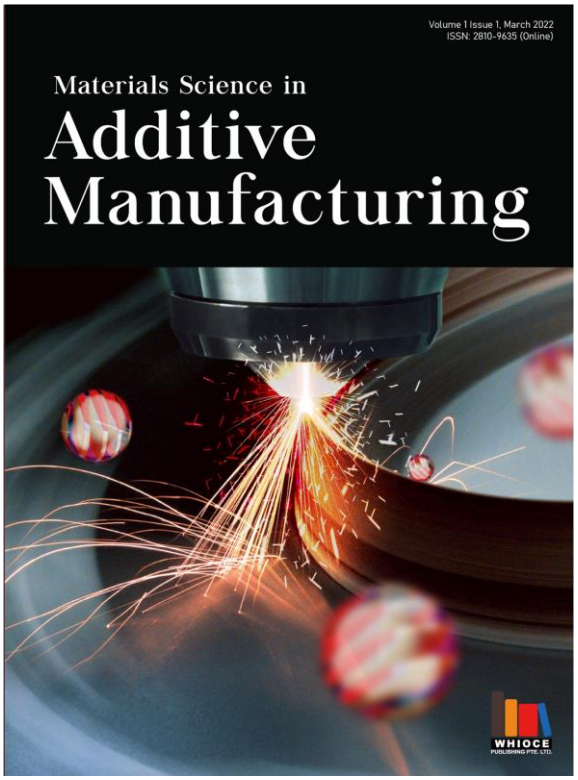

About the Cover

Directed energy deposition in progress

Disclaimer

Whioce Publishing is not liable to the statements, perspectives, and opinions contained in the publications. The appearance of advertisements in the journal shall not be construed as a warranty, endorsement, or approval of the products or services advertised and/or the safety thereof. Whioce Publishing disclaims responsibility for any injury to persons or property resulting from any ideas or products referred to in the publications or advertisements. Whioce Publishing remains neutral with regard to jurisdictional claims in published maps and institutional affiliations.

Materials Science in Additive Manufacturing

Editorial Board

Editor-in-Chief

Chee Kai Chua
Singapore University of Technology and Design, Singapore

Associate Editor

Swee Leong Sing
National University of Singapore, Singapore

Editorial Board Members*

Shweta Agarwala, *Denmark*

Clodualdo Aranas Jr, *Canada*

Mahdi Bodaghi, *UK*

Dongdong Gu, *China*

Charlotte Hauser, *Saudi Arabia*

Jingchao Jiang, *Hong Kong (China)*

Paulo Jorge da Silva Bártolo, *Singapore*

Ming C Leu, *USA*

Guha Manogharan, *USA*

Eujin Pei, *UK*

Nai Mui Ling Sharon, *Singapore*

Cijun Shuai, *China*

Jing Shi, *USA*

Jonathan Phuong Tran, *Australia*

Yiwei Weng, *China*

Chunze Yan, *China*

Wai Yee Yeong, *Singapore*

Shangqin Yuan, *China*

Yicha Zhang, *France*

Jack G. Zhou, *USA*

Ali Zolfagharian, *Australia*

*Editorial Board Members as of September 30, 2022

September 2022 | Volume 1 | Issue 3 |

Materials Science in Additive Manufacturing

https://msam.whioce.com/index.php/MSAM/index

CONTENTS

Materials Science in Additive Manufacturing

REVIEW ARTICLE

Biodegradable materials: Foundation of transient and sustainable electronics

Monisha Monisha, Shweta Agarwala*

Department of Electrical and Computer Engineering, Finlandsgade 22, Aarhus University, Denmark

Abstract

Biodegradable materials are designed to degrade in a desired time either through the action of microorganisms or under certain physical conditions. The driving force behind the rise of biodegradable materials is the growing problem of electronic waste (e-waste), low recyclability, and toxicity of electronic materials. Transient response of biodegradable materials has found application in next-generation health-care and biomedical devices. Advances in material science and manufacturing technique have pushed the envelope of innovation further. This review discusses different biodegradable material classes that have emerged to replace the traditional non-biodegradable materials in electronics. Focus has been given to conversion of biodegradable materials to inks and pastes that find use in printed electronics to create flexible, bendable, soft, and degradable devices. Material degradation behavior and dissolution chemistries have been illustrated to understand their impact on electrical performance of devices. Finally, some short-term and long-term challenges are pointed out to overcome the commercialization barrier.

***Corresponding author:**
Shweta Agarwala
(shweta@ece.au.dk)

Citation: Monisha M, Agarwala S, 2022, Biodegradable materials: Foundation of transient and sustainable electronics. *Mater Sci Add Manuf,* 1(3): 15.
https://doi.org/10.18063/msam.v1i3.15

Received: July 31, 2022
Accepted: September 2, 2022
Published Online: September 21, 2022

Copyright: © 2022 Author(s). This is an Open Access article distributed under the terms of the Creative Commons Attribution License, permitting distribution, and reproduction in any medium, provided the original work is properly cited.

Publisher's Note: Whioce Publishing remains neutral with regard to jurisdictional claims in published maps and institutional affiliations.

Keywords: Biodegradable materials; Biodegradable metals; Biodegradable polymers; Transient electronics

1. Introduction

Technological advancements and ever-increasing reliance on electronic devices have seen an unprecedented increase in the recent times. This has made our life easier, communication faster, and medical devices precise. Simultaneously, it has created an issue of growing electronic waste (e-waste). Just like plastic waste, e-waste takes up the space, releases toxins in the environment, and is not degradable. E-waste is the world's fastest growing waste stream with figures hitting around 74 metric tonnes by 2030[1]. Conventional electronics uses inorganic materials, namely, silicon, copper, and gallium arsenide, which degrade through corrosive action. The inorganic metals and ceramics undergo degradation through mediation of surface reactivity, metal catalysis, and resorbability. Most of the inorganic materials form an inert protective layer on exposure to the environment, thus hampering its degradation. Even if the material can be degraded under certain conditions, it often leads to leaching of heavy metal ions, which are toxic to the living organisms and cause environmental issues.

This has led researchers and industries to explore ways of not only recycling existing electronics but also finding viable alternatives to the non-degradable materials used

in electronic chips. Obtaining green materials, eco-friendly fabrication processes, and devices with low embodied energy have become prerequisite for sustainable electronics moving forward. There is a growing need for the development of biodegradable materials that can partially or completely degrade into non-toxic material under normal environmental and physiological conditions. Electronics fabricated using these materials are termed as transient electronics as they disintegrate fully or partially after a certain period of steady operation. The development of biodegradable electronic materials and devices that safely degrade at the end of their life cycle will reduce the financial costs, health care, and environmental risks and streamline the waste management system. The emerging technology of biodegradable electronics has expanded opportunities in many sectors, such as solar cells, batteries, and plant monitoring sensors with main influence being in health care (Figure 1). In this review, we discuss the emergence of biodegradable materials, which have application in electronics. The biodegradable materials, namely, conductors, semiconductors, and insulators and dielectrics, are categorized according to their electrical performance. The paper also discusses emerging functional materials such as inks and pastes that are being used in additive manufacturing and printed electronics. The dissolution chemistry of the materials is discussed in detail with emphasis on the electrical performance. Finally, the review discusses the recent developments in the field of electronics and their end of life and highlights the challenges associated with the biodegradable materials and their applications.

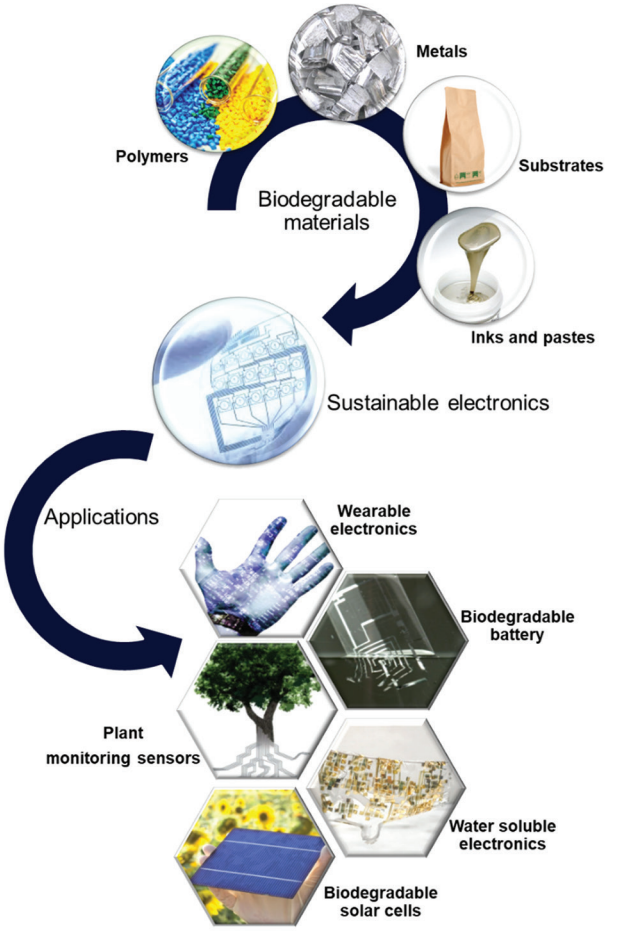

Figure 1. Schematic diagram illustrating various categories of biodegradable materials and their application in electronics.

2. Biodegradation mechanism

The biodegradation of the materials into its smaller constituents generally involves the process that is either influenced by biotic means that involve microorganisms such as fungi and bacteria or abiotic means that involve hydrolysis, photolysis, or oxidization. In nature, both biotic and abiotic mechanisms exist together and the whole degradation is a sum of both. The degradation of the materials is affected by many factors external (environment) and internal (molecular structure). There are mainly two different types of degradations categorized as biotic and abiotic. Biotic degradation, also referred to metabolic degradation, leads to disintegration of the material through the change in their physicochemical properties through microorganisms. Most materials are degraded by microbial attack in a single step. Biotic degradation is the most significant removal pathway of contaminants from the natural environment. If the biological activity is the predominant influence in the breakdown of a material, then it is referred to as abiotic degradation. The process mainly includes hydrolysis and photolysis. Hydrolysis in water is often accelerated by the presence of acids and bases. Photolysis is a light-induced redox reaction, which breaks the constituents wherever the light can reach.

2.1. Dissolution chemistry

In studying biodegradable materials, most of the research has been focused on dissolution rates, wherein a material breaks up into smaller group of molecules or constituents in a solvent. In general, investigations on the dissolution rates of biodegradable materials do not involve microorganisms. Research in dissolution chemistry of biodegradable materials involves dissolving them in suitable solvents or hydrolysis in water or biofluids. Dissolution rate of various biodegradable electroactive materials is given in Table 1. The mechanisms and kinetics of dissolution and their reaction products are important for potential application of biodegradable materials in eco-friendly electronics, biomedical devices, and environmental sensors. All the investigations involving degradation of metals follow the

Table 1. Dissolution rate of various biodegradable electroactive materials

Electroactive material	Dissolution rate			References
	DI water	Hanks' solution	PBS buffer	
Mg foil	-	1.08 μm/day	-	[3]
Mg	1.7×10^3 nm/day	-	-	[16]
MgO/Mg $(OH)_2$	5 – 8 nm/day	-	-	[17]
MgO	~50 nm/h	-	-	[21]
Mg – 1Zn – 0.2 Sr - Mg – 1Zn – 1Sr alloys	-	0.53 – 5.09 mm/year	-	[22]
W foil	-	0.19 μm/day	0.15 μm/day	[9]
W	-	-	300 – 700 μm/year	[23]
ce-WS2	-	-	5 – 8 nm/week	[16]
W/MgO/Mg/W-based device	20 min	-	-	[24]
W and Mo oxides	~0.2 – 0.5 nm/day	-	-	[17]
Mo	$(1 \pm 0.1) \times 10^{-3}$ μm/h	-	-	[7]
Mo	7 nm/day	-	2 nm/day	[16]
Mo foil	-	0.005 μm/day	0.02 μm/day	[9]
ce-MoS_2	-	-	10 – 20 nm/week	[16]
Zn foil	-	7.2 μm/day	3.5 μm/day	[9]
Zn/PVA	5 days	-	-	[25]
ZnNPs/Ag NWs (5 wt%)	40 h	-	-	[26]
ZnO	15 h	-	-	[27]
Zn: PVP: glycerol: methanol (7:0.007:2:1)	25 min	-	-	[28]
Fe foil	-	0.005 μm/day	0.08 μm/day	[9]
Si NM	-	-	5 nm/day	[16]
Si NM	-	-	4.5 nm/day	[29]
Monocrystalline Si NMs	0.2 nm/day	58 nm/day	4.8 ± 0.2 nm/day	[15]
SiO_2	-	-	14 nm/day	[16]
Poly-Si	2.8 nm/day	-	-	[19]
a-Si	4.1 nm/day	-	-	[19]
SiGe	0.1 nm/day	-	-	[19]
Ge	3.1 nm/day	-	-	[19]
SiO_2	0.13 nm/h	-	-	[20]
Si_3N_4	0.0044 nm/h	-	-	[20]
Silk/PEDOT: PSS	~10 days	-	-	[30]
GG5	~0.85%/day	-	-	[31]
GP: G (0.9:5 – 1.8:2.5)	~0.9% – 0.01%/day	-	-	[31]
PPOMaC 4	-	-	77.50 ± 1.93% (10 weeks)	[32]
EPPOMaC 8	-	-	18.45 ± 4.44% (10 weeks)	[32]

fundamental mechanisms and consequences which are established through in-depth experiments employing metal films in deionized (DI) water. In every case, majorly three types of changes were observed: (i) Mass loss happens at rates lower than the electrical dissolution rate (EDR), primarily because micropores and/or pits form; (ii) oxides appear on the surfaces as dissolution products, where they can act as protective layers to slow down the dissolution of underlying metal; and (iii) the formed residual oxide layers dissolve much more slowly than the metal.

Thus, it is important to study the degradation process of metals impacted by dissolution kinetics. Equation I

was suggested by Li *et al.*[2] to calculate the rates at which bioresorbable metal degrades.

$$v = \sqrt{kD}\,\frac{\omega_0 M}{q\rho M_{H2O}}\,tanh\sqrt{\frac{kh_0^{\,2}}{D}} \qquad \text{(I)}$$

Where, k is the reaction constant, D is the diffusivity of water phosphate-buffered saline (PBS), ω_o is the initial water concentration, q is the number of water molecules that react with each atom of the material, ρ is the mass density of the dissolution material, and M and M_{H2O} are the molar mass of the dissolution material and water, respectively. By adjusting the pH of the solution and observing the time-dependent changes in electrical resistance, Rogers *et al.*[3] investigated the dissolution rates of several bioresorbable metallic films. The metallic films degraded in DI water and in Hanks' Balanced Salt Solution (HBSS), which has a pH range of 5-8. Chloride ions (Cl^-) caused Mg to deteriorate 10 times more quickly in HBSS than in DI water. Regardless of pH or temperature, the presence of Cl^- ions speeds up the degradation of Mg by removing its surface protective layer[4]. Zn exhibits an 8.2, 2.6, and 3.3 times greater EDR in salt solution with pH values of 5, 7.4, and 8, respectively, following the same trend. Zinc hydroxide, $Zn(OH)_2$, a metabolite, is produced when zinc oxide (ZnO) is solubilized in water[5]. In a dissolution test in DI water and at room temperature, conducted by Dagdeviren *et al.*,[6] it was discovered that 200 nm thick ZnO vanished entirely in 15 h. W has 4 times higher EDR in salt solution with a pH value ranging from 7.4 to 8 as compared to a solution with pH value of 5. This is attributed to the sensitivity of W toward deposition conditions. The EDR of W deposited using the sputtering technique was higher than the one formed using chemical vapor deposition (CVD). Mo has a greater EDR in DI water than in salt solution, in contrast to Mg and Zn. The greater concentration of dissolved oxygen in aqueous solution is responsible for this difference[7]. It showed slower dissolution rates at higher pH in HBSS, as shown in Figure 2A and B[3]. Although, Fe has the highest EDR at pH 5, but due to the development of passive oxide layer in DI water, its dissolution ceases after 120 h[8]. Within a few days, 300 nm thick oxides on Mg, AZ31B Mg alloy, and Zn completely vanished in DI water, while residual oxides were detected on Mo (40 nm) and W (150 nm) substrate for a few weeks, which makes the degradation process slower[3,9-11]. As stated earlier, pure Si is a non-degradable material. However, nanostructured Si may have dissolution kinetics that can be varied. Its dissolution kinetics was studied by monitoring the change in Si nanomembranes (NMs) thickness with time using profilometer or atomic force microscopy (AFM) in bovine serum[12]. As shown in Figure 2C and D, a variety of variables, including pH, temperature, concentration, doping level, and the types of ions and proteins present in the solution, have a substantial impact on the dissolving rates[12-15]. Higher temperatures and pH levels were shown to speed up the dissolution process, but doping levels more than 10^{20} cm^{-3} had the reverse effect[12,13]. Similar to Mg dissolution, the presence of chlorides and phosphates above a certain level at approximately pH = 7.5 accelerates the Si dissolution (Figure 2D)[14]. In another study, researchers found that extremely thin Si NMs hydrolyze to form orthosilicic acid, $Si(OH)_4$[16]. These NMs with variable thickness from 35 to 100 nm dissolve in PBS at 37°C in ~ 8 – 22 days with the approximate rate of 4.5 nm/day[17]. The dissolution rate (R) of Si at temperature T with molar concentrations of water and hydroxide ions was given by Equation II[13,18].

$$R = k_0\left[H2O\right]^4\left[OH^-\right]^x e^{\frac{E_A}{kBT}} \qquad \text{(II)}$$

Where, k_B is the Boltzmann constant, E_A is the activation energy, and fitted values of x fall in the range of 0.46 – 0.9. The dissolution rate increased with increase in the pH value. Change in the concentration of PBS solution from 0.05 to 1 M increased the dissolution rate from 10 to 20 times. Besides for Si NMs, above equation can be used to determine the dissolution rate of other semiconducting materials such as polycrystalline amorphous Si (a-Si), Si (poly-Si), Si-Ge alloy (SiGe), and Ge. Their dissolution rate was found to be 4.1, 2.8, 0.1, and 3.1 nm/day, respectively, in a buffer solution of pH 7.4 at 37°C. Studies using molecular dynamics (MD) simulations and density functional theory (DFT) indicated that silicon dissolution initiates by the nucleophilic attack on silicon surface bonds, weakening the inner bonds. This makes them even more prone to subsequent ion attacks[14]. The dissolution rates of a-Si, poly-Si, and Ge increased by 10^2 – 10^3 times, and those of SiGe increased by 10 times, with a rise in pH from 7 to 10^{19}. Kang *et al.*[20] examined the SiO_2 and Si_3N_4 dissolving rates in various pH solutions. The room temperature dissolution rates for SiO_2 and Si_3N_4 are around 0.13 and 0.0044 nm/h in a buffer solution of pH = 7.4, respectively. The dissolution rates were increased by one or two orders in magnitude with increase in pH value to 12. Another study found that a 150 nm thick MgO film created using electron beam evaporation may disintegrate in deionized water at a rate of about 50 nm/h[21]. Thus, the dissolution rate of metals gets affected by the change in conditions and deposition method of the film.

3. Biodegradable conducting materials

3.1. Metals

Metal has widely been used as interconnects and electrodes in electronic devices. They have found their wide usage in

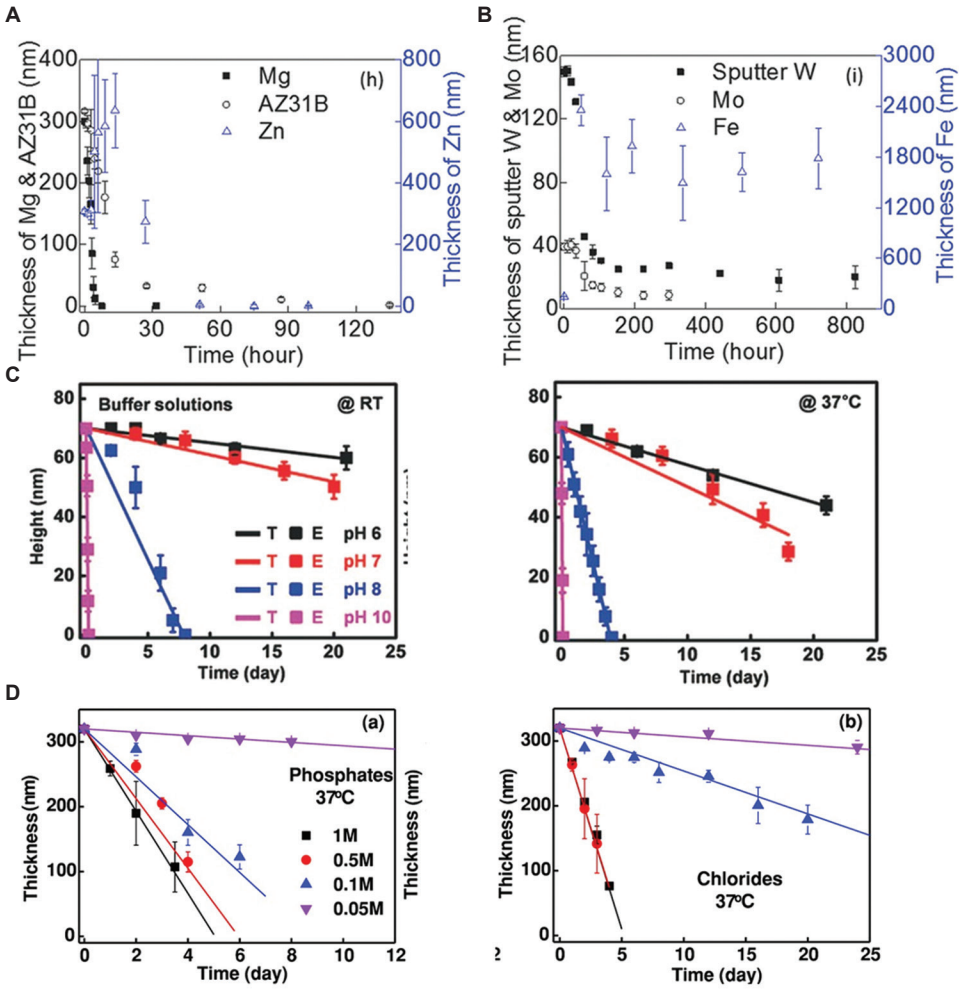

Figure 2. Change in thickness of thin films of metals with time during dissolution in DI water at room temperature for (A) Mg, AZ31B Mg alloy and Zn; (B) sputter deposited W, Mo, and Fe; (C) hydrolysis of Si NMs in buffer solutions at different pH at room temperature (left) and at physiological temperature (right, 37°C); and (D) change in thicknesses of Si NMs with time on immersing in aqueous solutions of potassium chlorides and potassium phosphates at 37°C with different concentrations. Reprinted with permission from Yin *et al.*, Hwang *et al.*, and Yin *et al*[3,13,14].

batteries[33,34], sensors[35-38], implantable stimulators[39,40], and energy harvesters[41] (Figure 3A)[6,42,43]. Despite this, only few degrade naturally and are considered biodegradable. The metals in aqueous conditions degrade through corrosion, leading to the formation of oxides and hydroxides. For example, metals such as zinc (Zn), iron (Fe), magnesium (Mg), and molybdenum (Mo) undergo degradation through reactions of hydrogen evolution in neutral aqueous mediums media, while tungsten (W) undergoes corrosive process through oxygen absorption in aqueous environment[23,44-49].

Much of the early work on biodegradable metals started with iron, which was used in wire form for implants[50]. However, investigations on Fe remain low due to the issue of easy corrosion and slow degradation rate. Mg remains the most sought after biodegradable materials due to its good mechanical properties and biocompatibility. Much investigations have been carried out on alloys of Mg, namely, Ma-Ca, Mg-Zn, Mg-Si, and Mg-Ag[22,29]. Hwang *et al.* used Mg electrodes in silicon-based transient device[17]. Later, their group demonstrated uniform dissolution of Mg in DI water with the formation of MgO and $Mg(OH)_2$ on the surface, which took the shape of nanoneedle-like structures[3]. Both the end products have high solubility in water and can be dissolved easily. Recently, research group at University of Glasgow fabricated a transient transistor based on n-channel silicon nanoribbons on Mg as substrate[24]. The fabricated transistor performed well with high mobility and high on/off current ratio. They studied the effect of transience on the electrical functioning of the device and observed Mg degradation under different pH. In another report by Cao *et l.*,[51] a transient volatile memristor

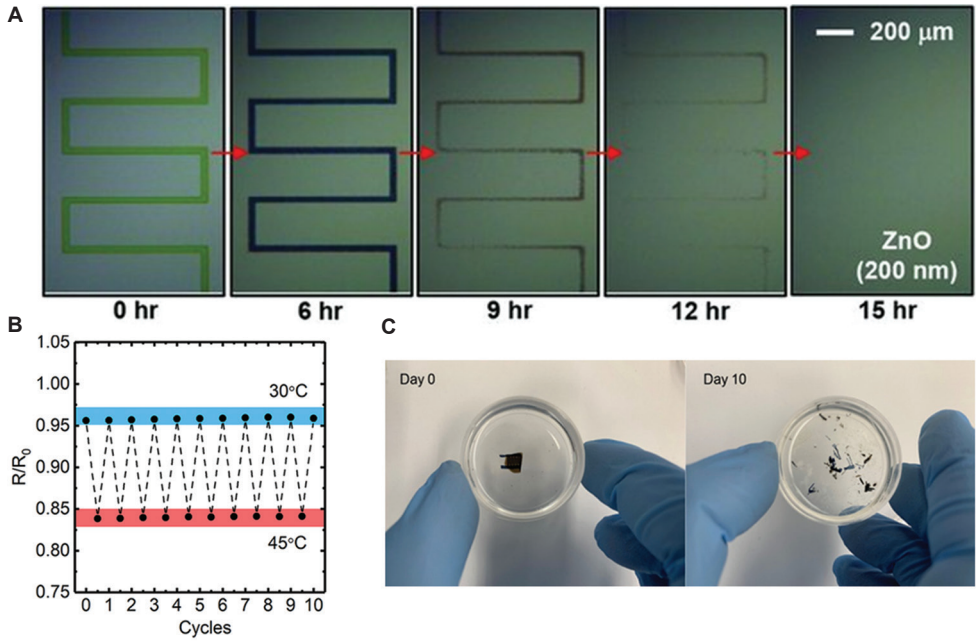

Figure 3. (A) A series of optical microscope images were taken at different points during the dissolution of a meander trace of ZnO (200 nm) submerged in DI water at room temperature, (B) changes in the relative resistance of a PEDOT: PSS-based printed temperature sensor subjected to cyclic heating and cooling run between 30°C and 45°C, and (C) the degradation of the flexible temperature sensor over the course of 10 days in an enzymatic (protease) environment. Reprinted with permission from Dagdeviren *et al*., Wang *et al*., and Pradhanand and Yadavalli[6,58,60].

device using Mg as an active electrode was fabricated on a polyvinyl alcohol (PVA) substrate. The full degradation of the device was achieved in DI water in about 20 min. Mg-based biodegradable metals have rapid degradation rates, resulting in loss of mechanical performance in short span and thus limiting its applications. Hence, Mg-based biodegradable materials will benefit from decreased degradation rates while Fe may need enhanced rates. Zn is heralded as the next promising metal for biodegradability. Zn-based materials overcome several drawbacks that were observed for other biodegradable materials. Wang *et al.*[52] studied mechanical properties of Zn alloy as a degradable biomaterial by casting with Mg. They showed Mg-Zn alloy degradation behaviors in simulated body fluid (SBF) solution. Both Mo and W show slow degradation rates. The variation in degradation rates of metals provides multiple options to use in different applications. Crystalline Zn films with conductivity of approximately 1.124×10^6 S/m were produced on a cellulose substrate. The resulting resistive Zn strain gauge array with a gauge factor of ≈1 exhibited no delamination or cracking, or electrical degradation after repeated stretch-release cycles, and a deflection of ≈16 mm (radius of curvature) was stably detected[53]. It is interesting to note that post-processing method has a considerable effect on the conductivity values of biodegradable metals. Electrochemical sintering process of Zn microparticles was carried out with acetic acid solution, and enhanced conductivity was observed ($\approx 3 \times 10^5$ S/m)[25]. The conductivity value of 1.124×10^6 S/m for Zn was obtained through laser sintering rather than heat sintering. Photonic sintering has also been applied, which resulted in high conductivity value of 44,634 S/m[48]. An alternate way of enhancing the conductivity of biodegradable metals is by making the composite with other highly conducting materials. The performance of Zn metal was enhanced by adding small amounts of silver nanowires (NWs), leading to maximum conductivity of 307,664.4 S/m after sintering[26]. Nevertheless, adding Ag may compromise the biodegradability of the overall composite.

3.2. Polymers

Polymer materials have better biodegradability and biocompatibility than metals and have been much sought after. This is true for both natural and synthetic polymers. Synthetic polymers are particularly attractive as their degradation rates can be tuned through triggered depolymerization. Moreover, polymer materials are cheap and easy to process that make them attractive for commercialization. Organic polymers show conducting properties through introduction of conjugation or doping with conductive materials. Examples of conjugated polymers are polyaniline (PANI), polypyrrole (PPy), and poly(3,4-ethylenedioxythiophene) (PEDOT). The conjugated network in conductive polymers makes

them brittle and inflexible, which can be overcome by doping the conjugated polymers without affecting their electrical properties[54-56]. PEDOT: PSS, a polymer doped with poly(styrenesulfonate) (PSS), shows the best known conductivity of up to 4.6×10^5 S/m in polymeric materials[57]. This electrode was developed by Worfolk *et al.*[58] to fabricate a sensor with a sensing range from 30°C to 45°C (Figure 3B).

Another strategy to tune degradability is to blend conducting polymers with biodegradable polymers to achieve partial degradation. Partial degradation is achieved, as these polymers do not break down completely into monomers. Shi *et al.* used a composite of PPy nanoparticles (NPs) with poly(D,L-lactic acid) (PDLLA), where NPs formed a conductive network within the PDLLA matrix for fibroblast growth. Adding even a small amount of PPy leads to high conductivity (approximately 1×10^{-3} S/cm), with the material being stable for about 1000 h[59]. Similarly, Wang *et al.*[30] used a combination of hyaluronic acid (HA)-doped PEDOT (10% NP loading) with poly(L-lactic acid) (PLLA) to fabricate a conductive film. The degradation of PLLA was accelerated by PEDOT-HA by almost 10%. The enhanced degradation can be assigned to increased water penetration in PLLA due to the presence of hydrophilic HA.

In another work, a mixture of PEDOT: PSS with photosericin and Irgacure 2959 photoinitiator was synthesized to prepare a conducting material. The fabricated sensor showed a high sensitivity (–0.99% °C^{-1}) in the temperature range of 20 – 50°C and excellent stability on exposure to about 60% relative humidity. The sensor was degradable in approximately 10 days under proteolytic conditions (Figure 3C)[60]. Hybrid approaches have also been investigated to realize fully degradable materials wherein inorganic materials are mixed with organic materials. In one report, Si NPs were mixed with carbon black and PEDOT: PSS to make electrodes for lithium-ion battery application[61].

Li *et al.*[62] reported electrospun camphor sulfonic acid (CPSA) doped with PANI and gelatin to obtain high conductivity material (up to 2.1×10^{-2} S/cm). In another report, CPSA/PANI composite was doped with poly(L-lactide-*co*-ε-caprolactone) and showed high conductivities (up to 1.38×10^{-2} S/cm). Electrical stimulation through these conducting fibers showed increased adhesion and proliferation for fibroblasts and myoblasts cells[63]. Hydrogels obtained by grafting PANI with gelatin and doping with CPSA exhibited conductivities around 10^{-4} S/cm[31]. P3HT was electrospun with polycaprolactone (PCL)[40] and polylactic-glycolic acid (PLGA)[64] to introduce partial degradability. The resulting electrospun nanofibers with PCL, however, displayed lower values of mobility (1.7×10^{-2} cm^2/V.s) due to macroscopic phase segregation.

3.3. Inks and pastes

The emerging field of printed electronics, an additive manufacturing technology, has opened doors to directly write electronic materials on desired substrates. The technology requires the materials to be converted to functional inks and pastes to be printed through inkjet, aerosol jet, screen printing, pneumatic head, or laser-based techniques. Hence, many conducting metals have been dissolved in aqueous, polar, or non-polar solvents to convert to inks. Biodegradable inks differ in particle size, types of additives, and solvent. In general, the biodegradable inks are made up of three key ingredients, namely, nanoparticles, small quantity of polymers as stabilizers, and suitable solvent. Mahajan *et al.*[65] prepared a stable conductive ink by dispersing Zn NPs (of average diameter 50 nm) with PVP particles in a solvent mixture of methanol and butyl acetate. In another work, Zn NPs were mixed with Ag NWs and polyethylene oxide (PEO) to prepare the ink[26,66]. Addition of Ag NW also adds a stretchable character to the printed patterns. Most of the prepared inks and pastes were processed using printed techniques such as screen printing, inkjet, and aerosol printing. To create a uniform dispersion of the biodegradable material particles, polymers are used as additives. Most of the additives, however, are insulating in nature and could hinder electron transport. Thus, it is important to post-process the printed patterns by heat sintering to degrade the additives. Huang *et al.*[67] prepared a W paste with PEO particles as additives in methanol. As stated earlier, most metal-based biodegradable materials are brittle at room temperature and, thus, require some sort of post-processing to enhance the mechanical properties. Li *et al.*[66] improved the conductivity of the Zn ink by an improved water sintering method. This ink showed the capability to withstand 1500 repeated bending test with a curvature of 3.8 mm. In another study, an ink based on Zn and Ag NW composite exhibited a high conductivity with excellent mechanical using the same water sintering approach. The authors demonstrated that the printed patterns were robust and could withstand 8000 bending cycles[26].

4. Biodegradable semiconducting materials

4.1. Inorganic semiconductors

Semiconductors have a bandgap, and their electrical conductivity is between conductors and insulators. They play a major role in fabrication of the electronic devices. Present electronic industry is based on silicon (Si) semiconductor, which is used in various forms to make devices, namely, monocrystalline silicon

(mono-Si)[68], amorphous silicon (a-Si)[69], polycrystalline silicon (poly-Si)[70], and silicon alloys[71]. The various Si forms used in the present day do not degrade due to the formation of a native oxide layer on top, which renders them chemically inert. Research has been focused toward increasing the hydrolysis rate of Si by reducing their thickness and aspect ratio to make nanostructures[72]. The hydrolysis of Si in water results in the formation of orthosilicic acid ($Si(OH)_4$)[72]. Most of the work has been done on Si-NM. Hwang *et al.*[12] carried out detailed investigation on the dissolution behavior of Si-NM nanostructures on silicon dioxide/silicon substrate through observing thickness change against time (Figure 4A). Through various reported literature, it has been established that the dissolution kinetics of Si NM depends on physical factors such as microstructure, geometry, and surface conditions and on external factors such as pH and temperature[12,73,74]. Effect of pH on Si NM has been widely investigated, where Yin *et al.*[55] found that the higher concentration on OH^- ions in the solution led to faster dissolution. The group also explained the weakening of Si-Si backbones in the material through nucleophile ions being bonded to Si surface. Si-NM shows promising results in enabling a Si-based material that can be degraded under various conditions. Silicon-germanium alloys have also shown dissolution in varying pH and temperature ranges[73,75]. Increased pH led to reactions that produced metagermanic acid (H_2GeO_3) on hydrolysis.

Inorganic oxides such as magnesium oxide (MgO), zinc oxide (ZnO), and silicon dioxide (SiO_2) have also been explored in biodegradable electronics due to their superior thermal and chemical stability. The rationale is to keep the material layers thin for better dissolution, as they are dissolvable in aqueous solutions. The dissolution rates depend on many physical and chemicals properties and external factors such as pH, temperatures, and ion concentration in the solution[9,17].

4.2. Organic semiconductors

Although organic semiconductors have inferior electrical properties compared to their inorganic counterparts, they have the advantage of faster dissolution. Madrigal *et al.*[76,77] prepared a composite film from poly(3-thiophene methyl acetate) (P3TMA) by blending with thermoplastic polyurethane (TPU). The composite film demonstrated semiconducting behavior with a wide bandgap (~2.35 eV). However, due to the non-degradability of P3TMA, the film was only partially degradable. A fully biodegradable semiconducting film (PDPP-PD) was

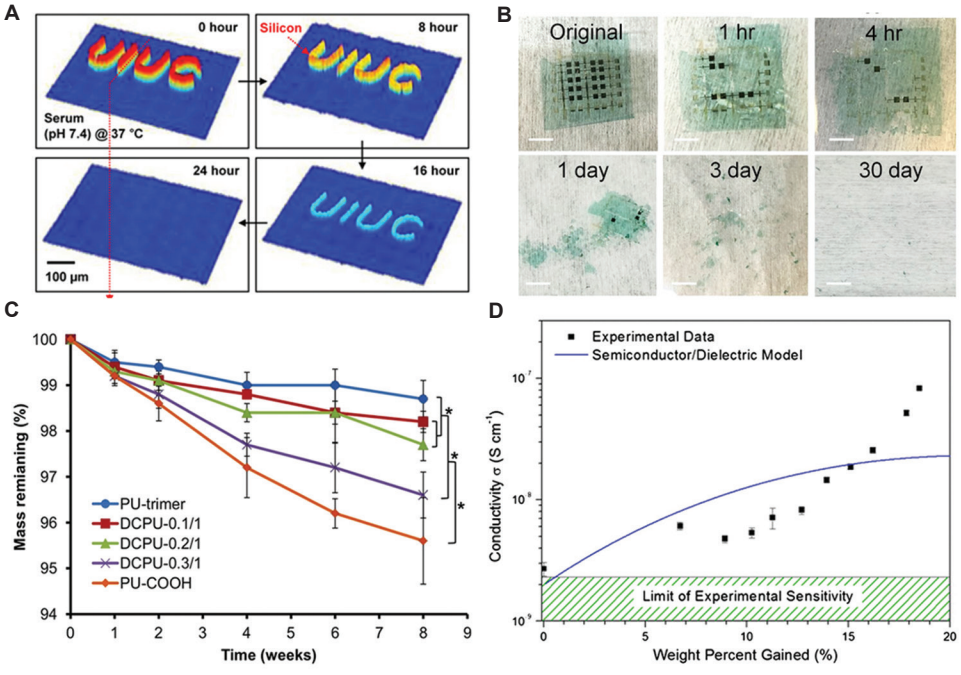

Figure 4. (A) Images of Si NMs at different stages of dissolution in bovine serum (pH 7.4) at physiological temperature (37°C) were measured using laser diffraction phase microscopy (DPM): 0 h (top left), 8 h (top right), 16 h (bottom right), and 24 h (bottom left). (B) Photographs of a totally disintegrable device prepared using PDPP-PD semiconducting film at various stages of disintegration (scale bars: 5 mm). (C) Mass remaining for DCPU in PBS at 37°C. (D) Change in conductivity of melanin with water content. The measured humidity was transformed into the percentage of weight gained due to water absorption. Reprinted with permission from Hwang *et al.*, Lei *et al.*, Xu *et al.*, and Mostert *et al*[12,78-80].

prepared by introducing reversible imine linkages between diketopyrrolopyrrole (DPP) and p-phenylenediamine. The conjugation along the backbone of this polymeric film allows for hole conduction. The degradation of the material takes place through breaking of imine bonds under acidic conditions to give aldehyde and amine precursors as the by-products (Figure 4B)[78]. Xu *et al.* reported a polyurethane-based conductive elastomer (DCPU) based on PCL, which used dopant as dimethyl propionic acid and aniline trimer linkers. The conductivity of the synthesized polymer could vary between 10^{-8} and 10^{-5} S/cm in the dry state. Depending on the concentration of dopant present in the polymer, conductivity could be enhanced further on soaking in PBS. Due to the presence of hydrophilic carboxylic functional groups, with the increase in DMPA content, degradation rate increased in aqueous PBS solution. The polymer degraded to ~75% of its weight in 14 days in PBS and in the presence of lipase without any decline in conductivity during degradation period (Figure 4C). The chemical linkage in the matrix helps to stabilize the dopant and leads to improved electronic performance[79]. Natural pigments[80,81], conjugated molecules such as *Indigofera tinctoria* and *Isatis tinctoria*[82], melanin, and β-carotene[83,84] have also been explored for the preparation of biodegradable electronics. Some natural semiconductor materials include indigo with a band gap of 1.7 eV and decent carrier mobilities. Eumelanin, a subclass of melanin, also exhibits electronic behavior. Conductivity of melanin depends on temperature, its hydration state, and physical form. Mostert *et al.*[80] demonstrated that eumelanin conducts free electrons and protons for electronic and ionic conduction, respectively, after absorption of water molecules, as shown in Figure 4D. The material was used as a regenerative medical scaffold, which could resorb in about 8 weeks[81].

Fully biodegradable conducting polymers can be prepared by interrupting the conjugation with the introduction of flexible non-conjugated linkers in the polymer backbone. This process makes the polymers flexible and processing easy, but decreases the conductivity as compared to partially degradable conductive polymers[31,79,85,86]. Due to the intrinsic flexibility of the material, these polymers are used in sensors as interconnects where low conductivity is not an issue. Electrical stimulation to promote cell growth and tissue regeneration of scaffolds and muscle tissues is another application of low conducting polymers[86-88]. There is a need to develop new chemistries and increase the conductivity of polymers to fabricate high-performance degradable electronics. Conductivities of various biodegradable conducting materials are given in Table 2.

5. Biodegradable dielectrics

When an electric field is present, dielectric polymers, which are insulators, can become polarized. The dielectric constant (κ), which can be high or low depending on the application, determines polarization. High-κ fillers can be added to a degradable polymer matrix to produce biodegradable dielectrics (Table 3). Common high-κ metal oxides include aluminum oxide (Al_2O_3, κ = 9), silicon oxide (SiO_2, κ = 3.9), and hafnium oxide (HfO_2, κ = 25). Al_2O_3 was combined with cellulose acetate (CA), and Figure 5A shows that this combination produced a higher κ value of 27.57 at a low frequency of 50 Hz[93]. Besides metal oxides, carbon nanotubes also improved the κ of biodegradable paper made from cellulose nanofibers (CNFs) from ~ 0 to 3198 at 1 kHz[94].

Plant-based fibers such as cotton, bamboo, jute, and banana fibers also possess dielectric properties, as shown in Figure 5B[95-100]. This is because there are free hydroxyl functional groups present, which add polarity and provide high κ values. Cotton exhibits a dielectric constant of 17 between frequency range of 60 and 1000 Hz[101]. Banana, bamboo, and jute fibers were also used as fillers into dielectric composites. The dielectric constant of these composites was found to be increasing with increase in fiber content[102]. Natural sugars also behave as dielectrics. High breakdown voltages of 1.5 MV/cm and 4.5 MV/cm, low loss tangents on the order of 10^{-2} at 100 mHz, and dielectric constants of 6.35 and 6.55 at 1 kHz, respectively, are all characteristics shown by glucose and lactose[84].

Besides natural materials, synthetic materials also exhibit biodegradability. An example of synthetic biodegradable dielectric elastomer is poly(glycerol sebacate) (PGS). Such elastic materials are useful for capacitive sensors since they can withstand compression more effectively and thus can be a useful alternative to viscoelastic polymers. Boutry *et al.*[103] reported a degradable capacitive pressure sensor fabricated using PGS as the dielectric sandwiched between biocompatible Mg and Fe metal electrodes. Fabricated sensor showed excellent time response while detecting small weights of single grain of salt weighing only 5 mg (Figure 5C). It is important to note that most of the dielectrics mentioned in this review were investigated at frequencies lower than few kHz. For practical use of these biodegradable dielectrics in complex electronic devices, their optimization is required for high-frequency performance.

6. Biodegradable insulators

6.1. Substrates

Substrates typically constitute most of the weight and volume of an electronic device. Therefore, overall

Table 2. Conductivities of various biodegradable conducting materials

Electroactive material	Conductivity	References
Mg	3.4 mS/cm	[33]
W: methanol: PEO (4:1:0.25)	5200 S/m	[67]
Zn NPs/Na-CMC	1.124×10^6 S/m	[89]
Zn/PVA	9.7×10^5 S/m	[25]
Zn/PVA	$\sim 2 \times 10^6$ S/m	[90]
Zn NPs/PVP (0.1 wt%)	22,321.3 S/m	[65]
Zn NPs/PEO (3 wt%)	72,400 S/m	[66]
ZnNPs/Ag NWs (5 wt%)	307,664.4 S/m	[26]
Zn: PVP: glycerol: methanol (7:0.007:2:1)	60,213.6 S/m	[28]
PEDOT: PSS	4,600 ± 100 S/cm	[56]
10% PEDOT-HA/PLLA	0.47 ± 0.21 S/cm	[59]
30% PEDOT-HA/PLLA	2.58 ± 1.02 S/cm	[59]
50% PEDOT-HA/PLLA	6.94 ± 1.23 S/cm	[59]
Silk/PEDOT: PSS		[30]
Pani: gelatin (0:100 – 60:40)	0.005 – 0.021 S/cm	[62]
CPSA-PANI: PLCL nanofiber (0:100 – 30:70)	0.0015 – 0.0138 S/cm	[63]
GG5	1.21×10^{-4} S/cm	[31]
GP: G (0.9:5 – 1.8:2.5)	$2.41 \times 10^{-4} - 4.54 \times 10^{-4}$ S/cm	[31]
Aligned PLGA-PHT nanofibers	0.1×10^{-5} S/cm	[64]
Random PLGA-PHT nanofibers	0.2×10^{-6} S/cm	[64]
TPU: P3TMA	$2.23 \times 10^{-5} - 5.19 \times 10^{-6}$ S/cm	[77]
PU-trimer	$2.7 \pm 0.9 \times 10^{-10}$ S/cm	[79]
DCPU-0.1/1	$5.5 \pm 0.7 \times 10^{-8}$ S/cm	[79]
DCPU-0.2/1	$4.6 \pm 0.4 \times 10^{-7}$ S/cm	[79]
DCPU-0.3/1	$1.2 \pm 0.3 \times 10^{-5}$ S/cm	[79]
PU-COOH	$5.5 \pm 1.2 \times 10^{-12}$ S/cm	[79]
Melanin films	$7.00 \pm 1.10 \times 10^{-5}$ S/cm	[81]
2a-PCL EMAP copolymer	5.01×10^{-6} S/cm	[85]
3a-PCL EMAP copolymer	2.42×10^{-5} S/cm	[85]
DNA/HA/SWCNT (0.5/0.3%)	128 ± 15 S/cm	[91]
GelMA/DNA/MWCNT (3/4/6 mg)	24 ± 1.8 S/cm	[91]
Graphene nanoflake ink	0.43×10^5 S/m	[92]

degradation behavior of the electronic device largely depends on the substrate used. Researchers are exploring polymers from natural[91,104-110] and synthetic sources to be used as substrate. Biodegradable polymers that work as excellent substrate materials include polylactic acid (PLA), PLGA (Figure 6A), PVA (Figure 6B), polyglycolic acid (PGA), poly (1,8-octanediol-co-citrate) (POC), silk fibroin, rice paper, and cellulose nanofibril paper [10,17,111-113]. POC was used to fabricate stretchable Si-based pH and electro-physiological sensors using transfer printing. After 12 h, these sensors completely disintegrated in PBS (pH 10) at ambient temperature, as shown in Figure 6C.[111]

By adding maleic anhydride, these elastomers can be rendered photo-cross-linkable, preventing lengthy thermal condensation curing. This method helps increase the variety of materials that can be used as stretchy and biodegradable substrates[32,114,115].

Similarly, silk or its bioresorbable protein fibroin has demonstrated promising applications in electronic devices such as drug delivery systems[27,116-118], wireless therapeutic

Table 3. Dielectric properties of various biodegradable materials

Material	Dielectric constant (1 kHz)	Breakdown field (MV cm^{-1})	Loss tangent (100 mHz)	References
Adenine	~3.85	~1.5	~4×10^{-3}	[84]
Guanine	~4.35	~3.5	~7×10^{-3}	
Glucose	~6.35	~1.5	~5×10^{-2}	
Lactose	~6.55	~4.5	~2×10^{-2}	
Sucrose	-	>3	~8×10^{-2}	
Caffeine	~4.1	~2	~9×10^{-2}	
SiO_2	~3.9	~5-15	-	
CA[a]	8.63	-	0.26	[93]
CA/Al_2O_3 (25 wt%)[a]	27.57	-	0.64	
CNF	-	0.6138	-	[94]
CNF/CNT (4.5 wt%)	-	0.4258	-	

[a]Dielectric constant at 50 Hz.

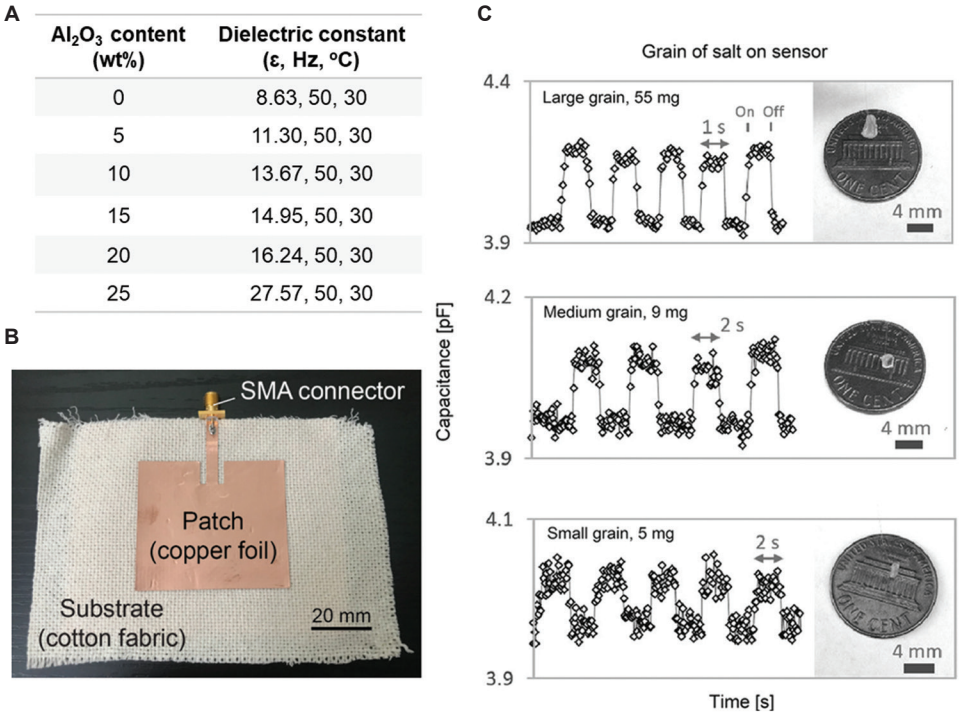

Figure 5. Increase in dielectric constant of cellulose acetate with increase in the addition of high-κ additives, Al_2O_3, (B) antenna sample using cotton fabric as the substrate and the dielectric material, and (C) a sensor array of 4 × 5 pressure-sensitive elements that can quickly respond to detect the presence of a grain of salt (weights: 55, 9, and 5 mg). Figure (A) is adapted from Deshmukh *et al.*[93] Reprinted with permission from Mukai *et al.* and Boutry *et al.*[95,103].

devices[117], energy harvesters,[6,41,119-121] and transistors[17]. Silk in water degrades at a well-characterized rate that can be easily adjusted by several orders of magnitude by regulating the degree of crystallization. Although highly crystalline silk degrades gradually, it can be fragile and challenging to handle. While less crystalline silk is more flexible, it breaks down more quickly in water. This trade-off restricts the manufacture of devices using transfer printing on silk substrates. Hwang *et al.*[13,17] fabricated Si-based microheaters for transient thermal therapy on silk using transfer printing method. These devices degrade after 15 days to prevent infections after surgery (Figure 7A and B).

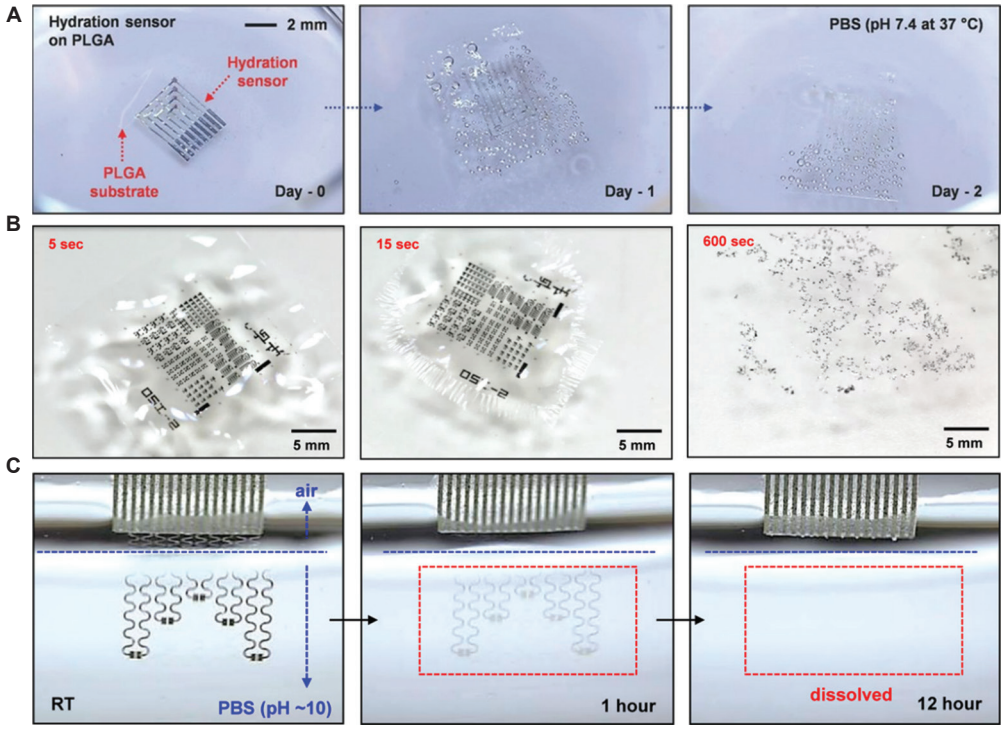

Figure 6. (A) Photographs taken at various stages of the dissolution of a transient hydration sensor on a PLGA film while being immersed in PBS (1 M, pH = 7.4) at physiological temperature at 37°C; (B) a collection of optical microscope photographs taken throughout the dissolution of a-IGZO devices in DI water at room temperature. After 1800 s, the PVA substrate completely dissolves, causing the electronic devices to completely dissociate in the water. (C) A sequence of photos showing the breakdown of a POC-modified Si-based device in room temperature PBS (pH = 10). Reprinted with permission from Hwang *et al*., Hwang *et al*., and Jin *et al*.[10,111,113].

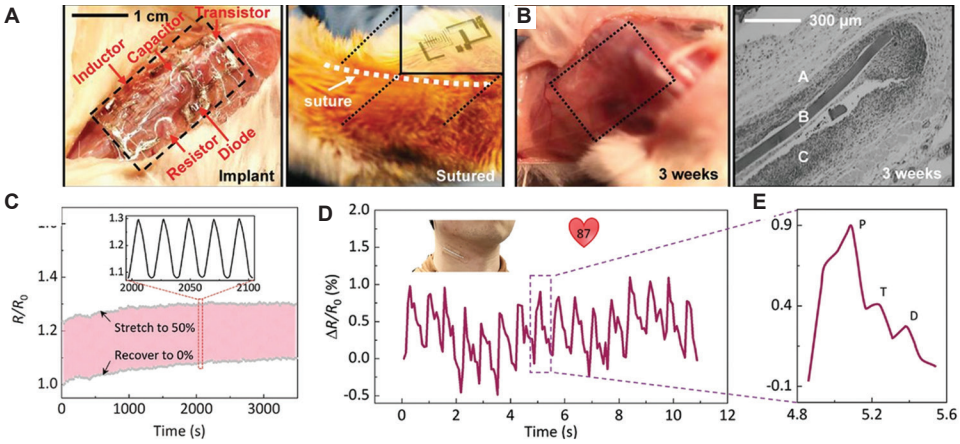

Figure 7. An example of a transient bioresorbable device for thermal therapy, together with *in vivo* evaluations. (A) Images of a demonstration platform for transient electronics implanted (left) and sutured (right) in a BALB/c mouse's subdermal dorsal area. (B) The implant location after 3 weeks (left); an implant site histological section that was removed 3 weeks later reveals a partially resorbed area of the silk film (right); pointers A, B, and C indicate subcutaneous tissue, silk film, and muscle layer, respectively. (C) Relative resistance changes of the gelatin-alginate-based strain sensor under cyclic stretching with 50% strain in air (150 cycles); (D) strain sensor attached to volunteer's neck to detect pulse. (E) The magnified graph corresponding to one cardiac cycle with discernible P-wave, T-wave, and D-wave. Reprinted with permission from Hwang *et al.* and Hao *et al*[13,141].

Plant-based polymers like cellulose, on the other hand, are flexible, transparent, robust at high temperatures, and degrades slowly (on the order of months) when exposed to fungi that are found in nature, making it a good choice for consumer electronics. Cellulose has been used in solar cells[122-124], organic light-emitting

diodes (OLEDs)[125], sensors[126-128], transistors[129-132], biobatteries[133], and radiofrequency identification (RFID) antennas[92,134,135] as substrate. CNFs were also used to fabricate biodegradable and flexible devices using transfer printing method. Good thermal stability of the material made direct printing possible on CNF papers[112,136]. Hsieh *et al.*[137] successfully printed and annealed conductive silver lines on CNF papers, thus demonstrating its full potential for roll-to-roll manufacturing. Despite easy availability of natural materials, such materials possess limitations for the wide applications due to high variation in quality from batch to batch. These variations affect the working of the electronic devices. The use of synthetic polymers is one of the solutions to mitigate such issues. Synthetic polymers can be chemically engineered for better control of physical and chemical properties. A combination of PLA and PGA in different ratios gives bioresorbable polymer with tunable mechanical strength and controlled degradation time[138]. PVA[25,28,66,90,113], PGS-PCL[139], and sodium carboxymethyl cellulose (Na-CMC)[65,67,89] with diverse mechanical and degradation capabilities have been employed due to the various needs for biodegradable healthcare devices. According to a study, numerous bio-based polymer substrate types can be used for printed electronic applications. Compared to conventional PET film, screen printed silver on cellulose acetate propionate (CAP) showed 18% lower resistance value and, hence, better electrical properties[140]. Hao *et al.*[141] developed a multifunctional gelatin-alginate hydrogel-based soft sensor with improved sensing performance. The degradable sensor is able to sense very small changes in strain, temperature, heart rate, and pH and has also been explored for drug delivery application. Since the device is both degradable and recyclable, it can be reconstructed with new functions (Figure 7C-E). A polymer of methyl 1H-pyrrole-3-carboxylate monomer ("MPC polymer") was explored as energy storage material for supercapacitors. This polymer, both as a planar electrode and as a composite porous electrode with PLLA, demonstrated charge storage ability that was comparable to that of the pseudocapacitive conducting polymer PPY. In aqueous environment (37°C, pH 8.2), its application in a supercapacitor with an organic electrolyte revealed detectable evidence of deterioration in 8 h.[142]

Stimuli-responsive polymeric materials offer various transient modes in aqueous solutions and in ambient atmosphere with precise control over the start of degradation. These materials include temperature-sensitive cyclododecane (CDD) and methanesulfonic acid/wax[11], moisture responsive polyanhydrides[143,144], and photoacid generator/cyclic poly(phthalaldehyde) (PAG/cPPA) that respond to ultraviolet light[145]. To ensure that a gadget performs as intended for a particular amount of time, slow swelling polymers are preferred. Thus, metallic substrates serve as a good alternative option as they do not swell in biological fluids and, therefore, offer dimensional stability. The dissolution rate of thin foils of Fe, Mo, W, and Zn in PBS (pH 7.4 at 37°C) as substrates for transient electronics was found to be 0.08, 0.02, 0.15, and 3.5 μm/day[9], respectively.

6.2. Encapsulating materials

Depending on the intended use, desired device operational times may range from a few days to a few weeks or years. Such time frames are crucial for application in healthcare or clinical settings. Most of the printed electronic devices need to be protected through an encapsulation layer. Thus, selection of the right material for the encapsulation is paramount to achieve biodegradability. The electrically active components may quickly deteriorate in the presence of a high water permeation rate. When exposed to PBS at room temperature, Mg thin film enclosed in 5 m PLGA degrades within 10 min[15]. Tuning the physical and chemical properties of biopolymers, such as composition, thickness, crystallinity, and chemistry, can extend the lifetime. A carefully formulated polyanhydride allows the intracranial pressure sensor to operate steadily for up to 3 days[146] and silk fibroin with high crystallinity can extend the Mg thin film's lifetime to about 90 h[17]. An alternative option is the use of dissolvable oxides, although care should be taken to not use single-layered oxides. Depending on the deposition conditions, single-layer oxide quickly dissolves due to the presence of pinholes. In PBS, Mg with a 200 nm SiO_2 encapsulation dissolves within 1 min, but Mg that has layers of alternate SiO_2 and Si_3N_4 can last up to 10 days. According to the encapsulation studies for OLED devices, combining oxide layers and biopolymers is projected to significantly extend functional durations[147]. In addition, recent research has demonstrated that using a mono-Si thin film (1.5 mm) as the encapsulation layer can greatly increase the device's operating lifetime. Materials coated with Si NMs, such as Mg thin film, maintain their integrity after 60 days in PBS at 37°C[15].

7. Biodegradable and transient electronics

The field of biodegradable electronics falls under "green" electronics with the aim to develop electronic components and systems that have degradation and bioresorbability characteristics. Such systems should have degradation of over 80% in the presence of aqueous medium, temperature, humidity, oxygen, microorganisms, or radiations and should ideally convert to harmless substances. Bioresorbability is a subclass of biodegradability that refers to the safe breakdown of the material in the human body after performing its

function, thus obviating the need of physical removal. The first report on transient electronics was published by Hwang *et al.*[17] in 2012, where a platform technology was demonstrated. Since then, much research has been focused on developing biodegradable materials for electronic systems, investigating material degradation behavior and dissolution chemistries, modeling degradation, and creating fabrication techniques. Numerous biodegradable devices that operate reliably for a certain amount of time have been demonstrated for environmental applications, hardware security applications, and other applications such as biomedical implants and energy storage devices. Some of the examples for biomedical devices are implantable transient silicon-based devices with microheaters for thermal therapy[17], pressure and temperature sensors for the treatment of brain surgery and monitoring of cardiovascular activities[146], hydration sensors for wound healing applications[10], pH sensors[111], and devices for drug delivery applications[117,148,149]. Transient electronics protect the environment by reducing electronic waste. Some recent studies have focused on enzymatic degradation of PEDOT: PSS polymer[150] and development of an all-carbon thin-film paper-based transistor, which is 95% recyclable[151]. To make transient electronics self-sufficient, the development of transient batteries is a pre-requisite. In 2017, Zn-Cu galvanic cell was used to power a temperature sensor and a wireless communication device in the gastrointestinal tract of pigs[152]. Recently, a one-dimensional battery, consisting of chitosan as separator, MnO_2 as cathode and a fiber conductor coated with polydopamine/polypyrrole composite material as anode, was developed. Due to its high flexibility, it could be easily injected into the body to power a biosensor[153]. To further extend the application, Mg-Mo-based battery was used in wearable electronics to power an electronic watch and wearable health-care devices for electromyography applications[154]. Transient electronics are particularly useful for hardware secured devices containing sensitive information. For the purpose, an MgO-based device was developed which can degrade within 8 min in the presence of DI water at room temperature[155]. Similarly, a $CsPbBr_3$-based device was capable of dissolving in DI water within 60 s[156-158]. Focus has also been directed to develop high-performance degradable printed circuit boards (PCBs). In one of the early works, Huang *et al.* demonstrated transient PCB using different materials that dissolved into benign end products on exposure to water[67]. The multilayered PCB device used biodegradable metals such as Mg, W, and Zn for interconnects and PEO on a flexible sodium carboxymethylcellulose substrate. A plant-based biodegradable PCB was made from agricultural waste of natural cellulose[159]. The biocomposite used in the work softens in contact with hot water or in high humidity. In another work, the performance of PCBs made from biodegradable cellulose acetate and PLA was compared with those created on Flame-Retardant Class 4 (FR-4) substrates[160]. Bharath *et al.*[161] explored rice husk-epoxy resin as a potential candidate for PCB. Although the performance of the PCBs and devices is far from that of the conventional devices, yet they hold promise to bring sustainability in electronics and make it environmentally friendly. For device applications, the functional lifetime is defined by the degradation time, thickness of material layers, and water permeability of the encapsulation materials. External stimulus triggers, namely, moisture, light, temperature, and mechanical force, have also been explored to degrade the materials in mostly non-aqueous environments.

Most of the initial devices using biodegradable materials used conventional manufacturing techniques of lithography, etching, and vapor or chemical deposition. Electrospinning and transfer techniques have also been explored but have been less successful when it comes to repeatability. Despite there are very few reports using additive manufacturing (AM) techniques to print biodegradable materials, discussion on this topic based on droplet-based printing techniques and 3D micro-additive manufacturing techniques has been initiated in a few papers[162-164]. PEDOT: PSS was converted into ink and printed using inkjet printer, which uses a piezoelectric nozzle and is a well-known drop-on-demand technique[164]. In a recent work by Williams *et al.*,[151] the emerging AM technique of aerosol jet printing was explored to fabricate an all-carbon thin-film transistor employing biodegradable material inks of nanocellulose and carbon nanotubes on paper substrate. A conductive paste of Zn, PVP, glycerol, and methanol was found to be suitable to create interconnects for screen printing. By combining screen printing with hot rolling and photonic sintering, a high conductivity of 60,213.6 S/m was achieved[28]. It was reported that among all printing methods, aerosol jet printing has the best resolution (line width >10 m) and thus this technique offers better printing on a wide range of substrates and on 3D surfaces[164].

8. End of life of electronics

Increasing electronic waste is an obstacle in the path of circular economy. Only 20% of e-waste gets recycled and a majority of it ends up in landfills, contributing to environmental problem. Researchers are exploring biodegradable materials to develop transient electronics in an effort to reduce e-waste. These devices have the capacity to dissolve in aqueous solutions to produce harmless products or to self-destruct themselves after operating for a predetermined period of time. The aim is to

counterbalance the negative trends conveyed by the short life cycle of electronics.

As discussed in this review paper, biodegradable metals generally convert into their oxides in aqueous solutions, and in some cases, they are non-reactive; therefore, they can be recycled back for use in another device, an example is liquid metal[165,166]. Researchers have experimented with recovering polymers back from the solution or degrading them enzymatically. In a previous study, an electrochromic display fabricated using PEDOT: PSS electrochromic layer, a gelatin-based electrolyte, and Au electrodes deposited on a cellulose diacetate substrate was tested for biodegradability study in accordance with the international standard ISO 14855. It was found that 79% of the device was able to degrade in 9 weeks by the microorganisms. The remaining 20% was cellulose diacetate and small amounts of PEDOT: PSS, glycerol, and gelatin[150]. In another study by Kwon *et al.*,[167] Ag composite with polycaprolactone (Ag-PCL) was used as a degradable electronic ink. The composite was embedded with enzymes to catalyze the hydrolytic degradation of PCL. This technique was useful to separate the electronic components, which can be recycled even after months of storage with no observable loss in performance. An all-carbon thin-film paper-based transistor was designed for controllable decomposition where efficiency to recapture graphene and carbon nanotubes was more than 95%. All the recycled materials could be reprinted in the form of new transistors with nearly identical performance to the thin film transistors (TFTs) created from new ink[151].

Although researchers are working to make electronics more environmentally friendly by making them repairable, recyclable, or degradable so as to reduce the amount of e-waste, another significant challenge to focus on is incorporating the capability to quickly change a sensor or a component according to the need. This will eliminate the need to replace the entire device helping to further reduce the amount of waste produced and serving as both ecologically and economically viable options.

9. Challenges

Much effort has been put in studying and investigating the degradation of materials. However, the topics surrounding the breakdown of the emerging electronic materials and its effects on their performance are new. There are still many issues that need to be addressed so that the field can fully evolve.

(i) One of the main challenges in biodegradable materials is their commercialization and acceptance by the industry. The synthesized biodegradable materials fall short in comparison to their synthetic counterparts in technical and economic aspects.

(ii) The biodegradability of various emerging materials has been tested and demonstrated only at the laboratory scale. It is essential to establish their biodegradability at the industrial scale and also set up standards for their commercial adoption.

(iii) One major challenge is associated with synthesizing semiconducting and conducting biodegradable polymers that can find application in electronics and biomedical devices. To date, it is still challenging to retain the conductivity of biodegradable polymers while ensuring their functionality for the desired time. Two possible scenarios for solving the issue are either biomimicking the biodegradable natural materials for electronics properties or using novel chemistries to expand the library of biodegradable conducting polymers.

(iv) One of the roadblocks for biodegradable materials is their application, especially in biomedical devices. The electroresponsive and tissue engineering materials have unknown biodegradation profile *in vitro* and *in vivo*. A lot of questions surrounding scaffold degradation and integration of cells or tissues with decomposing scaffold remain unanswered.

10. Conclusions and outlook

Development of biodegradable materials can help solve issues of e-waste, a growing problem that alone cannot be solved by recycling and reusing. This review summarizes the most current biodegradable materials currently being researched for their use electronic devices and health-care solutions. The materials are comprehensively categorized and discussed according to their electrical conduction, namely, conductors, semiconductors, and insulators. Both natural and synthetic materials have been explored as substrates, electrodes, and active layers in many biodegradable devices. However, the field of biodegradable electronics is in its infancy, and the current biodegradable devices cannot compete with conventional devices in performance. Hence, there is a need to push research in the direction of exploring novel biodegradable materials that have better performance. The library also needs to expand to piezoelectric, piezoresistive, and energy materials to fully replace electronic circuitry in the future. Most biodegradation studies are limited to materials, and it is paramount to evaluate dissolution rates of materials with respect to their electrical performance. It is still unknown at what point biodegradable devices start to become unreliable. This review provides a comprehensive knowledge regarding the potential of fabricating green electronics that can be partially or fully degraded, thus paving way for sustainable electronics.

Acknowledgments

None.

Funding

The work is funded by the Villum Fonden grant (no: 37508).

Conflict of interest

The authors declare no conflicts of interest.

Author contributions

Conceptualization: Monisha Monisha and Shweta Agarwala
Writing – original draft: Monisha Monisha
Writing – review & editing: Monisha Monisha and Shweta Agarwala
All authors have read and agreed to the published version of the manuscript.

References

1. Forti V, Balde CP, Kuehr R, *et al.*, 2020, The Global E-waste Monitor 2020: Quantities, Flows and the Circular Economy Potential. Available from: https://ewastemonitor.info/gem-2020 [Last accessed on 2022 Jul 21].
2. Li R, Cheng H, Su Y, *et al.*, 2013, An analytical model of reactive diffusion for transient electronics. *Adv Funct Mater*, 23: 3106–3114.

   https://doi.org/10.1002/adfm.201203088
3. Yin L, Cheng H, Mao S, *et al.*, 2014, Dissolvable metals for transient electronics. *Adv Funct Mater*, 24: 645–658.

   https://doi.org/10.1002/adfm.201301847
4. Song G, Atrens A, 2003, Understanding magnesium corrosion a framework for improved alloy performance. *Adv Eng Mater*, 5: 837–858.

   https://doi.org/10.1002/adem.200310405
5. Li W, Liu Q, Zhang Y, *et al.*, 2020, Biodegradable materials and green processing for green electronics. *Adv Mater*, 32: 2001591.

   https://doi.org/10.1002/adma.202001591
6. Dagdeviren C, Hwang SW, Su Y, *et al.*, 2013, Transient, biocompatible electronics and energy harvesters based on ZnO. *Small*, 9: 3398–3404.

   https://doi.org/10.1002/smll.201300146
7. Oikawa H, 1975, Ellipsometric investigation of corrosion of deposited thin molybdenum film. *Jpn J Appl Phys*, 14: 629–635.

   https://doi.org/10.1143/jjap.14.629
8. Sherif ESM, Erasmus RM, Comins JD, 2010, *In situ* Raman spectroscopy and electrochemical techniques for studying corrosion and corrosion inhibition of iron in sodium chloride solutions. *Electrochim Acta*, 55: 3657–3663.

   https://doi.org/10.1016/j.electacta.2010.01.117
9. Kang SK, Hwang SW, Yu S, *et al.*, 2015, Biodegradable thin metal foils and spin-on glass materials for transient electronics. *Adv Funct Mater*, 25: 1789–1797.

   https://doi.org/10.1002/adfm.201403469
10. Hwang SW, Song JK, Huang X, *et al.*, 2014, High-performance biodegradable/transient electronics on biodegradable polymers. *Adv Mater*, 26: 3905–3911.

    https://doi.org/10.1002/adma.201306050
11. Kim BH, Kim JH, Persano L, *et al.*, 2017, Dry transient electronic systems by use of materials that sublime. *Adv Funct Mater*, 27: 1606008.

    https://doi.org/10.1002/adfm.201606008
12. Hwang SW, Park G, Edwards C, *et al.*, 2014, Dissolution chemistry and biocompatibility of single-crystalline silicon nanomembranes and associated materials for transient electronics. *ACS Nano*, 8: 5843–5851.

    https://doi.org/10.1021/nn500847g
13. Hwang SW, Park G, Cheng H, *et al.*, 2014, 25th anniversary article: Materials for high-performance biodegradable semiconductor devices. *Adv Mater*, 26: 1992–2000.

    https://doi.org/10.1002/adma.201304821
14. Yin L, Farimani AB, Min K, *et al.*, 2015, Mechanisms for hydrolysis of silicon nanomembranes as used in bioresorbable electronics. *Adv Mater*, 27: 1857–1864.

    https://doi.org/10.1002/adma.201404579
15. Lee YK, Yu KJ, Song E, *et al.*, 2017, Dissolution of monocrystalline silicon nanomembranes and their use as encapsulation layers and electrical interfaces in water-soluble electronics. *ACS Nano*, 11: 12562–12572.

    https://doi.org/10.1021/acsnano.7b06697
16. Yang SM, Shim JH, Cho HU, *et al.*, 2022, Hetero-integration of silicon nanomembranes with 2D materials for bioresorbable, wireless neurochemical system. *Adv Mater*, 34: 2108203.

    https://doi.org/10.1002/adma.202108203
17. Hwang SW, Tao H, Kim DH, *et al.*, 2012, A physically transient form of silicon electronics. *Science*, 337: 1640–1644.

    https://doi.org/10.1126/science.1226325
18. Seidel H, Csepregi L, Heuberger A, *et al.*, 1990, Anisotropic etching of crystalline silicon in alkaline solutions: II. Influence of dopants. *J Electrochem Soc*, 137: 3626–3632.

    https://doi.org/10.1149/1.2086278
19. Kang SK, Park G, Kim K, *et al.*, 2015, Dissolution chemistry

and biocompatibility of silicon- and germanium-based semiconductors for transient electronics. *ACS Appl Mater Interfaces*, 7: 9297–9305.

https://doi.org/10.1021/acsami.5b02526

20. Kang SK, Hwang SW, Cheng H, *et al.*, 2014, Dissolution behaviors and applications of silicon oxides and nitrides in transient electronics. *Adv Funct Mater*, 24: 4427–4434.

https://doi.org/10.1002/adfm.201304293

21. Hwang SW, Kang SK, Huang X, *et al.*, 2015, Materials for programmed, functional transformation in transient electronic systems. *Adv Mater*, 27: 47–52.

https://doi.org/10.1002/adma.201403051

22. Manivasagam G, Suwas S, 2014, Biodegradable Mg and Mg based alloys for biomedical implants. *Mater Sci Technol*, 30: 515–520.

https://doi.org/10.1179/1743284713Y.0000000500

23. Patrick E, Orazem ME, Sanchez JC, *et al.*, 2011, Corrosion of tungsten microelectrodes used in neural recording applications. *J Neurosci Methods*, 198: 158–171.

https://doi.org/10.1016/j.jneumeth.2011.03.012

24. Dahiya AS, Zumeit A, Christou A, *et al.*, 2022, High-performance n-channel printed transistors on biodegradable substrate for transient electronics. *Adv Electron Mater*, 8: 2200098.

https://doi.org/10.1002/aelm.202200098

25. Feng S, Tian Z, Wang J, *et al.*, 2019, Laser sintering of Zn microparticles and its application in printable biodegradable electronics. *Adv Electron Mater*, 5: 1800693.

https://doi.org/10.1002/aelm.201800693

26. Li J, Liu J, Lu W, *et al.*, 2021, Water-sintered transient nanocomposites used as electrical interconnects for dissolvable consumer electronics. *ACS Appl Mater Interfaces*, 13: 32136–32148.

https://doi.org/10.1021/acsami.1c07102

27. Pandey V, Haider T, Jain P, *et al.*, 2020, Silk as a leading-edge biological macromolecule for improved drug delivery. *J Drug Deliv Sci Technol*, 55: 101294.

https://doi.org/10.1016/j.jddst.2019.101294

28. Li J, Luo S, Liu J, *et al.*, 2018, Processing techniques for bioresorbable nanoparticles in fabricating flexible conductive interconnects. *Materials*, 11: 1102.

https://doi.org/10.3390/ma11071102

29. Li H, Peng Q, Li X, *et al.*, 2014, Microstructures, mechanical and cytocompatibility of degradable Mg-Zn based orthopedic biomaterials. *Mater Des*, 58: 43–51.

https://doi.org/10.1016/j.matdes.2014.01.031

30. Wang S, Guan S, Wang J, *et al.*, 2017, Fabrication and characterization of conductive poly (3,4-ethylenedioxythiophene) doped with hyaluronic acid/poly (l-lactic acid) composite film for biomedical application. *J Biosci Bioeng*, 123: 116–125.

https://doi.org/10.1016/j.jbiosc.2016.07.010

31. Li L, Ge J, Guo B, *et al.*, 2014, *In situ* forming biodegradable electroactive hydrogels. *Polym Chem*, 5: 2880–2890.

https://doi.org/10.1039/C3PY01634J

32. Tran RT, Thevenot P, Gyawali D, *et al.*, 2010, Synthesis and characterization of a biodegradable elastomer featuring a dual crosslinking mechanism. *Soft Matter*, 6: 2449–2461.

https://doi.org/10.1039/C001605E

33. Jia X, Wang C, Ranganathan V, *et al.*, 2017, A biodegradable thin-film magnesium primary battery using silk fibroin-ionic liquid polymer electrolyte. *ACS Energy Lett*, 2: 831–836.

https://doi.org/10.1021/acsenergylett.7b00012

34. Zhou J, Zhang R, Xu R, *et al.*, 2022, Super-assembled hierarchical cellulose aerogel-gelatin solid electrolyte for implantable and biodegradable zinc ion battery. *Adv Funct Mater*, 32: 2111406.

https://doi.org/10.1002/adfm.202111406

35. Boutry CM, Nguyen A, Lawal QO, *et al.*, 2015, Fully Biodegradable Pressure Sensor, Viscoelastic Behavior of PGS Dielectric Elastomer Upon Degradation. 2015 IEEE SENSORS, 1-4 Nov.

36. Zhao D, Wu J, Chou DT, *et al.*, 2020, Visual hydrogen mapping sensor for noninvasive monitoring of bioresorbable magnesium implants *in vivo*. *JOM*, 72: 1851–1858.

https://doi.org/10.1007/s11837-020-04052-4

37. Curry EJ, Ke K, Chorsi MT, *et al.*, 2018, Biodegradable piezoelectric force sensor. *Proc Natl Acad Sci*, 115: 909–914.

https://doi.org/10.1073/pnas.1710874115

38. Suvarnaphaet P, Sasivimolkul S, Sukkasem C, *et al.*, 2019, *Biodegradable Electrode Patch Made of Graphene/PHA for ECG Detecting Applications*, 2019 12th Biomedical Engineering International Conference (BMEiCON), 19-22 Nov.

39. Zhu M, Jia C, Wang Y, *et al.*, 2018, Isotropic paper directly from anisotropic wood: Top-down green transparent substrate toward biodegradable electronics. *ACS Appl Mater Interfaces*, 10: 28566–28571.

https://doi.org/10.1021/acsami.8b08055

40. Liu H, Jiang H, Du F, *et al.*, 2017, Flexible and degradable paper-based strain sensor with low cost. *ACS Sustain Chem Eng*, 5: 10538–10543.

https://doi.org/10.1021/acssuschemeng.7b02540

41. Abdelkader AM, Karim N, Vallés C, *et al.*, 2017, Ultraflexible and robust graphene supercapacitors printed on textiles for

wearable electronics applications. *2D Materials*, 4: 035016.

https://doi.org/10.1088/2053-1583/aa7d71

42. Edupuganti V, Solanki R, 2016, Fabrication, characterization, and modeling of a biodegradable battery for transient electronics. *J Power Sources*, 336: 447–454.

https://doi.org/10.1016/j.jpowsour.2016.11.004

43. Zhang Q, Liang Q, Rogers JA, 2020, Water-soluble energy harvester as a promising power solution for temporary electronic implants. *APL Mater*, 8: 120701.

https://doi.org/10.1063/5.0031151

44. Krężel A, Maret W, 2016, The biological inorganic chemistry of zinc ions. *Arch Biochem Biophys*, 611: 3–19.

https://doi.org/10.1016/j.abb.2016.04.010

45. Presuel-Moreno FJ, Jakab MA, Scully JR, 2005, Inhibition of the oxygen reduction reaction on copper with cobalt, cerium, and molybdate ions. *J Electrochem Soc*, 152: B376.

https://doi.org/10.1149/1.1997165

46. Tolouei R, Harrison J, Paternoster C, *et al.*, 2016, The use of multiple pseudo-physiological solutions to simulate the degradation behavior of pure iron as a metallic resorbable implant: A surface-characterization study. *Phys Chem Chem Phys*, 18: 19637–19646.

https://doi.org/10.1039/C6CP02451C

47. Zhang T, Tao Z, Chen J, 2014, Magnesium–air batteries: From principle to application. *Mater Horiz*, 1: 196–206.

https://doi.org/10.1039/C3MH00059A

48. Yu X, Shou W, Mahajan BK, *et al.*, 2018, Materials, processes, and facile manufacturing for bioresorbable electronics: A review. *Adv Mater*, 30: 1707624.

https://doi.org/10.1002/adma.201707624

49. Fernandes C, Taurino I, 2022, Biodegradable molybdenum (Mo) and tungsten (W) devices: One step closer towards fully-transient biomedical implants. *Sensors* (*Basel*), 22: 3062.

https://doi.org/10.3390/s22083062

50. Laing PG, 1979, Clinical experience with prosthetic materials: Historical perspectives, current problems, and future directions. USA: ASTM Int, 199–211.

https://doi.org/10.1520/STP35945S

51. Cao Y, Wang S, Lv J, *et al.*, 2022, Fully physically transient volatile memristor based on mg/magnesium oxide for biodegradable neuromorphic electronics. *IEEE Trans Electron Devices*, 69: 3118–3123.

https://doi.org/10.1109/TED.2022.3166868

52. Xiang W, Hongmei L, Xinlin L, *et al.*, 2007, Effect of cooling rate and composition on microstructures and properties of Zn-Mg alloys. *Trans Nonferrous Metals Soc China*, 17: 122–125.

53. Han WB, Yang SM, Rajaram K, *et al.*, 2022, Materials and fabrication strategies for biocompatible and biodegradable conductive polymer composites toward bio-integrated electronic systems. *Adv Sustain Syst*, 6: 2100075.

https://doi.org/10.1002/adsu.202100075

54. Machado JM, Karasz FE, Lenz RW, 1988, Electrically conducting polymer blends. *Polymer*, 29: 1412–1417.

https://doi.org/10.1016/0032-3861(88)90304-7

55. Cao Y, Smith P, Heeger AJ, 1992, Counter-ion induced processibility of conducting polyaniline and of conducting polyblends of polyaniline in bulk polymers. *Synth Met*, 48: 91–97.

https://doi.org/10.1016/0379-6779(92)90053-L

56. Knackstedt MA, Roberts AP, 1996, Morphology and macroscopic properties of conducting polymer blends. *Macromolecules*, 29: 1369–1371.

https://doi.org/10.1021/ma951295h

57. Worfolk BJ, Andrews SC, Park S, *et al.*, 2015, Ultrahigh electrical conductivity in solution-sheared polymeric transparent films. *Proc Natl Acad Sci*, 112: 14138–14143.

https://doi.org/10.1073/pnas.1509958112

58. Wang YF, Sekine T, Takeda Y, *et al.*, 2020, Fully printed PEDOT: PSS-based temperature sensor with high humidity stability for wireless healthcare monitoring. *Sci Rep*, 10: 2467.

https://doi.org/10.1038/s41598-020-59432-2

59. Shi G, Rouabhia M, Wang Z, *et al.*, 2004, A novel electrically conductive and biodegradable composite made of polypyrrole nanoparticles and polylactide. *Biomaterials*, 25: 2477–2488.

https://doi.org/10.1016/j.biomaterials.2003.09.032

60. Pradhan S, Yadavalli VK, 2021, Photolithographically printed flexible silk/PEDOT: PSS temperature sensors. *ACS Appl Electron Mater*, 3: 21–29.

https://doi.org/10.1021/acsaelm.0c01017

61. Lawes S, Sun Q, Lushington A, *et al.*, 2017, Inkjet-printed silicon as high performance anodes for Li-ion batteries. *Nano Energy*, 36: 313–321.

https://doi.org/10.1016/j.nanoen.2017.04.041

62. Li M, Guo Y, Wei Y, *et al.*, 2006, Electrospinning polyaniline-contained gelatin nanofibers for tissue engineering applications. *Biomaterials*, 27: 2705–2715.

https://doi.org/10.1016/j.biomaterials.2005.11.037

63. Jeong SI, Jun ID, Choi MJ, *et al.*, 2008, Development of electroactive and elastic nanofibers that contain polyaniline and poly(L-lactide-co-ε-caprolactone) for the control of cell adhesion. *Macromol Biosci*, 8: 627–637.

https://doi.org/10.1002/mabi.200800005

64. Subramanian A, Krishnan UM, Sethuraman S, 2012, Axially aligned electrically conducting biodegradable nanofibers for neural regeneration. *J Mater Sci Mater Med*, 23: 1797–1809.

https://doi.org/10.1007/s10856-012-4654-y

65. Mahajan BK, Ludwig B, Shou W, *et al.*, 2018, Aerosol printing and photonic sintering of bioresorbable zinc nanoparticle ink for transient electronics manufacturing. *Sci China Inf Sci*, 61: 060412.

https://doi.org/10.1007/s11432-018-9366-5

66. Li J, Xu H, Zhang Z, *et al.*, 2020, Anhydride-assisted spontaneous room temperature sintering of printed bioresorbable electronics. *Adv Funct Mater*, 30: 1905024.

https://doi.org/10.1002/adfm.201905024

67. Huang X, Liu Y, Hwang SW, *et al.*, 2014, Biodegradable materials for multilayer transient printed circuit boards. *Adv Mater*, 26: 7371–7377.

https://doi.org/10.1002/adma.201403164

68. Iwai H, Ohmi SI, 2002, Silicon integrated circuit technology from past to future. *Microelectron Reliab*, 42: 465–491.

https://doi.org/10.1016/S0026-2714(02)00032-X

69. Snell AJ, Spear WE, Le Comber PG, *et al.*, 1981, Application of amorphous silicon field effect transistors in integrated circuits. *Appl Phys A*, 26: 83–86.

https://doi.org/10.1007/BF00616653

70. Bowman DR, Hammond RB, Dutton RW, 1985, Polycrystalline-silicon integrated photoconductors for picosecond pulsing and gating. *IEEE Electron Device Lett*, 6: 502–504.

https://doi.org/10.1109/EDL.1985.26209

71. Guha S, Yang J, Banerjee A, 2000, Amorphous silicon alloy photovoltaic research—present and future. *Prog Photovolt: Res Appl*, 8: 141–150.

https://doi.org/10.1002/(SICI)1099-159X(200001/02)8:1<141:AID-PIP305>3.0.CO;2-I

72. Kang SK, Koo J, Lee YK, *et al.*, 2018, Advanced materials and devices for bioresorbable electronics. *Acc Chem Res*, 51: 988–998.

https://doi.org/10.1021/acs.accounts.7b00548

73. Fu KK, Wang Z, Dai J, *et al.*, 2016, Transient electronics: Materials and devices. *Chem Mater*, 28: 3527–3539.

https://doi.org/10.1021/acs.chemmater.5b04931

74. Li R, Wang L, Kong D, *et al.*, 2018, Recent progress on biodegradable materials and transient electronics. *Bioact Mater*, 3: 322–333.

https://doi.org/10.1016/j.bioactmat.2017.12.001

75. Li R, Wang L, Yin L, 2018, Materials and devices for biodegradable and soft biomedical electronics. *Materials*, 11: 2108.

76. Madrigal MM, Giannotti MI, Oncins G, *et al.*, 2013, Bioactive nanomembranes of semiconductor polythiophene and thermoplastic polyurethane: Thermal, nanostructural and nanomechanical properties. *Polym Chem*, 4: 568–583.

https://doi.org/10.1039/c2py20654d

77. Pérez-Madrigal MM, Giannotti MI, Armelin E, *et al.*, 2014, Electronic, electric and electrochemical properties of bioactive nanomembranes made of polythiophene: Thermoplastic polyurethane. *Polym Chem*, 5: 1248–1257.

https://doi.org/10.1039/C3PY01313H

78. Lei T, Guan M, Liu J, *et al.*, 2017, Biocompatible and totally disintegrable semiconducting polymer for ultrathin and ultralightweight transient electronics. *Proc Natl Acad Sci*, 114: 5107–5112.

https://doi.org/10.1073/pnas.1701478114

79. Xu C, Huang Y, Yepez G, *et al.*, 2016, Development of dopant-free conductive bioelastomers. *Sci Rep*, 6: 34451.

https://doi.org/10.1038/srep34451

80. Mostert AB, Powell BJ, Pratt FL, *et al.*, 2012, Role of semiconductivity and ion transport in the electrical conduction of melanin. *Proc Natl Acad Sci*, 109: 8943–8947.

https://doi.org/10.1073/pnas.1119948109

81. Bettinger CJ, Bruggeman JP, Misra A, *et al.*, 2009, Biocompatibility of biodegradable semiconducting melanin films for nerve tissue engineering. *Biomaterials*, 30: 3050–3057.

https://doi.org/10.1016/j.biomaterials.2009.02.018

82. Irimia-Vladu M, Głowacki ED, Troshin PA, *et al.*, 2012, Indigo a natural pigment for high performance ambipolar organic field effect transistors and circuits. *Adv Mater*, 24: 375–380.

https://doi.org/10.1002/adma.201102619

83. Ramachandran GK, Tomfohr JK, Li J, *et al.*, 2003, Electron transport properties of a carotene molecule in a metal-(single molecule)-metal junction. *J Phys Chem B*, 107: 6162–6169.

https://doi.org/10.1021/jp0343786

84. Irimia-Vladu M, Troshin PA, Reisinger M, *et al.*, 2010, Biocompatible and biodegradable materials for organic field-effect transistors. *Adv Funct Mater*, 20: 4069–4076.

https://doi.org/10.1002/adfm.201001031

85. Guo B, Finne-Wistrand A, Albertsson AC, 2010, Enhanced electrical conductivity by macromolecular architecture: Hyperbranched electroactive and degradable block copolymers based on poly(ε-caprolactone) and aniline

pentamer. *Macromolecules*, 43: 4472–4480.

https://doi.org/10.1021/ma100530k

86. Cui H, Liu Y, Deng M, *et al.*, 2012, Synthesis of biodegradable and electroactive tetraaniline grafted poly(ester amide) copolymers for bone tissue engineering. *Biomacromolecules*, 13: 2881–2889.

https://doi.org/10.1021/bm300897j

87. Champion JA, Walker A, Mitragotri S, 2008, Role of particle size in phagocytosis of polymeric microspheres. *Pharm Res*, 25: 1815–1821.

https://doi.org/10.1007/s11095-008-9562-y

88. Temenoff JS, Mikos AG, 2008, *Biomaterials: The Intersection of Biology and Materials Science*. Pearson/Prentice Hall, London, United Kingdom.

89. Shou W, Mahajan BK, Ludwig B, *et al.*, 2017, Low-cost manufacturing of bioresorbable conductors by evaporation–condensation-mediated laser printing and sintering of Zn nanoparticles. *Adv Mater*, 29: 1700172.

https://doi.org/10.1002/adma.201700172

90. Feng S, Cao S, Tian Z, *et al.*, 2019, Maskless patterning of biodegradable conductors by selective laser sintering of microparticle inks and its application in flexible transient electronics. *ACS Appl Mater Interfaces*, 11: 45844–45852.

https://doi.org/10.1021/acsami.9b14431

91. Shin SR, Farzad R, Tamayol A, *et al.*, 2016, A bioactive carbon nanotube-based ink for printing 2D and 3D flexible electronics. *Adv Mater*, 28: 3280–3289.

https://doi.org/10.1002/adma.201506420

92. Leng T, Huang X, Chang K, *et al.*, 2016, Graphene nanoflakes printed flexible meandered-line dipole antenna on paper substrate for low-cost RFID and sensing applications. *IEEE Antennas Wirel Propag Lett*, 15: 1565–1568.

https://doi.org/10.1109/LAWP.2016.2518746

93. Deshmukh K, Ahamed MB, Deshmukh RR, *et al.*, 2017, Newly developed biodegradable polymer nanocomposites of cellulose acetate and Al_2O_3 nanoparticles with enhanced dielectric performance for embedded passive applications. *J Mater Sci Mater Electron*, 28: 973–986.

https://doi.org/10.1007/s10854-016-5616-9

94. Zeng X, Deng L, Yao Y, *et al.*, 2016, Flexible dielectric papers based on biodegradable cellulose nanofibers and carbon nanotubes for dielectric energy storage. *J Mater Chem C*, 4: 6037–6044.

https://doi.org/10.1039/C6TC01501H

95. Mukai Y, Suh M, 2020, Relationships between structure and microwave dielectric properties in cotton fabrics. *Mater Res Express*, 7: 015105.

https://doi.org/10.1088/2053-1591/ab653c

96. Liu Z, Liang T, Xin Y, *et al.*, 2021, Natural bamboo leaves as dielectric layers for flexible capacitive pressure sensors with adjustable sensitivity and a broad detection range. *RSC Adv*, 11: 17291–17300.

https://doi.org/10.1039/D1RA03207K

97. Larguech S, Triki A, Ramachandran M, *et al.*, 2021, Dielectric properties of jute fibers reinforced poly(lactic acid)/poly(butylene succinate) blend matrix. *J Polym Environ*, 29: 1240–1256.

https://doi.org/10.1007/s10924-020-01927-0

98. Ivanovska A, Cerovic D, Tadic N, *et al.*, 2019, Sorption and dielectric properties of jute woven fabrics: Effect of chemical composition. *Ind Crops Prod*, 140: 111632.

https://doi.org/10.1016/j.indcrop.2019.111632

99. Doddashamachar M, Setty RNV, Reddy MVH, *et al.*, 2022, Dielectric properties of banana fiber filled polypropylene composites: Effect of coupling agent. *Fibers Polym*, 23: 1387–1395.

https://doi.org/10.1007/s12221-022-4395-6

100. Joseph S, Thomas S, 2008, Electrical properties of banana fiber-reinforced phenol formaldehyde composites. *J Appl Polym Sci*, 109: 256–263.

https://doi.org/10.1002/app.27452

101. Hemstreet JM, 1982, Dielectric constant of cotton. *J Electrostat*, 13: 345–353.

https://doi.org/10.1016/0304-3886(82)90052-3

102. Jayamani E, Hamdan S, Rahman MR, *et al.*, 2014, Comparative study of dielectric properties of hybrid natural fiber composites. *Proc Eng*, 97: 536–544.

https://doi.org/10.1016/j.proeng.2014.12.280

103. Boutry CM, Nguyen A, Lawal QO, *et al.*, 2015, A sensitive and biodegradable pressure sensor array for cardiovascular monitoring. *Adv Mater*, 27: 6954–6961.

https://doi.org/10.1002/adma.201502535

104. Barone C, Maccagnani P, Dinelli F, *et al.*, 2022, Electrical conduction and noise spectroscopy of sodium-alginate gold-covered ultrathin films for flexible green electronics. *Sci Rep*, 12: 9861.

https://doi.org/10.1038/s41598-022-14030-2

105. Guo J, Liu J, Yang B, *et al.*, 2015, Low-voltage transient/biodegradable transistors based on free-standing sodium alginate membranes. *IEEE Electron Device Lett*, 36: 576–578.

https://doi.org/10.1109/LED.2015.2424982

106. Kumar R, Ranwa S, Kumar G, 2020, Biodegradable flexible substrate based on chitosan/PVP blend polymer for disposable electronics device applications. *J Phys Chem B*, 124: 149–155.

https://doi.org/10.1021/acs.jpcb.9b08897

107. Peng X, Dong K, Zhang Y, *et al.*, 2022, Sweat-permeable, biodegradable, transparent and self-powered chitosan-based electronic skin with ultrathin elastic gold nanofibers. *Adv Funct Mater*, 32: 2112241.

https://doi.org/10.1002/adfm.202112241

108. Baumgartner M, Hartmann F, Drack M, *et al.*, 2020, Resilient yet entirely degradable gelatin-based biogels for soft robots and electronics. *Nat Mater*, 19: 1102–1109.

https://doi.org/10.1038/s41563-020-0699-3

109. Wang C, Yokota T, Someya T, 2021, Natural biopolymer-based biocompatible conductors for stretchable bioelectronics. *Chem Rev*, 121: 2109–2146.

https://doi.org/10.1021/acs.chemrev.0c00897

110. Yang Y, Sun H, Zhao X, *et al.*, 2022, High-mobility fungus-triggered biodegradable ultraflexible organic transistors. *Adv Sci*, 9: 2105125.

https://doi.org/10.1002/advs.202105125

111. Hwang SW, Lee CH, Cheng H, *et al.*, 2015, Biodegradable elastomers and silicon nanomembranes/nanoribbons for stretchable, transient electronics, and biosensors. *Nano Lett*, 15: 2801–2808.

https://doi.org/10.1021/nl503997m

112. Jung YH, Chang TH, Zhang H, *et al.*, 2015, High-performance green flexible electronics based on biodegradable cellulose nanofibril paper. *Nat Commun*, 6: 7170.

https://doi.org/10.1038/ncomms8170

113. Jin SH, Kang SK, Cho IT, *et al.*, 2015, Water-soluble thin film transistors and circuits based on amorphous indium–gallium–zinc oxide. *ACS Appl Mater Interfaces*, 7: 8268–8274.

https://doi.org/10.1021/acsami.5b00086

114. Liu Q, Jiang L, Shi R, *et al.*, 2012, Synthesis, preparation, *in vitro* degradation, and application of novel degradable bioelastomers a review. *Prog Polym Sci*, 37: 715–765.

https://doi.org/10.1016/j.progpolymsci.2011.11.001

115. Nijst CL, Bruggeman JP, Karp JM, *et al.*, 2007, Synthesis and characterization of photocurable elastomers from poly(glycerol-co-sebacate). *Biomacromolecules*, 8: 3067–3073.

https://doi.org/10.1021/bm070423u

116. Benfenati V, Toffanin S, Capelli R, *et al.*, 2010, A silk platform that enables electrophysiology and targeted drug delivery in brain astroglial cells. *Biomaterials*, 31: 7883–7891.

https://doi.org/10.1016/j.biomaterials.2010.07.013

117. Tao H, Hwang SW, Marelli B, *et al.*, 2014, Silk-based resorbable electronic devices for remotely controlled therapy and *in vivo* infection abatement. *Proc Natl Acad Sci*, 111: 17385–17389.

https://doi.org/10.1073/pnas.1407743111

118. Zhu M, Liu Y, Jiang F, *et al.*, 2020, Combined silk fibroin microneedles for insulin delivery. *ACS Biomater Sci Eng*, 6: 3422–3429.

https://doi.org/10.1021/acsbiomaterials.0c00273

119. Kim HJ, Kim JH, Jun KW, *et al.*, 2016, Silk nanofiber-networked bio-triboelectric generator: silk bio-TEG. *Adv Energy Mater*, 6: 1502329.

https://doi.org/10.1002/aenm.201502329

120. Mi HY, Li H, Jing X, *et al.*, 2020, Silk and silk composite aerogel-based biocompatible triboelectric nanogenerators for efficient energy harvesting. *Ind Eng Chem Res*, 59: 12399–12408.

https://doi.org/10.1021/acs.iecr.0c01117

121. Ye C, Dong S, Ren J, *et al.*, 2019, Ultrastable and high-performance silk energy harvesting textiles. *Nanomicro Lett*, 12: 12.

https://doi.org/10.1007/s40820-019-0348-z

122. Lee CP, Lai KY, Lin CA, *et al.*, 2017, A paper-based electrode using a graphene dot/PEDOT: PSS composite for flexible solar cells. *Nano Energy*, 36: 260–267.

https://doi.org/10.1016/j.nanoen.2017.04.044

123. Castro-Hermosa S, Dagar J, Marsella A, *et al.*, 2017, Perovskite solar cells on paper and the role of substrates and electrodes on performance. *IEEE Electron Device Lett*, 38: 1278–1281.

https://doi.org/10.1109/LED.2017.2735178

124. Jia C, Li T, Chen C, *et al.*, 2017, Scalable, anisotropic transparent paper directly from wood for light management in solar cells. *Nano Energy*, 36: 366–373.

https://doi.org/10.1016/j.nanoen.2017.04.059

125. Jayaraman E, Iyer SS, 2020, Organic photovoltaic modules built on paper substrates. *Adv Mater Technol*, 5: 2000664.

https://doi.org/10.1002/admt.202000664

126. Cinti S, Colozza N, Cacciotti I, *et al.*, 2018, Electroanalysis moves towards paper-based printed electronics: Carbon black nanomodified inkjet-printed sensor for ascorbic acid detection as a case study. *Sens Actuators B Chem*, 265: 155–160.

https://doi.org/10.1016/j.snb.2018.03.006

127. Hui CY, Liu M, Li Y, *et al.*, 2018, A paper sensor printed with multifunctional bio/nano materials. *Angew Chem Int Ed*, 57: 4549–4553.

https://doi.org/10.1002/anie.201712903

128. Tao LQ, Zhang KN, Tian H, *et al.*, 2017, Graphene-paper pressure sensor for detecting human motions. *ACS Nano*, 11: 8790–8795.

https://doi.org/10.1021/acsnano.7b02826

129. Carvalho JT, Dubceac V, Grey P, *et al.*, 2019, Fully printed zinc oxide electrolyte-gated transistors on paper. *Nanomaterials*, 9: 169.

130. Lee CJ, Chang YC, Wang LW, *et al.*, 2019, Biodegradable materials for organic field-effect transistors on a paper substrate. *IEEE Electron Device Lett*, 40: 236–239.

https://doi.org/10.1109/LED.2018.2890618

131. Raghuwanshi V, Bharti D, Mahato AK, *et al.*, 2019, Solution-processed organic field-effect transistors with high performance and stability on paper substrates. *ACS Appl Mater Interfaces*, 11: 8357–8364.

https://doi.org/10.1021/acsami.8b21404

132. Zschieschang U, Klauk H, 2019, Organic transistors on paper: A brief review. *J Mater Chem C*, 7: 5522–5533.

https://doi.org/10.1039/C9TC00793H

133. Mohammadifar M, Yazgan I, Zhang J, *et al.*, 2018, Green biobatteries: Hybrid paper-polymer microbial fuel cells. *Adv Sustain Syst*, 2: 1800041.

https://doi.org/10.1002/adsu.201800041

134. Kim S, Georgiadis A, Tentzeris MM, 2018, Design of inkjet-printed RFID-based sensor on paper: single- and dual-tag sensor topologies. *Sensors* (*Basel*), 18: 1958.

135. Wang Y, Yan C, Cheng SY, *et al.*, 2019, Flexible RFID tag metal antenna on paper-based substrate by inkjet printing technology. *Adv Funct Mater*, 29: 1902579.

https://doi.org/10.1002/adfm.201902579

136. Zhu H, Fang Z, Preston C, *et al.*, 2014, Transparent paper: Fabrications, properties, and device applications. *Energy Environ Sci*, 7: 269–287.

https://doi.org/10.1039/C3EE43024C

137. Hsieh MC, Kim C, Nogi M, *et al.*, 2013, Electrically conductive lines on cellulose nanopaper for flexible electrical devices. *Nanoscale*, 5: 9289–9295.

https://doi.org/10.1039/C3NR01951A

138. Miller RA, Brady JM, Cutright DE, 1977, Degradation rates of oral resorbable implants (polylactates and polyglycolates): Rate modification with changes in PLA/PGA copolymer ratios. *J Biomed Mater Res*, 11: 711–719.

https://doi.org/10.1002/jbm.820110507

139. Najafabadi AH, Tamayol A, Annabi N, *et al.*, 2014, Biodegradable nanofibrous polymeric substrates for generating elastic and flexible electronics. *Adv Mater*, 26: 5823–5830.

https://doi.org/10.1002/adma.201401537

140. Luoma E, Välimäki M, Ollila J, *et al.*, 2022, Bio-based polymeric substrates for printed hybrid electronics. *Polymers* (*Basel*), 14: 1863.

https://doi.org/10.3390/polym14091863

141. Hao XP, Zhang CW, Zhang XN, *et al.*, 2022, Healable, recyclable, and multifunctional soft electronics based on biopolymer hydrogel and patterned liquid metal. *Small*, 18: 2201643.

https://doi.org/10.1002/smll.202201643

142. Moon J, Diaz V, Patel D, *et al.*, 2022, Dissolvable conducting polymer supercapacitor for transient electronics. *Org Electron*, 101: 106412.

https://doi.org/10.1016/j.orgel.2021.106412

143. Gao Y, Zhang Y, Wang X, *et al.*, 2017, Moisture-triggered physically transient electronics. *Sci Adv*, 3: e1701222.

https://doi.org/10.1126/sciadv.1701222

144. Park CW, Kang SK, Hernandez HL, *et al.*, 2015, Thermally triggered degradation of transient electronic devices. *Adv Mater*, 27: 3783–3788.

https://doi.org/10.1002/adma.201501180

145. Hernandez HL, Kang SK, Lee OP, *et al.*, 2014, Triggered transience of metastable poly(phthalaldehyde) for transient electronics. *Adv Mater*, 26: 7637–7642.

https://doi.org/10.1002/adma.201403045

146. Kang SK, Murphy RK, Hwang SW, *et al.*, 2016, Bioresorbable silicon electronic sensors for the brain. *Nature*, 530: 71–76.

https://doi.org/10.1038/nature16492

147. Park S, Yun WM, Kim LH, *et al.*, 2013, Inorganic/organic multilayer passivation incorporating alternating stacks of organic/inorganic multilayers for long-term air-stable organic light-emitting diodes. *Org Electron*, 14: 3385–3391.

https://doi.org/10.1016/j.orgel.2013.09.045

148. Feiner R, Fleischer S, Shapira A, *et al.*, 2018, Multifunctional degradable electronic scaffolds for cardiac tissue engineering. *J Control Release*, 281: 189–195.

https://doi.org/10.1016/j.jconrel.2018.05.023

149. Son D, Lee J, Lee DJ, *et al.*, 2015, Bioresorbable electronic stent integrated with therapeutic nanoparticles for endovascular diseases. *ACS Nano*, 9: 5937–5946.

https://doi.org/10.1021/acsnano.5b00651

150. Pietsch M, Schlisske S, Held M, *et al.*, 2020, Biodegradable inkjet-printed electrochromic display for sustainable short-lifecycle electronics. *J Mater Chem C*, 8: 16716–16724.

https://doi.org/10.1039/D0TC04627B

151. Williams NX, Bullard G, Brooke N, *et al.*, 2021, Printable and recyclable carbon electronics using crystalline nanocellulose dielectrics. *Nat Electron*, 4: 261–268.

https://doi.org/10.1038/s41928-021-00574-0

152. Nadeau P, El-Damak D, Glettig D, *et al.*, 2017, Prolonged energy harvesting for ingestible devices. *Nat Biomed Eng*, 1: 22.

https://doi.org/10.1038/s41551-016-0022

153. Mei T, Wang C, Liao M, *et al.*, 2021, A biodegradable and rechargeable fiber battery. *J Mater Chem A*, 9: 10104–10109.

https://doi.org/10.1039/D1TA01507A

154. Wang Z, Li X, Yang Z, *et al.*, 2021, Fully transient stretchable fruit-based battery as safe and environmentally friendly power source for wearable electronics. *EcoMat*, 3: e12073.

https://doi.org/10.1002/eom2.12073

155. Sun J, Wang H, Song F, *et al.*, 2018, Physically transient threshold switching device based on magnesium oxide for security application. *Small*, 14: 1800945.

https://doi.org/10.1002/smll.201800945

156. Lu L, Yang Z, Meacham K, *et al.*, 2018, Biodegradable monocrystalline silicon photovoltaic microcells as power supplies for transient biomedical implants. *Adv Energy Mater*, 8: 1703035.

https://doi.org/10.1002/aenm.201703035

157. Song F, Wang H, Sun J, *et al.*, 2018, ZnO-based physically transient and bioresorbable memory on silk protein. *IEEE Electron Device Lett*, 39: 31–34.

https://doi.org/10.1109/LED.2017.2774842

158. Wang H, Zhu B, Ma X, *et al.*, 2016, Physically transient resistive switching memory based on silk protein. *Small*, 12: 2715–2719.

https://doi.org/10.1002/smll.201502906

159. Guna VK, Murugesan G, Basavarajaiah BH, *et al.*, 2016, Plant-based completely biodegradable printed circuit boards. *IEEE Trans Electron Devices*, 63: 4893–4898.

https://doi.org/10.1109/TED.2016.2619983

160. Géczy A, Nagy D, Hajdu I, *et al.*, 2015, Investigating Mechanical Performance of PLA and CA Biodegradable Printed Circuit Boards, *2015 IEEE 21st International Symposium for Design and Technology in Electronic Packaging* (*SIITME*), 2015 22-25 Oct. 201545-49.

161. Bharath KN, Madhu P, Gowda TGY, *et al.*, 2020, A novel approach for development of printed circuit board from biofiber based composites. *Polym Compos*, 41: 4550–4558.

https://doi.org/10.1002/pc.25732

162. Abdolmaleki H, Kidmose P, Agarwala S, 2021, Droplet-based techniques for printing of functional inks for flexible physical sensors. *Adv Mater*, 33: 2006792.

https://doi.org/10.1002/adma.202006792

163. Vaezi M, Seitz H, Yang S, 2013, A review on 3D micro-additive manufacturing technologies. *Int J Adv Manuf Technol*, 67: 1721–1754.

https://doi.org/10.1007/s00170-012-4605-2

164. Saengchairat N, Tran T, Chua CK, 2017, A review: Additive manufacturing for active electronic components. *Virtual Phys Prototyp*, 12: 31–46.

https://doi.org/10.1080/17452759.2016.1253181

165. Teng L, Ye S, Handschuh-Wang S, *et al.*, 2019, Liquid metal-based transient circuits for flexible and recyclable electronics. *Adv Funct Mater*, 29: 1808739.

https://doi.org/10.1002/adfm.201808739

166. Tavakoli M, Lopes PA, Hajalilou A, *et al.*, 2022, 3R Electronics: Scalable fabrication of resilient, repairable, and recyclable soft-matter electronics. *Adv Mater*, 34: 2203266.

https://doi.org/10.1002/adma.202203266

167. Kwon J, DelRe C, Kang P, *et al.*, 2022, Conductive ink with circular life cycle for printed electronics. *Adv Mater*, 34: 2202177.

https://doi.org/10.1002/adma.202202177

Materials Science in Additive Manufacturing

ORIGINAL RESEARCH ARTICLE

Preparation of polyamide 6 and its titanium dioxide photocatalytic composite powders for laser powder bed fusion

Peng Chen[1], Zhaoqing Li[1], Sheng Liu[1], Jin Su[1], Haoze Wang[1], Lei Yang[2], Chunze Yan[1]*, Yusheng Shi[1]

[1]State Key Laboratory of Materials Processing and Die and Mould Technology, School of Materials Science and Engineering, Huazhong University of Science and Technology, Wuhan, China

[2]School of Logistics Engineering, Wuhan University of Technology, Wuhan, China

Abstract

Laser powder bed fusion (LPBF) additive manufacturing is an effective method to prepare three-dimensional ordered network titanium dioxide (TiO_2) photocatalytic materials, therefore enhancing the absorption intensity of incident light and improving the photocatalytic efficiency. However, TiO_2 is difficult to be directly sintered by LPBF due to the high melting point and brittleness. In this study, we prepared a polyamide 6 (PA6)-coated TiO_2 photocatalytic composite powder for LPBF based on the dissolution precipitation polymer coating (DPPC) method and evaluated its LPBF processability. In the precipitation process of PA6, there was a significant crystallization exotherm with temperature recovery. Effective temperature control of this precipitation process had a significant effect on the morphology and particle size distribution of the precipitated powder. The increase of the dissolved concentration of PA6 to 150 g/L produced an obvious temperature gradient of the reactor, resulting in a wide particle size distribution and a powder with a characteristic porous surface. The prepared PA6/TiO_2 composite powder presents a near-spherical porous-surfaced morphology, a high specific surface area of 240.5 m^2/kg, an appropriate Dv(50) of 48.8 μm, and a wide sintering window of 26.6℃, indicating a good LPBF processability and potential of the photocatalytic application.

Keywords: Additive manufacturing; Laser powder bed fusion; Photocatalytic material; Polyamide 6; Titanium dioxide

***Corresponding author:**
Chunze Yan
(c_yan@hust.edu.cn)

Citation: Chen P, Li Z, Liu S, *et al.*, 2022, Preparation of polyamide 6 and its titanium dioxide photocatalytic composite powders for laser powder bed fusion. *Mater Sci Add Manuf.* 1(3): 14.
https://doi.org/10.18063/msam.v1i3.14

Received: July 6, 2022

Accepted: August 9, 2022

Published Online: August 24, 2022

Copyright: © 2022 Author(s). This is an Open Access article distributed under the terms of the Creative Commons Attribution License, permitting distribution, and reproduction in any medium, provided the original work is properly cited.

1. Introduction

Titanium dioxide (TiO_2) photocatalytic materials have the advantages of stable chemical properties, good photoelectric characteristics, high catalytic activity, and good accessibility[1,2]. These advantages promote their widespread use in the photocatalytic degradation of environmental pollutants, self-cleaning, solar cells, and photolysis of water for hydrogen production, thus facilitating their broad applications in energy, environmental protection, and medical health fields[3-6]. However, TiO_2 has the problems of the low utilization rate of sunlight and low catalytic efficiency. The electrons in excited state and holes can be easily combined, resulting in low photocatalytic reaction efficiency

of most photocarriers. This greatly limits the practical application range of TiO_2 in research and production[5].

From the perspective of material modification, different methods have been studied to improve the photocatalytic performance of TiO_2, such as semiconductor compounding, dye sensitization, noble metal deposition, and carbon (C) compound modification[7-10]. Among these methods, the research on C-modified TiO_2 is particularly attractive. C-TiO_2 composite can increase the specific surface area of the material, which is conducive to the adsorption of reactive species and the occurrence of catalytic reactions. The composite of C-TiO_2 can also make the photogenerated carrier electrons transfer to C and reduce the recombination of photogenerated electrons and photogenerated hole pairs, thereby improving the catalytic efficiency.

From the perspective of structural design, the researchers proposed to prepare a porous TiO_2 photocatalytic material to provide a three-dimensional (3D) network structure with a large specific surface area, which is beneficial to improve the photocatalytic efficiency and also provides a way for the rapid transfer of photogenerated electrons and holes to reduce their recombination probability[11]. Furthermore, the 3D porous structure is beneficial to generate light scattering channels and enhance the absorption of incident light. At present, the preparation of 3D TiO_2 structure mainly adopts ionic liquid, nickel foam, and template methods[12-14]. The prepared 3D porous photocatalytic materials usually have disordered structures, unavoidable structural defects, and poor experimental repeatability, which are the main limitations restricting their applications[15].

Laser powder bed fusion (LPBF) additive manufacturing is an effective technique for fabricating 3D ordered porous photocatalytic materials[6,16-19], which provides a new idea for solving the problems existing in traditional TiO_2 photocatalytic materials. LPBF also provides an effective technical means for the preparation of ordered porous structures with controllable and repeatable photocatalytic properties[20-22]. Although additive manufacturing has significant advantages in the fabrication of complex ordered structures, its application in the field of photocatalysis is very limited. In this paper, a new polyamide 6 (PA6)-coated TiO_2 composite porous material is prepared for LPBF using the dissolution precipitation polymer coating (DPPC) method. As a polymer material, PA6 provides a carbon source for the carbonization preparation of C-TiO_2 porous photocatalytic material. Carbon-complexed porous TiO_2 can increase the efficiency of photogenerated carrier separation and thus improve the photocatalytic efficiency. However, the DPPC method for PA6 and its TiO_2 composite powders has not been studied in-depth. How to regulate the DPPC process parameters, control the porous morphology and size distribution of precipitated powders, and prepare PA6/TiO_2 composite porous powders suitable for LPBF warrants some in-depth investigations.

2. Experimental section

2.1. Materials preparation

Commercial PA6 granules with the trade name Zytel 7331J were obtained from Dupont, USA. P25 type TiO_2 was a highly dispersed gas phase nanoparticle produced by Degussa Company in Germany. The reaction kettle with the capacity of 10 L was used for DPPC powder preparation (Figure 1A), which mainly includes the reaction unit and its temperature control unit. The schematic of the DPPC method is shown in Figure 1B. First, the reaction kettle was heated to 150°C for 2 h to ensure that the PA6 granules were completely dissolved in a high-temperature and high-pressure alcohol solvent. Afterward, the solution was cooled, and the cooling conditions were controlled so that the PA6 macromolecules were uniformly precipitated to realize the nucleation and the coating of TiO_2. The stirring speed was 300 rpm. Finally, the reactor was cooled to room temperature. After discharge, vacuum filtration, drying, and ball milling, the powder materials can be obtained.

2.2. Characterization

The powder morphology and element mapping were carried out by environmental scanning electron microscope (ESEM, FEI Instrument, Netherlands), electron probe microanalyzer 8050 g, SHIMADZU, Japan, and WDS. The specimens were vacuum-coated with platinum for 300 s to avoid charging. The morphology and crystalline structure of nano-TiO_2 were analyzed by field emission transmission electron microscope (TEM, Talos F200X, FEI Instrument, Netherlands) using high resolution TEM (HRTEM) and selected area electron diffraction modes. The particle size distributions of PA6 and composites powers were tested on Mastersizer 3000 (British Malvern). The angle of repose was tested according to the standard ASTM C 1444-00. Four groups of experiments were performed for each kind of powder, and the diameter of each group was recorded 4 times and the mean value was taken. The AOR was calculated using the following equation:

$$\varphi = \arctan 2h/D_a \quad (1)$$

Where ϕ represents AOR, h is the vertical distance between the top height formed by powder accumulation and the bottom end of the funnel (38.1 mm in this experiment), and D_a is the average value of powder packing diameter obtained after four groups multiplied by 4 measurements of each powder. The measurement of powder bulk density

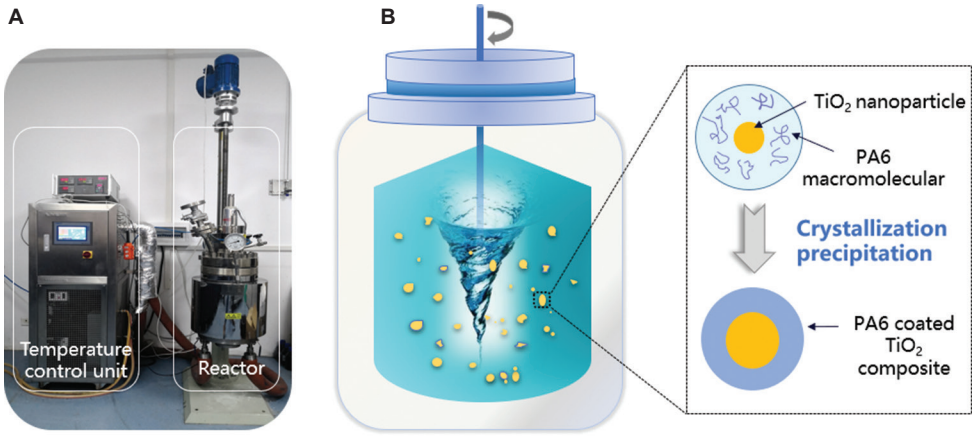

Figure 1. (A) Reaction kettle system. (B) Schematic diagram of DPPC method for the preparation of PA6/TiO_2 composite powders.

was carried out according to the standard ASTM D7481-18. A metal measuring cylinder was placed under the funnel to receive powder quantitatively. The volume of the measuring cylinder was 100 mL. Thermal experiments were performed by Diamond differential scanning calorimetry (DSC, PerkinElmer Instruments, USA) to analyze the melting/crystallization properties of composite powders. The DSC testing was carried out under a nitrogen atmosphere at a heating and cooling rate of 10°C/min. The variation of the crystalline structure was tested on an X'pert3 powder X-ray diffractometer (PANalytical B.V., Netherlands) using Cu Kα radiation at a scan speed of 3°/min.

3. Results and discussion

3.1. Control of precipitation cooling process

First, the precipitation process of PA6 was studied. The precipitation cooling process had an important effect on the morphology and particle size distribution of powders. Figure 2 shows the morphology difference between powder precipitated by rapid cooling at 120°C/h and natural slow cooling at 20°C/h. The powders precipitated by rapid cooling were mainly solid particles, but many of them were featured by incompletely grown sheets. By contrast, the slow-cooling particles stuck with each other. The porous structure of the particle surface is beneficial to the improvement of light absorption efficiency[23,24]. The cooling of the reaction kettle directly determines the particle morphology, size, and surface quality. In the whole cooling process, the control of the precipitation stage plays a key role in the powder properties. Therefore, the whole cooling process was monitored, and the precipitation temperature holding method was adopted to analyze the variation of powder properties.

Figure 3 shows the cooling curve when the reaction kettle was kept at 125°C immediately after precipitation.

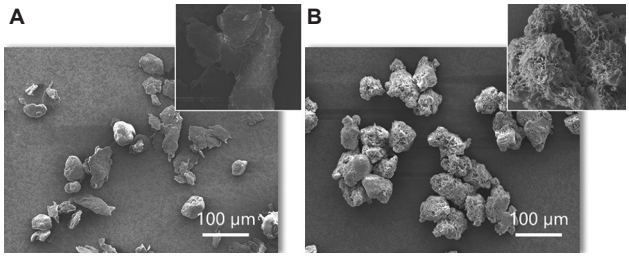

Figure 2. Morphological characteristics of PA6 powders precipitated by (A) rapid cooling at 120°C/h and (B) natural cooling at 20°C/h. The dissolved concentration of PA6 is 50 g/L.

It is obvious that the temperature recovery of PA6 solution occurred in the cooling process, and the dynamic temperature fluctuation occurred in the temperature holding process. This is mainly due to the crystallization exotherm generated during the precipitation of PA6, which increases the temperature of the system. Therefore, the crystallization precipitation temperature of PA6 can be determined according to the transition of the temperature curve. Figure 3 shows that the starting temperature of crystallization precipitation was 124°C. The cooling rate before precipitation was 24.4°C/h, while the cooling rate after precipitation significantly decreased to 16.8°C/h. The exothermic enthalpy during crystallization precipitation increased the temperature of the whole system by 1.8°C, indicating the large exothermic heat from crystallization. Meanwhile, the final steady-state temperature was 0.2°C higher than the equilibrium temperature of 125°C due to the existence of crystallization exothermic enthalpy.

The typical morphology and particle size distribution of powders precipitated at 125°C were studied. It is shown in Figure 4A that the morphology of the powder was nearly spherical. Most of the particles were solid structures without obvious pores, indicating the high solid density of powders. The analysis of particle size distribution

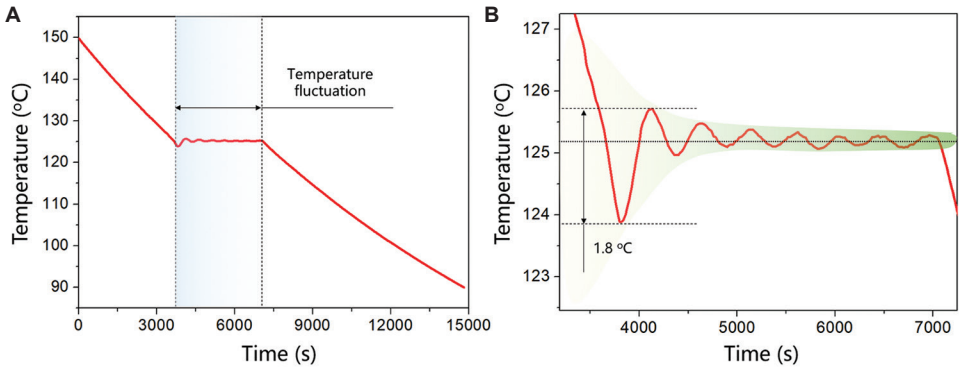

Figure 3. (A) The cooling curve of the reaction kettle held at 125°C for 1 h immediately after precipitation and (B) its characteristic temperature fluctuation. The dissolved concentration of PA6 is 50 g/L.

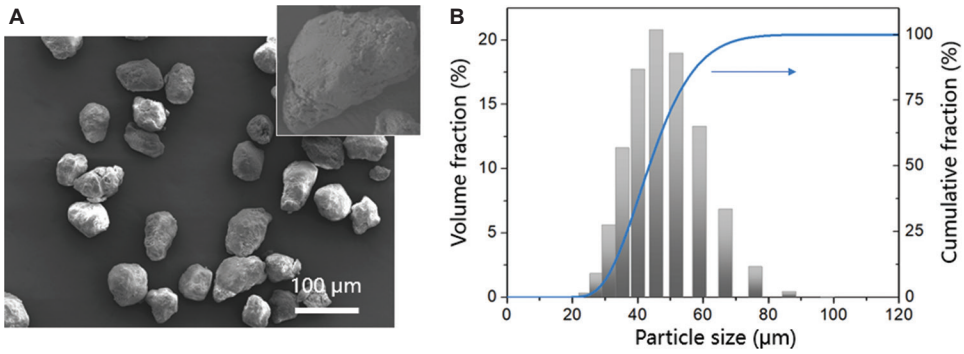

Figure 4. (A) The morphology and (B) particle size distribution of PA6 powders precipitated after holding at 125°C for 1 h. The dissolved concentration of PA6 is 50 g/L.

(Figure 4B) shows that most powders were distributed in the particle size range of 20–90 μm and showed a normal distribution peak at 49.3 μm.

According to the crystallization precipitation temperature and the steady-state temperature, different holding temperatures were taken to study their effects on the powder morphology and particle size distribution (Figures 5 and 6). The changes in powder size at different holding temperatures are shown in Table 1. According to Figure 5, there were distinctly different morphological features of powders precipitated above and below the precipitation temperature. When the holding temperature was low at 120°C, there were many small particles among the powders. The large particles also had an obvious cracking phenomenon, and there were opening pores inside. The particle size showed a bimodal normal distribution, and the small particle powder was aggregated at 10 μm (Figure 6). This is mainly because the particles have already nucleated at 120°C but have not grown up. The temperature holding at this time increased the quantity of small-sized powders. The powders precipitated at 122.5°C showed the morphology transformation of flakes and long strips, and the powder

Table 1. Changes in powder size at different holding temperatures

Parameters	Holding temperature				
	120°C	122.5°C	125°C	127.5°C	130°C
D_v (10)/μm	28.8	29.8	36.2	33.1	25.0
D_v (50)/μm	49.5	45.3	49.3	48.6	40.2
D_v (90)/μm	78.3	68.4	66.7	70.7	63.8
D[3, 2]/μm	41.6	43.1	48.0	46.5	37.6

growth was irregular. Most of the powders showed solid structures, and there was no aggregation of small particles. When the holding temperature was higher than the precipitation temperature at 127.5°C, some powders showed a fish-scale surface, which promotes the formation of internal lapped pores. This is not conducive to powder spreading and density improvement[24]. When the temperature reached 130°C, the excessively high temperature promotes the generation of new secondary nucleated particles with the feature of fish-scale surface. From the perspective of particle size, too high or too low holding temperature can produce small-sized particles.

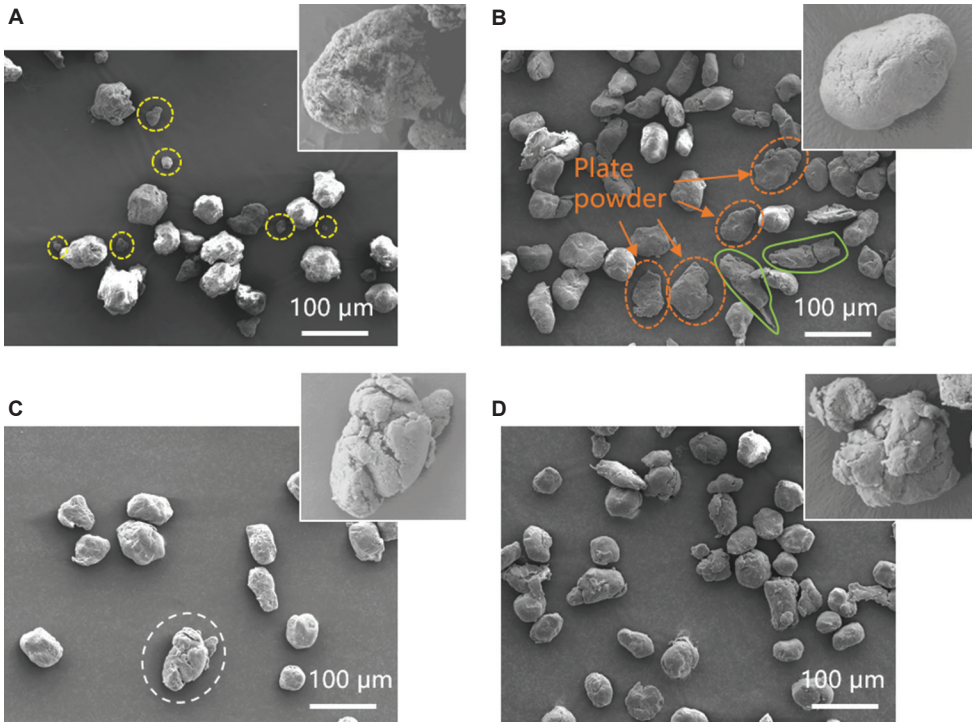

Figure 5. Morphologies of PA6 powders precipitated at different holding temperatures: (A) 120°C, (B) 122.5°C, (C) 127.5°C, and (D) 130°C.

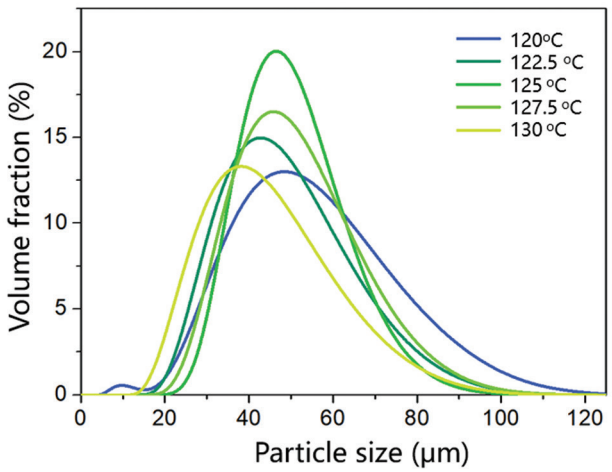

Figure 6. Particle size distributions of PA6 powders precipitated at different holding temperatures.

The small-sized particles from low holding temperatures are caused by an incomplete particle growth process after nucleation, while those from high holding temperatures are caused by secondary nucleation with additional adhesion of surface substances. The heat preservation near the precipitation temperature of 125°C can form particles with a narrow particle size distribution, a uniform particle size, and a smooth surface particle, which is beneficial to the HT-LPBF process.

3.2. Effects of dissolved concentration on powder properties

When the powder was prepared in large quantities, the dissolved concentration of PA6 increased, resulting in a huge difference in particle morphology. Figure 7 shows the changes in morphologies under the concentration conditions of 100 g/L, 150 g/L, and 200 g/L. When the concentration was increased to 100 g/L, the powder surface became rough and uneven, accompanied by the generation of small particles. The powder under the concentration of 150 g/L gradually acquired a porous surface. When the concentration reached 200 g/L, obvious characteristics of multiphase nucleation could be observed. A single particle was formed by the agglomeration of small particles. There was a large number of network structures between the particles, indicating that the particles have already adhered to each other before they grew up.

From a comprehensive analysis, the increase in dissolved concentration leads to the emergence of contradictory phenomena. On the one hand, porous-surfaced powders and rod-like powders were produced. The rod-like powders and porous-surfaced powders appeared only after slow cooling and long-term heat preservation, indicating that the increase in concentration has the same effect as the long-term heat preservation. On the other hand, the agglomeration and inter-bonding of small particles occurred, which are similar to the small particles

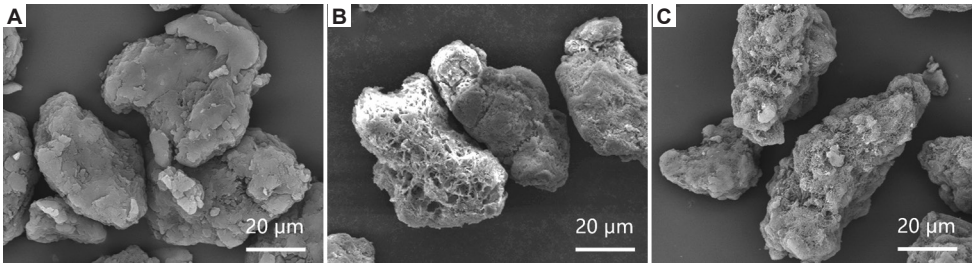

Figure 7. Morphologic difference of powders prepared with different PA6 concentrations: (A) 100 g/L, (B) 150 g/L, and (C) 200 g/L.

produced from low-temperature partial nucleation and high-temperature secondary nucleation. These two aspects indicate that the increase in concentration leads to obvious low-temperature and high-temperature regions, corresponding to the temperature gradient from the kettle wall to the inside of the solution. Therefore, an increase in concentration is not advantageous for uniform precipitation of powders, because the improvement of concentration leads to an increase in the number of nucleation per unit volume and a decrease in the heat transfer rate from the reactor wall to the interior of the solution.

Even so, increasing the concentration would widen the particle size distribution, making it more suitable for increasing the packing density of the LPBF powder bed. The porous-surfaced powders were also favorable for improving photocatalytic performance because a large specific surface area could enhance the absorption of incident light. Based on the concentration of 150 g/L and the condition of 125°C temperature holding for 1 h, the preparation of PA6/TiO_2 composite powders was carried out.

3.3. Evaluation of LPBF processability of composite powder

Based on the precipitation process of PA6 powder, the PA6/TiO_2 composite powders are prepared. As a polymer material, PA6 provides a carbon source for the carbonization preparation of C-TiO_2 photocatalytic material. Carbon-complexed TiO_2 can increase the efficiency of photogenerated carrier separation, and the photogenerated carrier electrons are transferred to C. Therefore, the combination probability of electrons and holes will be greatly reduced, and the photocatalytic efficiency of TiO_2 will be improved. The preparation process of PA6 powder directly determines the network morphology of the precipitated PA6/TiO_2 composite powder, which, further, determines the network morphology of C-TiO_2. In this section, based on the preparation process of pure PA6 powder, porous PA6/TiO_2 composite powders were prepared and the HT-LPBF processability was evaluated.

Figure 8 shows the TEM images and SEAD pattern of the P25-type TiO_2, which is a highly dispersed gas-phase nano-TiO_2. It can be observed from the TEM images that TiO_2 is composed of a large number of nanoscale particles with a size of ~20 nm. HRTEM image shows that the sample is composed of a clear lattice. The interplanar spacing is 3.581 Å, corresponding to the (0 1 0) crystal plane of anatase TiO_2. It can also be observed from the SAED pattern in Figure 8D that there are diffraction rings of 1 0 1, 0 0 4, 2 0 0, and 1 0 5 planes of anatase TiO_2 and those of 2 1 1, 1 1 0, and 1 1 1 planes of rutile phase. Therefore, it can be concluded that the TiO_2 contains a mixed phase of rutile and anatase phases. This can also be proven by XRD analysis (Figure 9). Meanwhile, with the increase of TiO_2 content in the composite powders, the diffraction intensity of TiO_2 was enhanced. The diffraction angle of TiO_2 in the composite powder was shifted to a low 2θ, indicating an increase in the interplanar spacing. This may be attributed to the intercalation of TiO_2 by PA6 molecules under a high-temperature and high-pressure solution environment.

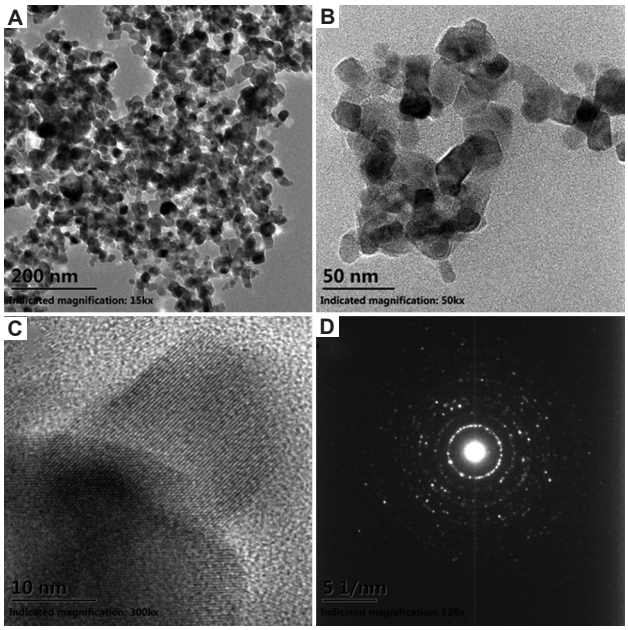

Figure 8. (A and B) TEM images of P25-type TiO_2. (C) HRTEM image. (D) SAED diffraction pattern. SEAD: Selected area electron diffraction.

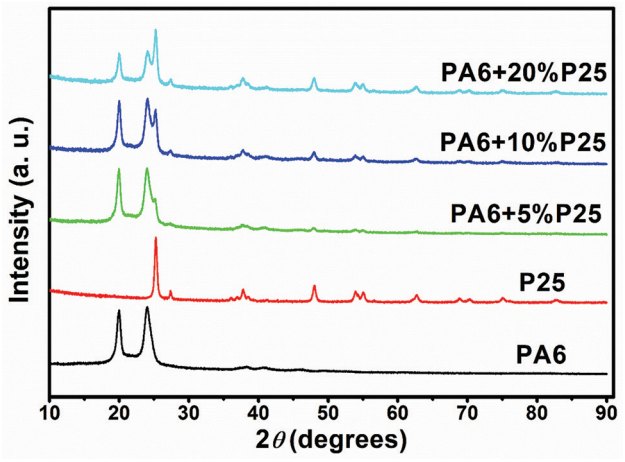

Figure 9. XRD diffraction curves of PA6, P25-type TiO_2, and their composites.

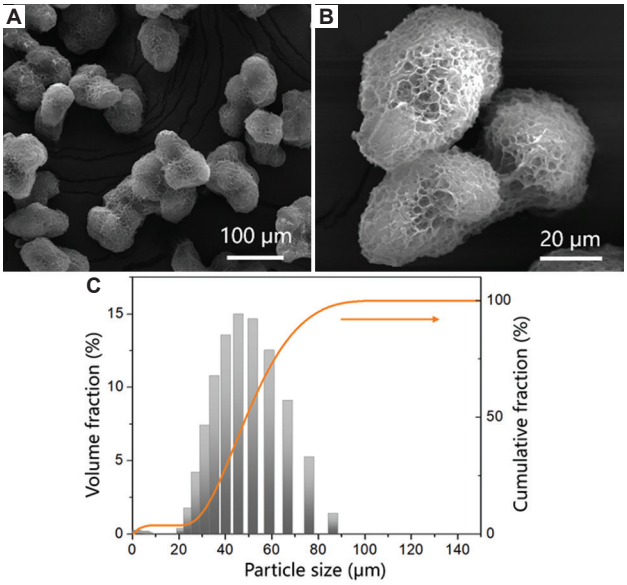

Figure 10. (A and B) Typical microstructure of PA6/TiO_2 composite powder and (C) its particle size distribution.

As shown in Figures 10 and 11, the PA6/TiO_2 composite powders were near-spherical, and there was a weak inter-bonding between the particles. The surface of the powder showed an obvious microporous structure, on which TiO_2 was evenly distributed, and the specific surface area of the powder reached 240.5 m^2/kg. Due to the generation of the porous network morphology, the bulk density of the powder decreased, as shown in Table 2, especially for the composite powders. On the one hand, this may cause large shrinkage during the LPBF process, which is not conducive to the control of part accuracy. On the other hand, this is very beneficial to the uniform absorption of incident light and the improvement of photocatalytic efficiency.

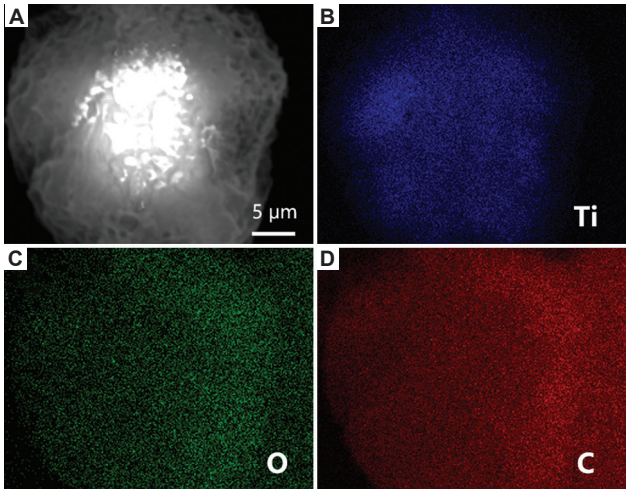

Figure 11. EPMA-WDS element mapping of composite powder shows the distribution of TiO_2 in particle. (A) Microstructure of composite powder, (B) Ti, (C) O, and (D) C element distribution. EPMA-WDS: Electron probe microanalyzer-wavelength dispersive spectrometer.

Laser particle size testing showed that the composite powder exhibited a good normal distribution, although there were some small particles below 10 μm. The Dv(10), Dv(50), and Dv(90) of the composite powder were 31 μm, 48.8 μm, and 72.6 μm, respectively. The AOR values of the prepared PA6 and its TiO_2 composite powders are at or below 30°, indicating good powder flowability and spreading properties compared with LPBF-graded PA12 and PEEK powders[25,26]. Therefore, from the perspective of powder flowability and particle size distribution, the prepared PA6/TiO_2 composite powder is suitable for the LPBF process[27,28].

In addition, from the perspective of rheology properties, the studies demonstrated that PA6 has a similar melt flow index to that of the commercial LPBF-graded PA12 material, indicating suitable melt processing properties of PA6[29,30]. As the DPPC process does not change the essential macromolecular structure of the raw material, it can, therefore, be expected that the rheology properties of the prepared powders are suitable for the LPBF process. From the perspective of thermal properties, the sintering window of the composite powder is broadened from 19.7°C to 26.6°C compared to pure PA6, showing better processability (Figure 12)[31,32]. With the increase of the initial melting and crystallization temperatures of the composite powder, higher powder bed temperature and slower cooling control are required to obtain better mechanical properties and dimensional accuracy.

In general, the PA6/TiO_2 composite powder prepared by the DPPC method has great potential to be used for the LPBF process to fabricate 3D photocatalytic material with a characteristic macro-micro porous structure.

Table 2. Properties of PA6 and its TiO_2 composite powders

Parameter	PA6 (125°C, 1 h, 50 g/L)	PA6 (125°C, 1 h, 150 g/L)	PA6/5% TiO_2	PA6/10% TiO_2	PA6/20% TiO_2
Bulk density (g/cm^3)	0.36±0.001	0.31±0.002	0.28±0.006	0.28±0.004	0.26±0.002
Angle of repose (°)	30.39±0.29	30.75±0.45	29.77±0.68	26.62±0.5	25.96±0.73

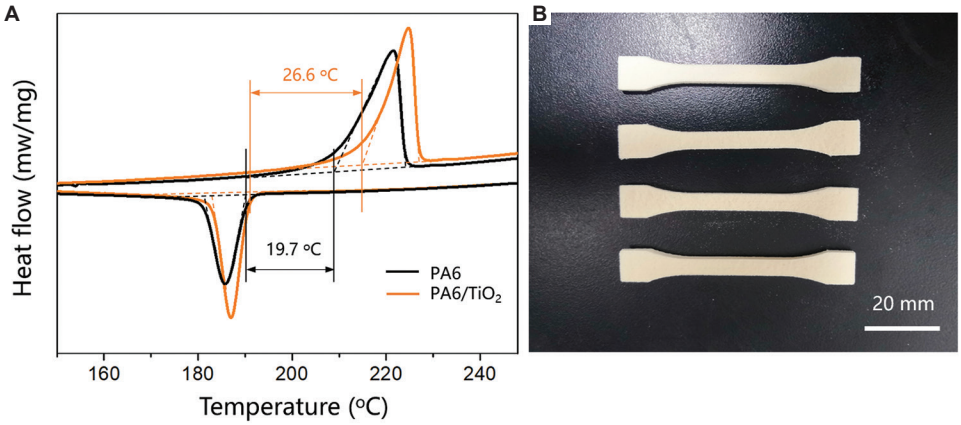

Figure 12. (A) Comparison of DSC curves between PA6 and its TiO_2 composite powders indicating the changes in LPBF processability, and (B) the printed PA6 samples proving the LPBF processability.

4. Conclusion

In this study, the PA6/TiO_2 photocatalytic composite was prepared based on DPPC method, and its LPBF processability was investigated. The main conclusions are as follows:

(i) Holding the crystallization precipitation temperature at 125°C for 1 h, nearly spherical PA6 powders with a particle size of 20–90 μm and a normal distribution peak of 49.3 μm can be obtained.
(ii) Increasing the dissolved concentration of PA6 to 150 g/L will increase the temperature gradient of the reactor, resulting in a porous-surfaced powder and a wide particle size distribution.
(iii) PA6/TiO_2 composite powder has a characteristic spherical porous-surfaced morphology, a high specific surface area of 240.5 m^2/kg, an appropriate Dv(50) of 48.8 μm, and a wide sintering window of 26.6°C, which make it suitable for LPBF process and improvement of photocatalytic efficiency.

This paper describes the preparation of a PA6/TiO_2 powder material for LPBF additive manufacturing of photocatalytic composites and also presents a novel idea for the preparation of macro-micro 3D network TiO_2-based photocatalytic composites.

Acknowledgments

The authors would also like to thank the State Key Laboratory of Materials Processing and Die and Mould Technology and the HUST Testing Center.

Funding

The study was supported by National Natural Science Foundation of China (52105341), China Postdoctoral Science Foundation (2020M682406), Post-Doctoral Innovative Research Post of Hubei Province (Post-doc No. 257963), Fundamental Research Funds for the Central Universities (2019kfyRCPY044 and 2021GCRC002), Program for HUST Academic Frontier Youth Team (2018QYTD04), and Guangdong Provincial Enterprise Key Laboratory for 3D Printing Polymer and Composite Materials (2018B030323001).

Conflict of interest

The authors declare that they have no known competing financial interests or personal relationships that could have appeared to influence the work reported in this paper.

Author contributions

Conceptualization: Peng Chen, Chunze Yan
Data curation: Zhaoqing Li, Haoze Wang
Formal analysis: Zhaoqing Li, Jin Su
Funding acquisition: Chunze Yan, Yusheng Shi
Investigation: Sheng Liu, Haoze Wang
Methodology: Peng Chen
Supervision: Chunze Yan, Yusheng Shi
Validation: Sheng Liu, Jin Su
Writing – original draft: Peng Chen
Writing – review & editing: Peng Chen, Lei Yang, Chunze Yan

References

1. Chen XB, Liu L, Huang FQ, 2015, Black titanium dioxide (Ti_{O2}) nanomaterials. *Chem Soc Rev*, 44: 1861–1885.

   https://doi.org/10.1039/c4cs00330f

2. Hu X, Hu XJ, Peng QQ, *et al.*, 2020, Mechanisms underlying the photocatalytic degradation pathway of ciprofloxacin with heterogeneous TiO_2. *Chem Eng J*, 380: 122366.

   https://doi.org/10.1016/j.cej.2019.122366

3. Wang D, Zhi T, Liu LH, *et al.*, 2022, 3D printing of TiO_2 nano particles containing macrostructures for As(III) removal in water. *Sci Total Environ*, 815: 152754.

   https://doi.org/10.1016/j.scitotenv.2021.152754

4. Kamrannejad MM, Hasanzadeh A, Nosoudi N, *et al.*, 2014, Photocatalytic degradation of polypropylene/TiO_2 nanocomposites. *Mater Res Am J Mater*, 17: 1039–1046.

   https://doi.org/10.1590/1516-1439.267214

5. Li Z, Liu Z, Yang X, *et al.* 2022, Enhanced photocatalysis of black TiO_2/graphene composites synthesized by a facile Sol–Gel method combined with hydrogenation process. *Materials*, 15: 3336.

   https://doi.org/10.3390/ma15093336

6. Shuai C, Shuai C, Feng P, *et al.*, 2018, Antibacterial capability, physicochemical properties, and biocompatibility of $nTiO_{(2)}$ incorporated polymeric scaffolds. *Polymers* (*Basel*), 10: 328.

   https://doi.org/10.3390/polym10030328

7. Kayaci F, Vempati S, Ozgit-Akgun C, *et al.*, 2014, Selective isolation of the electron or hole in photocatalysis: ZnO-TiO_2 and TiO_2-ZnO core-shell structured heterojunction nanofibers via electrospinning and atomic layer deposition. *Nanoscale*, 6: 5735–5745.

   https://doi.org/10.1039/c3nr06665g

8. Xu XY, Wang M, Lin L, *et al.*, 2015, Efficient visible-light photocatalysts from sensitized TiO_2 nanospheres. *Mater Sci Forum*, 814: 31–38.

   https://doi.org/10.4028/www.scientific.net/msf.814.31

9. Shuang S, Lv R, Xie Z, *et al.*, 2016, Surface plasmon enhanced photocatalysis of Au/Pt-decorated TiO_2 nanopillar arrays. *Sci Rep*, 6: 26670.

   https://doi.org/10.1038/srep26670

10. Wang DH, Jia L, Wu XL, *et al.*, 2012, One-step hydrothermal synthesis of N-doped TiO2/C nanocomposites with high visible light photocatalytic activity. *Nanoscale*, 4: 576–584.

    https://doi.org/10.1039/c1nr11353d

11. Wang Q, Zhang LX, Guo YK, *et al.*, 2020, Multifunctional 2D porous g-C3N4 nanosheets hybridized with 3D hierarchical TiO_2 microflowers for selective dye adsorption, antibiotic degradation and CO_2 reduction. *Chem Eng J*, 396: 125347.

    https://doi.org/10.1016/j.cej.2020.125347

12. Carp O, Huisman CL, Reller A, 2004, Photoinduced reactivity of titanium dioxide. *Prog Solid State Chem*, 32: 33–177.

    https://doi.org/10.1016/j.progsolidstchem.2004.08.001

13. Fattakhova-Rohlfing D, Zaleska A, Bein T, 2014, Three-dimensional titanium dioxide nanomaterials. *Chem Rev*, 114: 9487–9558.

    https://doi.org/10.1021/cr500201c

14. Yang L, Yan C, Fan H, *et al.*, 2019, Investigation on the orientation dependence of elastic response in Gyroid cellular structures. *J Mech Behav Biomed Mater*, 90: 73–85.

    https://doi.org/10.1016/j.jmbbm.2018.09.042

15. Yang L, Yan C, Han C, *et al.*, 2018, Mechanical response of a triply periodic minimal surface cellular structures manufactured by selective laser melting. *Int J Mech Sci*, 148: 149–157.

    https://doi.org/10.1016/j.ijmecsci.2018.08.039

16. Skorski MR, Esenther JM, Ahmed Z, *et al.*, 2016, The chemical, mechanical, and physical properties of 3D printed materials composed of TiO_2-ABS nanocomposites. *Sci Technol Adv Mater*, 17: 89–97.

    https://doi.org/10.1080/14686996.2016.1152879

17. Chen P, Su J, Wang H, *et al.*, 2022, Mechanical properties and microstructure characteristics of lattice-surfaced PEEK cage fabricated by high-temperature laser powder bed fusion. *J Mater Sci Technol*, 125: 105–117.

    https://doi.org/10.1016/j.jmst.2022.03.009

18. Chen P, Wang H, Su J, *et al.*, 2022, Recent advances on high-performance polyaryletherketone materials for additive manufacturing. *Adv Mater*, 2200750.

    https://doi.org/10.1002/adma.202200750

19. Yang L, Wu S, Yan C, *et al.*, 2021, Fatigue properties of Ti-6Al-4V Gyroid graded lattice structures fabricated by laser powder bed fusion with lateral loading. *Addit Manuf*, 46: 102214.

    https://doi.org/10.1016/j.addma.2021.102214

20. Wu S, Yang L, Wang C, *et al.*, 2022, Ceramic lattices with a triply periodic minimal surface structure prepared by laser powder bed fusion. *Addit Manuf*, 56: 102910.

    https://doi.org/10.1016/j.addma.2022.102910

21. Hussein A, Hao L, Yan C, *et al.*, 2013, Young, advanced lattice support structures for metal additive manufacturing. *J Mater Process Tech*, 213:1019–1026.

    https://doi.org/10.1016/j.jmatprotec.2013.01.020

22. Yan C, Hao L, Hussein A, *et al.*, 2012, Evaluations of cellular lattice structures manufactured using selective laser melting. *Int J Machine Tools Manuf*, 62: 32–38.

https://doi.org/10.1016/j.ijmachtools.2012.06.002

23. Chen P, Wu H, Zhu W, *et al*., 2018, Investigation into the processability, recyclability and crystalline structure of selective laser sintered polyamide 6 in comparison with polyamide 12. *Polym Test*, 69: 366–374.

    https://doi.org/10.1016/j.polymertesting.2018.05.045

24. Chen B, Berretta S, Davies R, *et al*., 2019, Characterisation of carbon fibre (Cf) Poly Ether Ketone (PEK) composite powders for laser sintering. *Polym Test*, 76: 65–72.

    https://doi.org/10.1016/j.polymertesting.2019.03.011

25. Chen B, Wang Y, Berretta S, *et al*., 2017, Poly aryl ether ketones (PAEKs) and carbon-reinforced PAEK powders for laser sintering. *J Mater Sci*, 52: 6004–6019.

    https://doi.org/10.1007/s10853-017-0840-0

26. Berretta S, Ghita O, Evans KE, 2014, Morphology of polymeric powders in laser sintering (LS): From polyamide to new PEEK powders. *Eur Polym J*, 59: 218–229.

    https://doi.org/10.1016/j.eurpolymj.2014.08.004

27. Chen P, Su J, Wang H, *et al*., 2022, Aging mechanism of polyetheretherketone powder during layer-wise infrared radiation of high-temperature laser powder bed fusion. *Mater Des*, 213: 110348.

    https://doi.org/10.1016/j.matdes.2021.110348

28. Su J, Hua S, Chen A, *et al*., 2021, Three-dimensional printing of gyroid-structured composite bioceramic scaffolds with tuneable degradability. *Mater Sci Eng C*, 133: 112595.

    https://doi.org/10.1016/j.msec.2021.112595

29. Salmoria GV, Leite JL, Vieira LF, *et al*., 2012, Mechanical properties of PA6/PA12 blend specimens prepared by selective laser sintering. *Polym Test*, 31: 411–416.

    https://doi.org/10.1016/j.polymertesting.2011.12.006

30. Salmoria GV, Leite JL, Paggi RA, 2009, The microstructural characterization of PA6/PA12 blend specimens fabricated by selective laser sintering. *Polym Test*, 28: 746–751.

    https://doi.org/10.1016/j.polymertesting.2009.06.010

31. Wang H, Chen P, Wu H, *et al*., 2022, Comparative evaluation of printability and compression properties of poly-ether-ether-ketone triply periodic minimal surface scaffolds fabricated by laser powder bed fusion. *Addit Manuf*, 57: 102961.

    https://doi.org/10.1016/j.addma.2022.102961

32. Guo B, Xu Z, Luo X, *et al*., 2021, A detailed evaluation of surface, thermal, and flammable properties of polyamide 12/glass beads composites fabricated by multi jet fusion. *Virtual Phys Prototy*, 16: S39–S52.

    https://doi.org/10.1080/17452759.2021.1899463

Materials Science in Additive Manufacturing

ORIGINAL RESEARCH ARTICLE

Optimizing of chemical admixtures for 3D printable cementitious materials by central composite design

Mingyang Li[1], Yiwei Weng[2]*, Zhixin Liu[1], Dong Zhang[3], Teck Neng Wong[1]

[1]Singapore Centre for 3D Printing, Nanyang Technological University, Singapore

[2]Department of Building and Real Estate, The Hong Kong Polytechnic University, Hong Kong, China

[3]College of Civil Engineering, Fuzhou University, Fuzhou, China

Abstract

Printability of 3D printable cementitious materials is related to material rheological properties, and is affected and controlled by modern concrete chemical admixtures. In this work, the influence of several chemical admixtures including superplasticizer, retarder, and accelerator on the rheological characteristics of printable materials was investigated using central composite design (CCD). Twenty test points with varying dosages of chemical admixtures were performed to evaluate the primary effects of chemical admixtures and their combined interactive effects on the rheological properties. The results indicate that with the increase of retarder or superplasticizer dosage, all rheological parameters decrease while accelerator possesses an opposite impact. The rheological properties are negatively proportional to the combined interactive effect of retarder and accelerator. The combined interactive effect of retarder and superplasticizer positively affects dynamic yield stress, plastic viscosity, and thixotropy, while it negatively impacts static yield stress. The combined interactive effect of accelerator and retarder positively affects the yield stress, whereas it negatively influences the plastic viscosity and thixotropy. The results indicate that the CCD is an efficient method to find the desirable formulation within a given boundary.

Keywords: 3D concrete printing; Central composites design; Rheological properties; Statistical models

***Corresponding author:**
Yiwei Weng
(yiwei.weng@polyu.edu.hk)

Citation: Li M, Weng Y, Liu Z, *et al.*, 2022, Optimizing of chemical admixtures for 3D printable cementitious materials by central composite design. *Mater Sci Add Manuf,* 1(3): 16.
https://doi.org/10.18063/msam. v1i3.16

Received: July 30, 2022
Accepted: September 4, 2022
Published Online: September 21, 2022

Copyright: © 2022 Author(s). This is an Open Access article distributed under the terms of the Creative Commons Attribution License, permitting distribution, and reproduction in any medium, provided the original work is properly cited.

Publisher's Note: Whioce Publishing remains neutral with regard to jurisdictional claims in published maps and institutional affiliations.

1. Introduction

The 3D concrete printing (3DCP) technique, an extrusion-based additive manufacturing process[1-3], has attracted much attention in recent years due to its advantages, such as automated process, formwork-free construction, and improved productivity[4-6]. These benefits are mainly due to the automated layer-by-layer construction process based on a 3D model. In the printing process, material rheological performance is a critical factor determining the printability of printed structures[7-9].

Printability is characterized by buildability and pumpability, which are related to material rheological properties (static/dynamic yield stress, plastic viscosity, and thixotropy)[10,11]. These parameters are affected by various factors, including material

constituents and chemical admixtures[12-16]. Weng *et al.*[8] explored the impact of material constituents on rheological properties of 3D printable materials and proposed statistical models to predict rheological properties. Zhang *et al.*[17] presented that the buildability could increase by 150% with the addition of a small quantity of nanoclay. Apart from material constituents, chemical admixtures also serve vital roles on rheology of concrete[12,13]. Dressler *et al.*[18] studied the effect of accelerator on the material properties in shotcrete 3D printing. Tao *et al.*[19] investigated the stiffening control of material using an inline mixing process with chemical admixtures. Yu *et al.*[20,21] studied the influence of mortar composition on the aggregate bed process by adjusting the sand/cement ratio and the water/cement ratio in aggregate-bed 3D concrete printing.

Many research works have been conducted to study the impact of chemical admixtures on rheological properties[22-24]. However, there are still certain limitations. First, conclusions from the previous works are mainly qualitative. Few quantitative results have been established to explain the impact of chemical admixtures on the rheological properties. Furthermore, research needs to be carried out to explore the impact of chemical admixtures on thixotropy, which measures the structural rebuilding rate of materials. Therefore, more attention should be paid to explore the impact of chemical admixtures on rheological properties and construct models to predict rheological properties. More specifically, an efficient approach should be adopted for experimental design, and quantitative models should be built empirically through a series of experiments[25].

Design of experiments (DoE) is a class of scientific methodology for experimental design and data analysis to improve research efficiency based on fundamental mathematical statistics[26]. It has been successfully used in various research fields as a powerful approach to exploring the relationship between factors and responses[27-29]. One of the useful DoE methods is called central composite design (CCD), quantifying the impact of variables on responses through constructing statistical models. Using CCD, the experimental process can be simplified, and the experimental runs can be reduced, while the sufficient information can be extracted from the experiment for data analysis. In summary, the CCD method is more efficient than traditional one-factor at one-time experiment design.

In this study, CCD was adopted to efficiently construct statistical models, expressing the rheological characteristics as functions of different factors, that is, various chemical admixtures. The constructed statistical models are not universally applicable[30], while the results indicate that the CCD is efficient to find the desirable formulation within a given boundary.

2. Methodology

2.1. Response surface method and central composite design

As one of the most reliable statistical methodologies in DoE, response surface methodology (RSM) includes optimization procedures for the settings of factorial variables, such that the response reaches a desired maximum or minimum value[26]. The RSM includes various design structures, such as CCD and Box-Behnken[26]. CCD design structure was used in this work as it explores a larger process space and provides a higher prediction quality over the entire space than that of Box-Behnken.

The structure of CCD design includes corner points, axial points, and center points (corresponding to ±1, ±1.68, and 0 as shown in Figure 1). Corner points are the parameters with boundary values. The axial points can make the model in quadratic terms, considering the curvature effect. The experiments of center points were replicated for several times to provide information on process reproducibility.

2.2. Rheology and time-dependent effect

2.2.1. Rheology of cementitious materials

Rheological properties of cementitious materials are described by Bingham plastic model and characterized by the static/dynamic yield stress and plastic viscosity. The correlation between shear stress τ (Pa) and shear rate γ (1/s) in the Bingham model is described in Equation I:

$$\tau = \tau_0 + k\gamma \quad \text{(I)}$$

Where τ_0 is yield stress, which includes static yield stress τ_s (Pa) and dynamic yield stress τ_d (Pa). τ_s and τ_d are the minimum shear stress to initiate and maintain the flow of materials, respectively. Plastic viscosity k (Pa·s) describes the resistance of fluid to flow when it is agitated. All the rheological parameters can be obtained from the

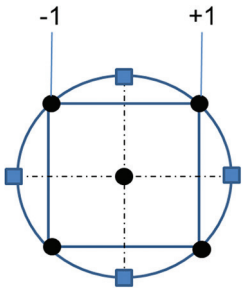

Figure 1. Design structure of CCD.

rheological test[11], in which Bingham model can also be expressed as the following formula (Equation II) for convenience of experiment design and data analysis:

$$T = G + hN \quad \text{(II)}$$

Equation II describes the correlation between the measured torque T (N·m) and rotational speed N (rpm). The parameter G (N·m) is flow resistance, representing the minimum torque required to initiate or maintain the flow of a material. The parameter h (N·m·min) is torque viscosity. Similar to the k in Equation I, the parameter h describes the change of applied torque with altering rotational speed.

Buildability and pumpability can be characterized by a build-up model and a pumping pressure model, respectively. The built-up model can be adopted to predict the printed height of structures with static yield stress of material, and the model is expressed in Equation III[31]:

$$H = \frac{\alpha}{\rho g}\tau_s(t) \quad \text{(III)}$$

Where H (m) and α are the printed height (buildability) and the geometric factor of printed structures, respectively; ρ (kg/m^3) and g (m/s^2) are the density of materials and gravitational constant, respectively. Equation III implies that the printed height is positively proportional to the static yield stress for a given material and structure. pumpability, generally characterized by pumping pressure, is positively related to dynamic viscosity that measures a fluid's resistance to flow when an external force is applied[32].

2.2.2. Time-dependent effect of rheological properties

Rheological properties evolve with time due to hydration process. A theoretical model proposed by Roussel *et al.*[33] correlates yield stress with resting time. The model is expressed in Equation IV:

$$\tau_s(t) = \tau_s(0) + A_{thix}t \quad \text{(IV)}$$

Where t (s) is time at rest; A_{thix} (Pa/s) is thixotropy parameter, a constant value for a given material; $\tau_s(0)$ is the static yield stress as a function of resting time $t = 0$. A high A_{thix} is required for the 3D printable cementitious material in printing process to accelerate the increase of static yield stress to make certain that materials possess appropriate buildability.

The time effect on the evolution of dynamic viscosity is expressed in Equation V:

$$\mu(t) = \mu_0 + (1000 - \mu_0)(t/t_v)^n \quad \text{(V)}$$

Where t (s) is time at rest; t_v is 1000 Pa·s. μ_0 is initial dynamic viscosity. Generally, dynamic viscosity changes slightly in 30 min after mixing[34].

3. Materials, mixture design, and properties characterization

3.1. Materials and mixture design

Material mixture in this study consists of ordinary Portland cement (OPC, ASTM type I, Grade 42.5), silica fume (SF, undensified, Grade 940, Elkem company), fine sand, fly ash (FA, Class F), water, superplasticizer (MasterPozzolith-R168, BASF Pte. Ltd.), accelerator (MasterRoc SA160, BASF Pte. Ltd.), and retarder (MasterReobuild1000, BASF Pte. Ltd.). Particle size distribution is illustrated in Figure 2, and the chemical composition of all the raw ingredients used is shown in Table 1. The mixtures used in this study follow the same mixture proportion, as shown in Table 2.

The dosage of chemical admixtures was designed by the CCD, and the coded and actual values used in the experiment are presented in Table 3. The relationship between coded and actual values is expressed in Equation VI[8].

$$\text{Coded value} = \left(\text{Actual value} - \text{Factor mean}\right) / \left(\text{Range of factorial value} / 2\right) \quad \text{(VI)}$$

3.2. Mixing process and properties characterization

A Hobart mixer X200L was used for mixing. The rheological properties of cement slurries are influenced by several factors, such as speed, time, and temperature. Thus, mixing procedures in this study were fixed to minimize the difference among batches. First, the powders of all solid ingredients were dry mixed for 1 min in stir speed (33 rpm). Water, superplasticizer, and retarder were then added, and the mixing process continued for 1 min in stir speed (33 rpm) followed by 1 min in speed I (61 rpm);

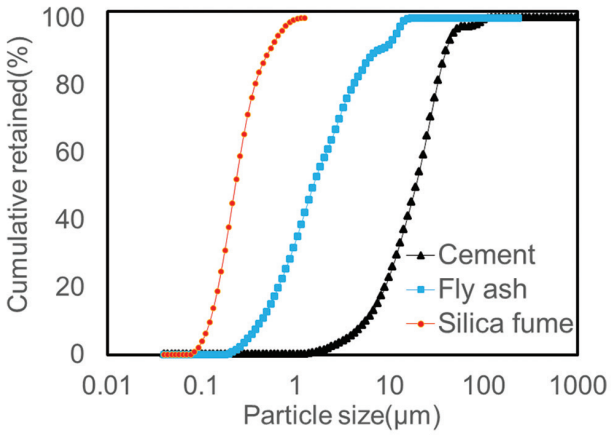

Figure 2. Particle size distribution of ordinary Portland cement, fly ash, and silica fume.

the accelerator was then added, and the mixing process continued for 1 min in speed II (113 rpm).

Rheological properties of mixed materials, including static/dynamic yield stress and plastic viscosity, were characterized via Viskomat XL. The six-blade vane probe and cage are used for rheological test to avoid slippage of cement paste. Both the diameter and the height of this vane probe are 69 mm, and the gap between probe and cage, and the bottoms of probe and barrel are both 40 mm. During the rheological test, the speed of rheometer increased linearly from 0 rpm to 60 rpm in 5 min. Afterward, the speed decreased linearly to 0 rpm in another 5 min as shown in Figure 3. The typical test result of rheological properties is plotted in Figure 4. Then the static/dynamic yield stress and plastic viscosity can be computed by Equation VII [11]:

$$\Gamma = \frac{4\pi R_1^2 R_2^2 lk}{R_2^2 - R_1^2}\omega_2 - \frac{4\pi R_1^2 R_2^2 l\tau_d}{R_2^2 - R_1^2}\ln\frac{R_1}{R_2} \qquad \text{(VII)}$$

Where Γ (N·m) is the torque, ω_2 (rad/s) is the rotational speed of outer barrel, l (m) and R_1 (m) are the length and radius of the probe, respectively, and R_2 (m) is the radius of the outer barrel. Thixotropy value is measured by the area of hysteresis loop[8,15,35] in Figure 4.

Table 1. Chemical composition of FA and OPC

Formula	Concentration/%	
	FA	OPC
SiO_2	58.59	24.27
Al_2O_3	30.44	4.56
Fe_2O_3	4.66	3.95
TiO_2	2.02	0.55
K_2O	1.51	0.61
CaO	1.21	62.2
MgO	0.776	3.34
P_2O_5	0.531	0.15
Na_2O	-	0.21
SO_3	0.0914	-
ZrO_2	0.04	-
MnO	0.0351	-
Cr_2O_3	0.027	-
CuO	0.0254	-
ZnO	0.0229	-

OPC: Ordinary Portland cement, FA: Fly ash

3.3. Printability test

Finally, a printing test was conducted to investigate the printability of designed mixture. As shown in Figure 5, a gantry printer with a 1.2 m × 1.2 m × 1.0 m (L × W × H) printing volume was used to print specimens. The dimension of nozzle opening was 30 mm × 10 mm. Nozzle travel speed and pumping speed are 2,000 mm/min and 650 rpm, respectively. The standoff distance was 30 mm. 3D model used in the printing test is shown in Figure 6.

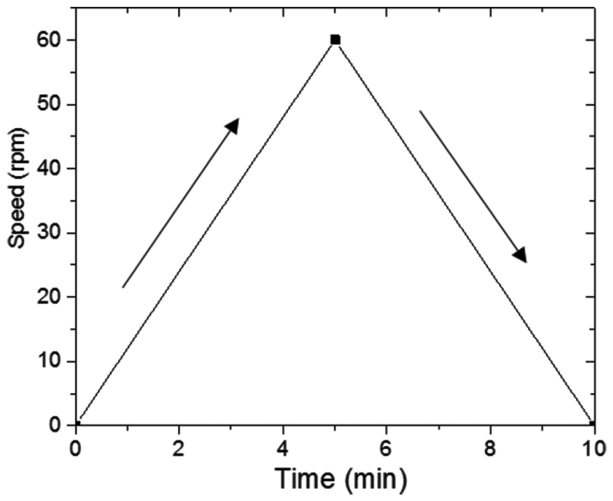

Figure 3. Rheological testing programs.

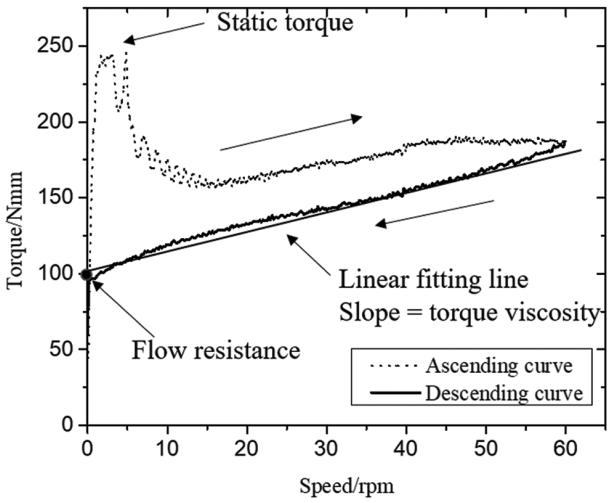

Figure 4. The typical test results of rheology.

Table 2. Mixture proportion

OPC (g)	Sand (g)	W (g)	FA (g)	SF (g)	Retarder (g)	Accelerator (g)	Superplasticizer (g)
1356	1729	1024	2034	68	4.47–15.9	4.47–15.9	2.24–7.93

Table 3. Coded values via CCD

Test run	Retarder		Accelerator		Superplasticizer	
	Coded value	Actual value (g)	Coded value (g)	Actual value (g)	Coded value	Actual value (g)
1	−1	6.78	−1	6.78	−1	3.39
2	1	13.6	−1	6.78	−1	3.39
3	−1	6.78	1	13.6	−1	3.39
4	1	13.6	1	13.6	−1	3.39
5	−1	6.78	−1	6.78	1	6.78
6	1	13.6	−1	6.78	1	6.78
7	−1	6.78	1	13.6	1	6.78
8	1	13.6	1	13.6	1	6.78
9	−1.68	4.47	0	10.2	0	5.08
10	1.68	15.9	0	10.2	0	5.08
11	0	10.2	−1.68	4.47	0	5.08
12	0	10.2	1.68	15.9	0	5.08
13	0	10.2	0	10.2	−1.68	2.24
14	0	10.2	0	10.2	1.68	7.93
15	0	10.2	0	10.2	0	5.08
16	0	10.2	0	10.2	0	5.08
17	0	10.2	0	10.2	0	5.08
18	0	10.2	0	10.2	0	5.08
19	0	10.2	0	10.2	0	5.08
20	0	10.2	0	10.2	0	5.08

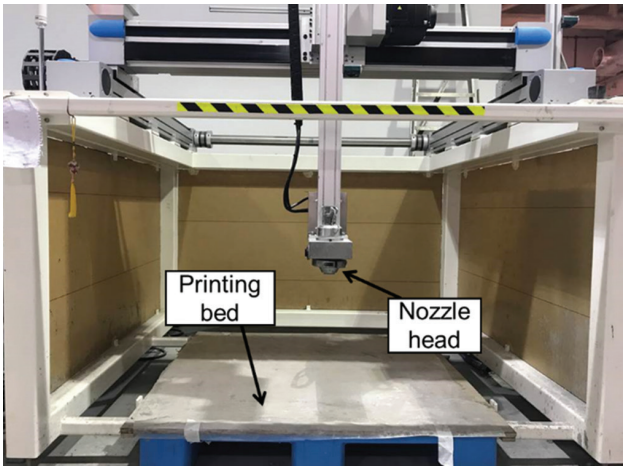

Figure 5. Gantry printer.

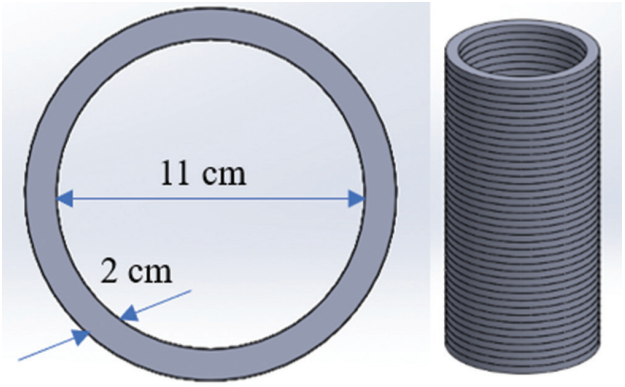

Figure 6. CAD model for printability test.

4. Results and discussion

4.1. ANOVA analysis

The rheological testing results are presented in Table 4, including static torque, flow resistance, and torque viscosity. These results are converted into static/dynamic yield stress and plastic viscosity.

The ANOVA results, which are shown in Table 5, indicate the significance of the influence of individual and interaction (second-order effect) of factors on the rheological properties. A, B, and C stand for the coded factors of superplasticizer, retarder, and accelerator, respectively. AB, BC, and AC represent the interactive effect of superplasticizer and retarder, retarder and accelerator, and superplasticizer and accelerator, respectively.

Materials Science in Additive Manufacturing

Table 4. Experimental results of CCD

Test run	Static torque (N·mm)	Flow resistance (N·mm)	Torque viscosity (N·mm/rpm)	Static yield stress (Pa)	Dynamic yield stress (Pa)	Plastic viscosity (Pa·s)	Thixo-tropy (Pa/s)
1	843.1	194.7	2.58	833.2	192.4	18.84	13243
2	976.3	178.3	2.00	964.8	176.2	14.58	6263
3	1170	233.0	3.53	1156	230.3	25.79	17081
4	937.3	165.4	2.38	926.3	163.5	17.37	8667
5	673.6	164.5	2.90	665.7	162.6	21.19	9898
6	595.6	150.4	2.70	588.6	148.7	19.73	7410
7	1057	213.9	2.08	1045	211.4	15.21	12373
8	639.7	155.3	2.41	632.2	153.5	17.62	9222
9	1082	215.2	3.06	1070	212.7	22.35	15099
10	846.3	155.9	2.17	836.3	154.0	15.88	6893
11	762.8	187.3	1.89	753.9	185.1	13.84	13124
12	996.6	210.9	2.89	984.9	208.4	21.09	17889
13	1099	182.4	2.64	1086	180.2	19.28	11351
14	639.0	149.2	2.46	631.5	147.4	17.97	9233
15	837.9	169.0	2.82	828.1	167.0	20.60	17446
16	834.6	167.2	3.01	824.8	165.3	21.99	17256
17	856.3	166.5	2.64	846.2	164.6	19.29	17126
18	805.6	171.2	2.80	796.1	169.1	20.46	17296
19	825.6	168.5	3.02	815.9	166.5	22.06	18224
20	864.5	169.8	2.90	854.3	167.8	21.19	16585

CCD: Central composite design

Table 5. The ANOVA results of DoE

Responses	Static yield stress (Pa)		Dynamic yield stress (Pa)		Plastic viscosity (Pa·s)		Thixotropy (Pa/s)	
	P-value	*F* value	*P*-value	*F* value	*P*-value	*F* value	*P*-value	*F* value
Model	$<10^{-4}$	46.15	$<10^{-4}$	140.6	0.0062	5.64	$<10^{-4}$	43.18
A	$<10^{-4}$	61.91	$<10^{-4}$	577.8	0.0043	13.46	$<10^{-4}$	106.58
B	$<10^{-4}$	77.18	$<10^{-4}$	125.1	0.0482	5.06	0.0003	30.20
C	$<10^{-4}$	188.8	$<10^{-4}$	179.8	0.4329	0.6678	0.0148	8.630
AB	$<10^{-4}$	53.34	$<10^{-4}$	137.4	0.9525	0.0037	0.4358	0.6589
AC	0.0022	16.77	0.1961	1.920	0.0162	8.34	0.0036	14.26
BC	0.1792	2.090	0.0054	12.48	0.0036	14.29	0.4663	0.5737

In ANOVA, P-value and F-value serve as critical parameters to evaluate the significance of the proposed model and individual parameters. The P-value is the probability of achieving the F-value. A small P-value reveals that the effects of the parameters are statistically significant, while the high F-value indicates that the variation reported by the model is significantly larger than that inherent in the process [27]. For example, the factor AC has a F-value of 16.77 and a P-value of 0.0022 associated with static yield stress, and the results indicate that there was only a 0.22% possibility that the F-value of 16.77 occurs because of noise. As can be seen from ANOVA results, except for some cases in AB, AC, and BC, the P-value is generally smaller than 0.05, which implies that the model used for predicting the response is statistically significant.

Figure 7 shows the normability tests. As can be seen from Figure 7, all the points are scattering around a straight line. The result indicates that residuals followed a normal distribution, and static/dynamic yield stress, plastic

viscosity, and thixotropy cannot be further improved by adopting other curve fitting methods.

To exclude the run order effects from various statistical rheological models, the relation between the residual and run order should be confirmed[27]. Figure 8 shows that the points scatter randomly (no grouping) with the run order, which indicates that run order has no significant impact on the responses.

4.2. Prediction models

The coefficients of prediction models are presented in Table 6. A positive value indicates a positive effect on the response, while a negative value implies a negative effect on the response. The magnitude of the absolute value represents how significant the factor is and can be used to rank the importance of each factor. Results in Table 6 suggest that with an increase in the dosage of retarder and superplasticizer, all these rheological parameters decrease while accelerator possesses the opposite influence on the rheological properties. The interaction of retarder and accelerator (AB) has a negative influence on all the rheological properties. The interaction of retarder and superplasticizer (AC) possesses a positive influence on the dynamic yield stress, plastic viscosity, and thixotropy, while it has a negative influence on the static yield stress. The interaction of accelerator and superplasticizer (BC) has a positive influence on the yield stress, whereas it possesses a negative influence on the plastic viscosity and thixotropy.

The derived models for static/dynamic yield stress, plastic viscosity, and thixotropy with respect to the three main factors and their second-order effects can be written as follows:

$$\text{Static yield stress} = 829.1 - 71.89A + 80.27B - 125.5C - 87.19AB - 48.89AC + 17.24BC \quad \text{(VIII)}$$

$$\text{Dynamic yield stress} = 166.8 - 18.56A + 8.640B - 10.35C - 11.83AB + 1.400AC + 3.560BC \quad \text{(IX)}$$

$$\text{Plastic viscosity} = 20.91 - 1.650A + 1.010B - 0.3685C - 0.0360AB + 1.700AC - 2.230BC \quad \text{(X)}$$

$$\text{Thixotropy} = 17369 - 2550A + 1357B - 725.9C - 262.1AB + 1219AC - 244.5BC \quad \text{(XI)}$$

The statistical analysis, as shown in Table 6, was also conducted to estimate the statistical accuracy of established models. High R-squared value (larger than 0.8) and high adequate precision (larger than 4) indicate

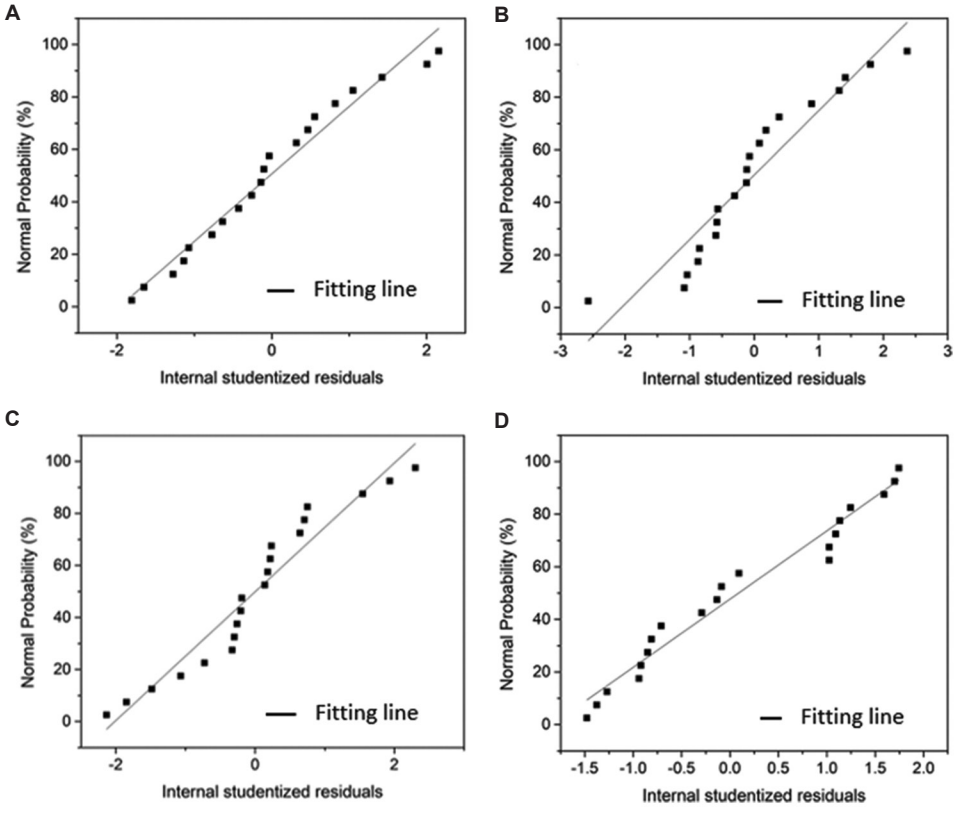

Figure 7. Normal probability plots of residuals for different responses: (A) Static yield stress; (B) dynamic yield stress; (C) plastic viscosity; and (D) thixotropy.

Materials Science in Additive Manufacturing

Table 6. Coefficients of derived models

Factors	Coefficient of models			
	Static yield stress (Pa)	Dynamic yield stress (Pa)	Plastic viscosity (Pa·s)	Thixotropy (Pa/s)
Interception	829.1	166.82	20.91	17369
A	−71.89	−18.56	−1.65	−2550
B	80.27	8.64	1.01	1357
C	−125.5	−10.35	−0.3685	−725.9
AB	−87.19	−11.83	−0.0360	−262.1
AC	−48.89	1.40	1.70	1219
BC	17.24	3.56	−2.23	−244.5
R2	0.9765	0.9922	0.8354	0.9749
Adequate precision	23.26	41.08	11.20	17.90

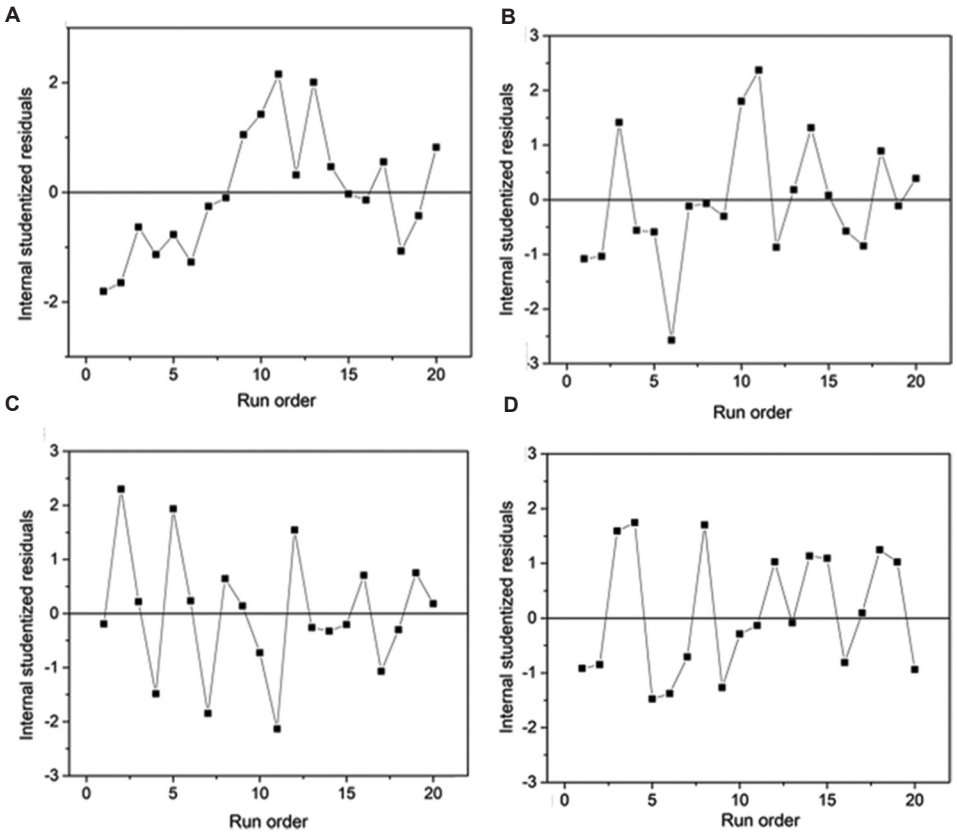

Figure 8. The relationship between residuals and run orders: (A) Static yield stress; (B) dynamic yield stress; (C) plastic viscosity; and (D) thixotropy.

that the obtained model is statistically significant. The adequate precision is a signal-to-noise ratio. It compares the range of the predicted values at the design points to the average prediction error[26]. Ratios greater than 4 indicate adequate model discrimination. Figure 9 shows the predicted values (calculated from the model) versus the actual values (obtained from experiments). It is clear that the models were successful in capturing the correlation between the dosages of chemical admixtures and material rheological properties with high R-squared values in Table 6.

Figure 10 shows the 3D response surface, in which the coded value of superplasticizer is set as 0. As can be seen from Figure 10, the dosages required for accelerators or retarders to achieve different rheological properties can be found from the contour figures, for example, maximum static yield stress or lowest plastic viscosity.

 https://doi.org/10.18063/msam.v1i3.16

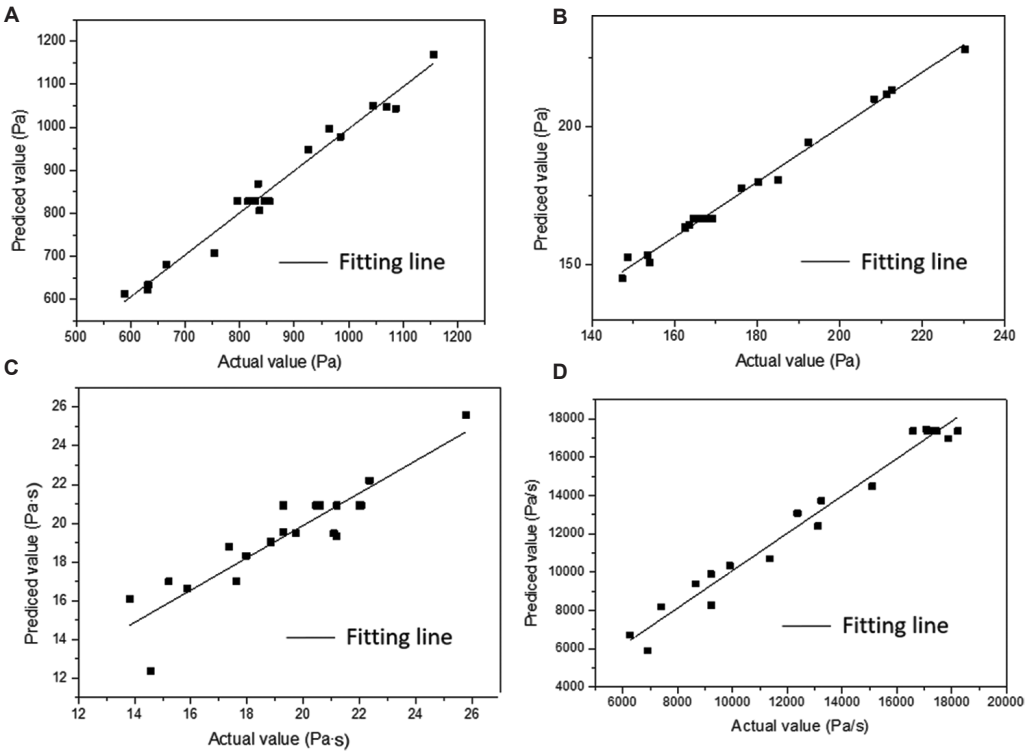

Figure 9. Predicted values vs actual values of different responses: (A) Static yield stress; (B) dynamic yield stress; (C) plastic viscosity; and (D) thixotropy.

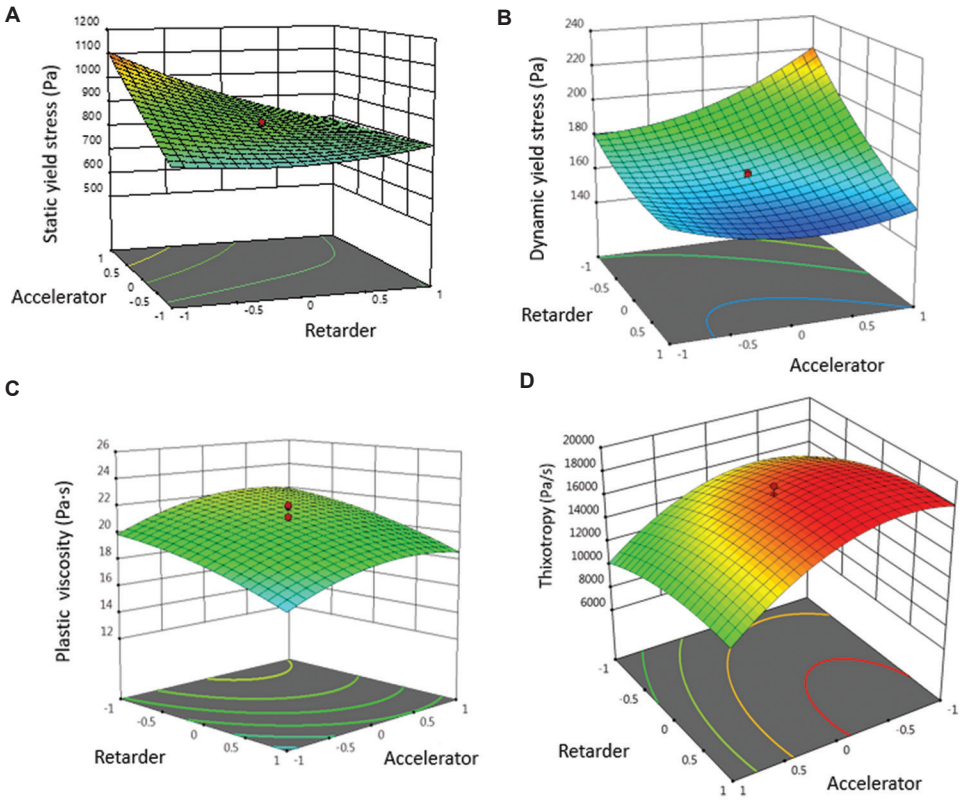

Figure 10. 3D response surface of different responses: (A) Static yield stress; (B) dynamic yield stress; (C) plastic viscosity; and (D) thixotropy.

Figure 11. Final printout of formulation No. 3.

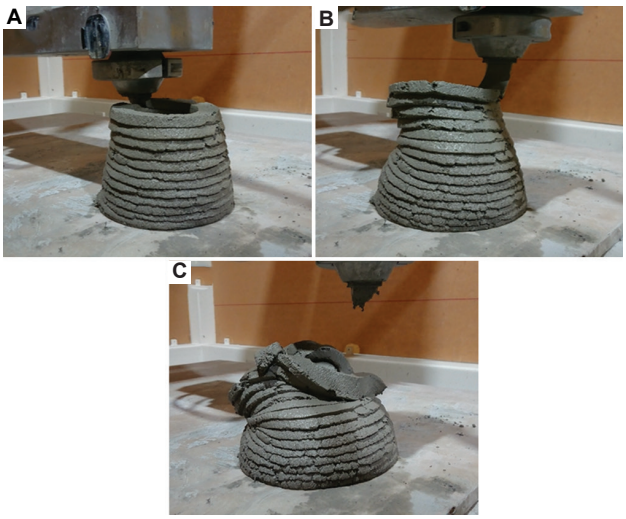

Figure 12. Printability test result of formulation No. 6: (A) Slight deformation appeared; (B) large deformation and misalignment occurred; and (C) final collapse occurred.

4.3. Printability test results

The mixture proportions of No.3 and No.6 in Table 4 were selected in printability test as they show the extremes of the rheological properties. The mixture proportion of No.3 possesses high yield stress (1,156 Pa) and high thixotropy (17,081 Pa/s). On the contrary, No.6 possesses a low yields stress (588.6 Pa) and low thixotropy (7,410 Pa/s). Final printed component with mixture proportion No.3 is illustrated in Figure 11. As shown from Figure 11, it indicates that the mixture proportion of No.3 can be printed well, and material can fully maintain its shape in the printing process.

However, mixture proportion of No.6 is not suitable for printing as shown in Figure 12. Large deformation of the structure occurred during the printing test since material static yield stress is insufficient to keep the printed layers to stand firmly; therefore, it is not suitable for 3D printing. Finally, the structure collapsed due to large deformation and misalignment. Therefore, materials with higher yield stress and higher thixotropy have better printability according to the printing test. The developed statistical models by using CCD can be an efficient method to optimize the dosage of chemical admixtures so that the material has the desired rheological properties, that is, high yield stress and high thixotropy, for 3DCP.

5. Conclusions

In this study, CCD was adopted to investigate the impact of chemical admixtures and their combined interactive effects on the rheological properties with respect of static/dynamic yield stress, plastic viscosity, and thixotropy. Two mixtures with the extremes of the rheological properties were selected for the printing test in this work. The printing test was successfully conducted when the mixture has high yield stress (1,156 Pa) and high thixotropy (17,081 Pa/s). However, the collapse happened during the printing test when materials have a low yields stress (588.6 Pa) and low thixotropy (7,410 Pa/s).

Four polynomial models are constructed to correlate the dosage of chemical admixtures with material rheological properties. The derived models are shown to be statistically significant based on ANOVA analysis. The results indicate that with an increase in the dosage of superplasticizer or retarder, the rheological properties decrease, while accelerator possesses an opposite effect on the rheological properties. The combined interactive effect of retarder and accelerator has a negative impact on the rheological properties. The interactive effect of retarder and superplasticizer possesses a positive impact on the dynamic yield stress, plastic viscosity, and thixotropy while it has a negative influence on the static yield stress. The interactive effect of accelerator and retarder has a positive influence on the yield stress whereas it possesses a negative impact on the plastic viscosity and thixotropy. The CCD derived model is not universally applicable since the results may possibly alter in conjunction with other factors such as the test range of parameters being studied. However, the CCD can minimize the efforts and time consumed in conducting experiments while obtaining sufficient information for data analysis. The method is particularly useful when one has to deal with a large number of variables in experiment. The second-order models can be further obtained through the CCD to make predictions.

Acknowledgments

None.

Funding

The authors would like to acknowledge The Hong Kong Polytechnic University (P0038598), BASF for the materials supply, National Research Foundation, Prime Minister's Office, Singapore under its Medium-Sized Centre funding scheme, Singapore Centre for 3D Printing and Sembcorp Design & Construction Pte Ltd for their funding and support in this research project.

Conflict of interest

The authors report that they have no affiliations with or involvement in any organization or entity with any financial interest in the subject matter or materials discussed in this manuscript.

Author contributions

Conceptualization: Mingyang Li, Yiwei Weng
Data curation: Mingyang Li, Yiwei Weng
Formal analysis: Mingyang Li, Yiwei Weng
Funding acquisition: Yiwei Weng, Teck Neng Wong
Investigation: Mingyang Li, Yiwei Weng, Zhixin Liu, Dong Zhang
Methodology: Mingyang Li, Yiwei Weng
Validation: Mingyang Li, Yiwei Weng, Zhixin Liu, Dong Zhang
Writing – original draft: Mingyang Li, Yiwei Weng
Writing – review & editing: Mingyang Li, Yiwei Weng, Teck Neng Wong

References

1. Lu B, Tan MJ, Qian S, 2016, A review of 3D printable construction materials and applications. In: Proceedings 2nd International Conference on Progress in Additive Manufacturing. (Pro-AM 2016), pp330–335.

   https://doi.org/10.1063/1.1465107

2. Kondepudi K, Subramaniam KV, Nematollahi B, *et al*., 2022, Study of particle packing and paste rheology in alkali activated mixtures to meet the rheology demands of 3D Concrete Printing. *Cem Concr Compo*, 131: 104581.

   https://doi.org/10.1016/j.cemconcomp.2022.104581

3. Xu J, Buswell RA, Kinnell P, *et al*., 2020, Inspecting manufacturing precision of 3D printed concrete parts based on geometric dimensioning and tolerancing. *Autom Constr*, 117: 103233.

   https://doi.org/10.1016/j.autcon.2020.103233

4. Weng Y, Li M, Ruan S, *et al*., 2020, Comparative economic, environmental and productivity assessment of a concrete bathroom unit fabricated through 3D printing and a precast approach. *J Clean Prod*, 261: 121245.

   https://doi.org/10.1016/j.jclepro.2020.121245

5. Zhu B, Pan J, Nematollahi B, *et al*., 2019, Development of 3D printable engineered cementitious composites with ultra-high tensile ductility for digital construction. *Mater Des*, 181: 1–12.

   https://doi.org/10.1016/j.matdes.2019.108088

6. Buswell R, da Silva WR, Bos P, *et al*, (2020), A process classification framework for defining and describing digital fabrication with concrete. *Cem Concr Res*, 134: 106068.

   https://doi.org/10.1016/j.cemconres.2020.106068

7. Weng Y, Li M, Liu Z, *et al*., 2019, Printability and fire performance of a developed 3D printable fibre reinforced cementitious composites under elevated temperatures. *Virtual Phys Prototyp*, 14: 284–292.

   https://doi.org/10.1080/17452759.2018.1555046

8. Weng Y, Lu B, Li M, *et al*., 2018, Empirical models to predict rheological properties of fiber reinforced cementitious composites for 3D printing. *Constr Build Mater*, 189: 676–685.

   https://doi.org/10.1016/j.conbuildmat.2018.09.039

9. Liu Z, Li M, Weng Y, *et al*., 2019, Tan, mixture design approach to optimize the rheological properties of the material used in 3D cementitious material printing. *Constr Build Mater*, 198: 245–255.

   https://doi.org/10.1016/j.conbuildmat.2018.11.252

10. Ivanova I, Ivaniuk E, Bisetti S, *et al*., 2021, Comparison between methods for indirect assessment of buildability in fresh 3D printed mortar and concrete. *Cem Concr Res*, 156: 106764.

    https://doi.org/10.1016/j.cemconres.2022.106764

11. Weng Y, Li M, Tan MJ, *et al*., 2018, Design 3D printing cementitious materials via Fuller Thompson theory and Marson-Percy model. *Constr Build Mater*, 163: 600–610.

    https://doi.org/10.1016/j.conbuildmat.2017.12.112

12. Roussel N, 2018, Rheological requirements for printable concrete. *Cem Concr Res*, 112: 76–85.

    https://doi.org/10.1016/j.cemconres.2018.04.005

13. Marchon D, Kawashima S, Bessaies-Bey H, *et al*., 2018, Hydration and rheology control of concrete by admixtures for digital fabrication. *Cem Concr Res*, 112: 96–110.

    https://doi.org/10.1016/j.cemconres.2018.05.014

14. Buswell R, Silva WR, Jones SZ, *et al*., 2018, Dirrenberger, 3D printing using concrete extrusion: A roadmap for research. *Cem Concr Res*, 112: 37–49.

    https://doi.org/10.1016/j.cemconres.2018.05.006

15. Zhang Y, Zhang Y, She W, *et al*., 2019, Rheological and harden properties of the high-thixotropy 3D printing concrete. *Constr Build Mater*, 201: 278–285.

    https://doi.org/10.1016/j.conbuildmat.2018.12.061

16. Zhang Y, Zhang Y, Yang L, *et al*., 2021, Hardened properties and durability of large-scale 3D printed cement-based materials. *Mater Struct*, 54: 45.

https://doi.org/10.1617/s11527-021-01632-x

17. Zhang Y, Zhang Y, Liu G, *et al*., 2018, Fresh properties of a novel 3D printing concrete ink. *Constr Build Mater*, 174: 263–271.

https://doi.org/10.1016/j.conbuildmat.2018.04.115

18. Dressler I, Freund N, Lowke D, 2020, The effect of accelerator dosage on fresh concrete properties and on interlayer strength in shotcrete 3D printing. *Materials (Basel)*, 13: 13020374.

https://doi.org/10.3390/ma13020374

19. Zhang C, Nerella VN, Krishna A, *et al*., 2021, Mix design concepts for 3D printable concrete: A review. *Cem Concr Compos*, 122: 104155.

https://doi.org/10.1016/j.cemconcomp.2021.104155

20. Yu S, Sanjayan J, Du H, 2022, Effects of cement mortar characteristics on aggregate-bed 3D concrete printing. *Addit Manuf*, 58: 103024.

https://doi.org/10.1016/j.addma.2022.103024

21. Yu S, Du H, Sanjayan J, 2020, Aggregate-bed 3D Concrete Printing with Cement Paste Ink. *Cem Concr Res*, 136: 106169.

https://doi.org/10.1016/j.cemconres.2020.106169

22. Wangler T, Pileggi R, Gürel S, *et al*., 2022, A chemical process engineering look at digital concrete processes: Critical step design, inline mixing, and scaleup. *Cem Concr Res*, 155: 106782.

https://doi.org/10.1016/j.cemconres.2022.106782

23. Ramakrishnan S, Kanagasuntharam S, Sanjayan J, 2022, In-line activation of cementitious materials for 3D concrete printing. *Cem Concr Compos*, 131: 104598.

https://doi.org/10.1016/j.cemconcomp.2022.104598

24. Rubio-Hernández FJ, Adarve-Castro A, Velázquez-Navarro JF, *et al*., 2020, Influence of water/cement ratio, and type and concentration of chemical additives on the static and dynamic yield stresses of Portland cement paste. *Constr Build Mater*, 235: 117744.

https://doi.org/10.1016/j.conbuildmat.2019.117744

25. Liu JC, Tan KH, Zhang D, 2017, Multi-response optimization of post-fire performance of strain hardening cementitious composite. *Cem Concr Compos*, 80: 80–90.

https://doi.org/10.1016/j.cemconcomp.2017.03.001

26. Jones R, 2000, Design and Analysis of Experiments. 5th ed. Hoboken: Wiley.

https://doi.org/10.1002/qre.458

27. Chen L, Zhang Z, Gong W, *et al*., 2015, Liang, Quantifying the effects of fuel compositions on GDI-derived particle emissions using the optimal mixture design of experiments. *Fuel*, 154: 252–260.

https://doi.org/10.1016/j.fuel.2015.03.081

28. Chen L, Liang Z, Liu H, *et al*., 2017, Sensitivity analysis of fuel types and operational parameters on the particulate matter emissions from an aviation piston engine burning heavy fuels. *Fuel*, 202: 520–528.

https://doi.org/10.1016/j.fuel.2017.04.052

29. Chen L, Liu Z, Sun P, *et al*., 2015, Formulation of a fuel spray SMD model at atmospheric pressure using Design of Experiments (DoE). *Fuel*, 153: 355–360.

https://doi.org/10.1016/j.fuel.2015.03.013

30. Jiao D, Shi C, Yuan Q, *et al*, (2018), Mixture design of concrete using simplex centroid design method. *Cem Concr Compos*, 89: 76–88.

https://doi.org/10.1016/j.cemconcomp.2018.03.001

31. Perrot A, Rangeard D, Pierre A, 2016, Structural built-up of cement-based materials used for 3D-printing extrusion techniques. *Mater Struct*, 49: 1213–1220.

https://doi.org/10.1617/s11527-015-0571-0

32. Lu B, Li M, Neng T, *et al*, (2021), Effect of printing parameters on material distribution in spray-based 3D concrete printing (S-3DCP), *Autom Constr*, 124: 103570.

https://doi.org/10.1016/j.autcon.2021.103570

33. Roussel N, 2007, A theoretical frame to study stability of fresh concrete. *Mater Struct*, 39: 81–91.

https://doi.org/10.1617/s11527-005-9036-1

34. Wu D, Cai SJ, Huang G, 2014, Coupled effect of cement hydration and temperature on rheological properties of fresh cemented tailings backfill slurry. *Trans Nonferrous Met Soc China*, 24: 2954–2963.

https://doi.org/10.1016/S1003-6326(14)63431-2

35. Chen M, Liu B, Li L, *et al*., 2020, Cheng, Rheological parameters, thixotropy and creep of 3D-printed calcium sulfoaluminate cement composites modified by bentonite, Compos. *Part B Eng*, 186: 107821.

https://doi.org/10.1016/j.compositesb.2020.107821

Materials Science in Additive Manufacturing

ORIGINAL RESEARCH ARTICLE

Characterization of triply periodic minimal surface structures obtained using toolpath-based construction design

Shujie Tan[1], Xi Zhang[1], Ziyu Wang[1], Liping Ding[1], Wenliang Chen[1], Yicha Zhang[2]*

[1]College of Mechanical and Electrical Engineering, Nanjing University of Aeronautics and Astronautics, Nanjing, P. R. China

[2]ICB-COMM, UMR 6303, CNRS, Univ. Bourgogne Franche-Comté, UTBM, Belfort, France

Abstract

Triply periodic minimal surface (TPMS) cellular structures of Ti6Al4V with theoretically calculated relative densities ranging from 4% to 22.6% were designed using a toolpath-based construction method and fabricated by laser powder bed fusion, and their macrostructure, microstructure, and compression performance were investigated. The results indicated that the macrostructure was the same as that of TPMS structures designed using the traditional method. In contrast, the microstructures of the as-built samples and the samples after stress-relief annealing were slightly different from those of the traditional ones. Moreover, compression test results of the Schwarz-P structures showed that the compressive modulus was positively related to the calculated relative density, and a Gibson-Ashby model was established to quantitatively describe the relationship between the compressive modulus and theoretical relative density. The findings of this work show that the mechanical performance of a TPMS structure obtained using a toolpath-based construction design can be accurately predicted using geometric parameters or printing toolpaths. This will be helpful during the design stage.

Keywords: Additive manufacturing; Compression test; Laser powder bed fusion; Toolpath-based construction design; Triply periodic minimal surface structure

***Corresponding author:**
Yicha Zhang
(yicha.zhang@utbm.fr)

Citation: Tan S, Zhang X, Wang Z, *et al*., 2022, Characterization of triply periodic minimal surface structures obtained using toolpath-based construction design. *Mater Sci Add Manuf*. 1(3): 17.
https://doi.org/10.18063/msam.v1i3.17

Received: July 31, 2022

Accepted: September 5, 2022

Published Online: September 21, 2022

Copyright: © 2022 Author(s). This is an Open Access article distributed under the terms of the Creative Commons Attribution License, permitting distribution, and reproduction in any medium, provided the original work is properly cited.

Publisher's Note: Whoice Publishing remains neutral with regard to jurisdictional claims in published maps and institutional affiliations.

1. Introduction

At present, additive manufacturing (AM), especially the powder bed fusion (PBF) process, plays an important role in the biomedical, aerospace, automotive, and heat exchanger manufacturing industries[1-3]. Due to its ability to fabricate freeform surfaces, AM greatly expands design freedom. In industry, an increasing number of components with extremely complex shapes, such as lattices, Voronoi foam, triply periodic minimal surfaces (TPMSs), and topological shapes, have been designed, fabricated, and applied[4,5] because of their excellent physical and mechanical properties. Researchers have also focused on the design methods[6,7], manufacturing evaluation[8,9], and performance[10,11] of these structures with complex shapes. However, according to the literature and our own studies, there are at least three unsolved problems in the manufacturing chain when

using laser PBF (LPBF) to manufacture such structures on an industrial scale. The first is the limitations of the stereolithography (STL) file format. It is difficult and time-consuming for commercial pre-processing software (i.e., Magics, Voxel Dance, and P3Ds) to handle the STL model of lattice/cellular structures created by scholars using the proposed novel design methods when the number of structural units exceeds ten thousand or more. Second, it is difficult to evaluate the manufacturability and manufacturing results of such complex structures because traditional evaluation methods are unsuitable for AM processes[8]. Finally, the performance (i.e., physical and mechanical properties, and failure mechanism) of such novel structures is still unclear, although many scholars have focused on this topic.

To solve the first problem, Ding *et al.*[12] proposed an STL-free design and manufacturing paradigm for high-precision PBF, and Feng *et al.*[13,14] proposed an efficient generation strategy for hierarchical porous scaffolds with freeform external geometries. Both groups simplified the three-dimensional (3D) calculations to two-dimensional (2D) operations to improve the calculation efficiency. However, the infilling efficiency remains a problem. Similar to this simplified method, we proposed a toolpath-based construction method for designing and printing porous structures in a previous study[15]. In our method, we used a toolpath pattern to infill the hull model, directly generating the toolpath of the porous structure. Compared with the traditional pre-processing method, the toolpath-based construction method exhibits a significant advantage in terms of toolpath precision and generating efficiency.

However, as mentioned above, to apply cellular structures generated by toolpath-based construction on an industrial scale, the manufacturability/manufacturing results and structural performance still need to be investigated. Although we analyzed the manufacturability of a cellular structure generated using the toolpath-based construction method and developed a manufacturability predictor for these structures in previous papers[15,16], we did not investigate the performance of structures generated by the toolpath-based method.

Yan *et al.*[17] evaluated the manufacturability and performance of LPBF-produced TPMS gyroid lattice structures. They found that the yield strength and Young's modulus of the gyroid lattice structures increased with decreasing unit cell size because of the denser struts of the lattice structures with smaller unit cell sizes. In another study, Yan *et al.*[18] established two equations based on the Gibson-Ashby model to predict the compression properties of the 316L stainless steel gyroid lattice structures; however, there were differences between the experimentally tested values and the values predicated by the Gibson-Ashby model. Many other scholars have investigated the microstructure and mechanical deformation behavior of LPBF-produced lattice structures. However, to the best of our knowledge, all of these studies used the conventional AM data-processing method when printing the lattice structure. As pointed out by Neikter *et al.*[19], the microstructure of LPBF-produced samples is related to the laser scanning strategy, that is, the toolpath. However, the toolpath generated by the toolpath-based construction method is different from that generated by commercial AM data pre-processing software. Hence, it is unknown whether the performance of a lattice structure fabricated using toolpath-based construction design is the same as that of the traditionally designed structures.

In summary, there is a gap in knowledge regarding the microstructure and mechanical performance of lattice structures obtained using toolpath-based design. To fill this gap, we fabricated a TPMS Schwarz-P structure using our proposed method and investigated its microstructure and mechanical performance. The rest of the paper is organized as follows: Section 2 introduces the experimental materials and methods, Section 3 gives the experimental results and discusses the results, and we conclude with Section 4.

2. Materials and methods

2.1. TPMS Schwarz-P surface

A TPMS is an implicit surface with zero mean curvature[3]. Owing to their smooth surfaces and highly interconnected porous architectures, TPMS structures have been applied in many domains. The Schwarz-P surface is a typical type of TPMS. Equation I gives its mathematical expression, and Figure 1 shows Schwarz-P surfaces with different unit sizes and shape factors.

$$\varphi_{\mathrm{P}}(x,y,z): \cos\frac{2\pi}{k}x+\cos\frac{2\pi}{k}y+\cos\frac{2\pi}{k}z=c \qquad \text{(I)}$$

2.2. Toolpath-based construction method

In this study, a toolpath-based construction method was used to construct and generate printing toolpaths for the TPMS-Schwarz-P structures. Figure 2 shows the workflow of the printing toolpath generation of the TPMS-Schwarz-P structure through the toolpath-based construction method. The hull model, AM parameters, and mathematical equation of the Schwarz-P surface and its corresponding toolpath pattern were used as the input variables in this method. As shown in Figure 2, the box model was first sliced at a fixed thickness to obtain the layer contours. Then, the layer contours were used to construct the polygons to be infilled. Finally, the polygons

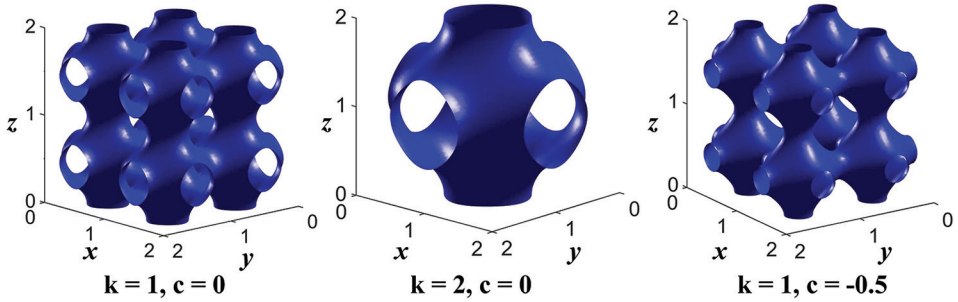

Figure 1. Schwarz-P surface with different parameters.

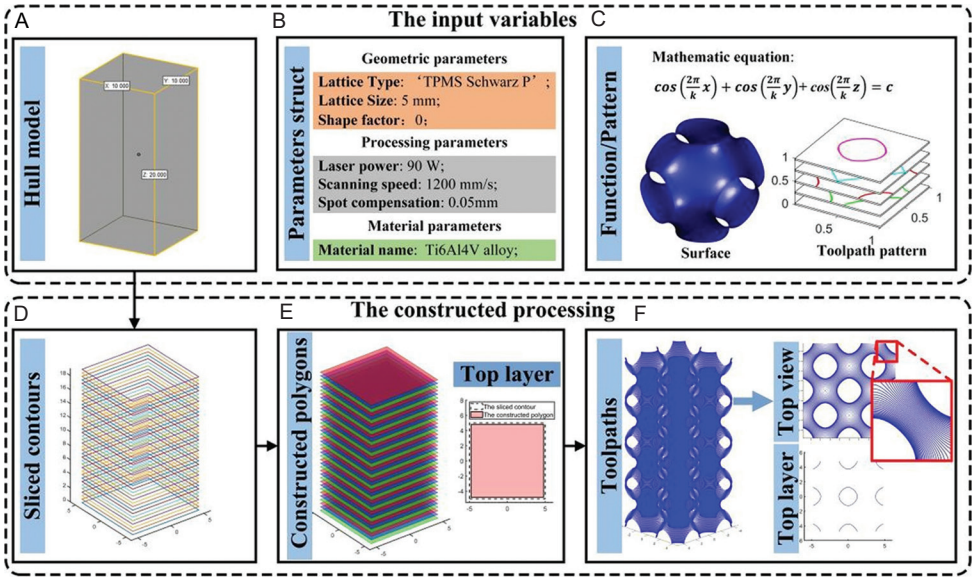

Figure 2. Workflow of the toolpath-based construction method.

were infilled using the Schwarz-P toolpath pattern. More details about the toolpath-based construction method can be found in our previous studies[20,21].

Figure 3 exhibits the STL model of TPMS Schwarz-P structure, and its printing toolpaths generated by different methods. According to Figure 3, our observations are as follows: (i) the toolpaths generated by our method are smoother than those generated by Magics; and (ii) the toolpaths generated by Magics contain closed contours whether the thin wall optimization is selected. In this case, the wall thickness of the structure depended on the contours and their processing parameters. Opposite to Magics, our method used single-curve rather than contour as the printing toolpath. For this single-toolpath structure obtained through the toolpath-based construction method, the wall thickness was determined by the processing parameters, that is, the laser power and scanning speed. Without any hatching in the toolpath, the microstructure and mechanical performance of this Schwarz-P structure differed slightly from those of the CAD model-based structure.

2.3. LPBF processing and materials

Gas-atomized Ti6Al4V powder supplied by ZhongHangMaiTe (China) was selected as the raw material in this study. Figure 4A presents the spherical morphology of the Ti6Al4V powder, and Table 1 lists the chemical composition. The size distributions were D10 = 18.6 μm, D50 = 34.3 μm, and D90 = 57.6 μm. The Ti6Al4V Schwarz-P structures were printed on a 150-mm diameter titanium alloy substrate under an argon protective atmosphere using a commercial SLM printer (Ti150, Profeta, China). The Ti150 printer (Figure 4B) was equipped with an IPG Photonics fiber laser, delivering a maximum power of P = 200 W at λ = 1064 nm and having a laser spot size of 50 μm.

Twenty-five samples (10 × 10 × 20 mm) with different geometric parameters were fabricated for compression, and four samples (10 × 10 × 5 mm) with the same

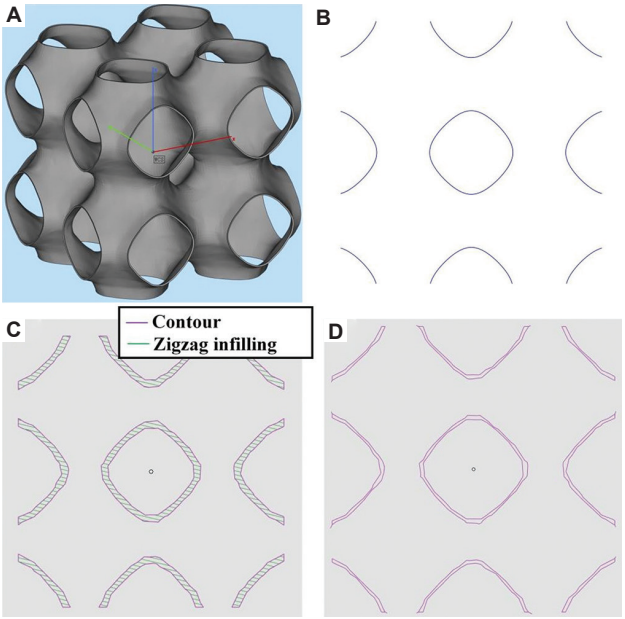

Figure 3. Model and its printing toolpaths generated by different methods. (A) STL model of TPMS Schwarz-P structure. Toolpaths generated by (B) our method, (C) Magics without spot compensation and thin-wall optimization, and (D) Magics with spot compensation and thin-wall optimization.

geometric parameters were fabricated for microstructural characterization. The samples were designated as A0-A0.8, B0-B0.8, C0-C0.8, D0-D0.8, E0-E0.8, and F1-F4. An illustration of the orientation, sample dimensions, and distribution within the substrate for these Schwarz-P structures is shown in Figure 5A. In this study, the laser power, scanning speed, and printing layer thickness were 90 W, 1100 mm/s, and 30 μm, respectively. The oxygen content was less than 0.1%. After printing, F1 and F3 were immediately cut by wire electrical discharge machining (WEDM), whereas the remaining samples were heat treated to relieve the residual thermal stress before cutting. Figure 5B illustrates the stress-relief heat treatment process. The geometric parameters and corresponding theoretical porosities are listed in Table 2. Here, we assumed that the width of the melt track would not change

Table 1. Composition of Ti6Al4V powder

Main ingredients	Ti	Al		V	
Content/%	Bal	5.50-6.75		3.50-4.50	
Minor ingredients	Fe	C	N	H	O
Content/%	≤ont	≤onte	≤onte	≤onten	≤ont

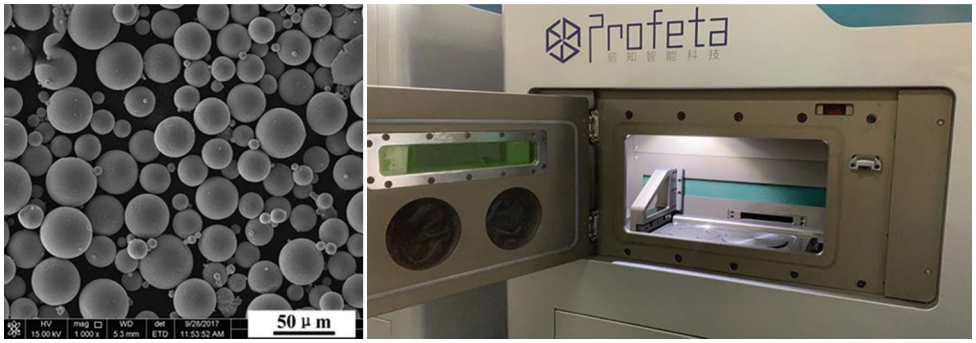

Figure 4. Material and Ti150 machine.

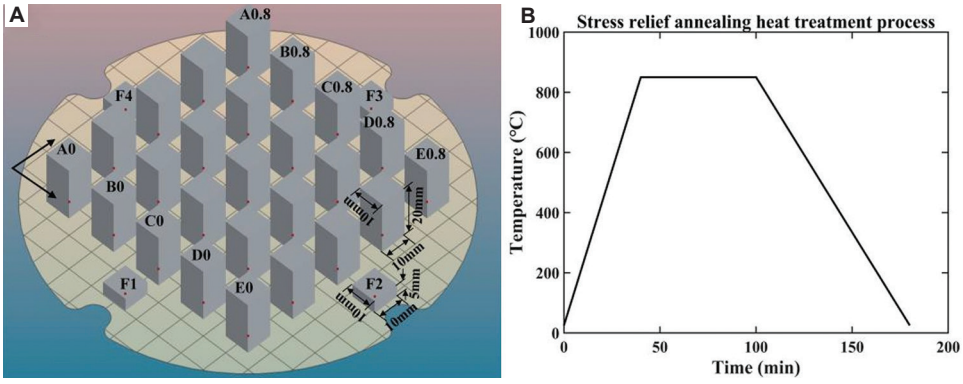

Figure 5. (A) An illustration of the orientation, sample dimensions, and distribution within the substrate for the fabricated samples. (B) An illustration of the stress relief heat treatment to the fabricated samples.

Table 2. The geometric parameters and processing parameters of the Schwarz-P structures

No.	Lattice size	Shape factor	Theoretical relative density
A0	1	0	0.2262
A0.2	1	0.2	0.2244
A0.4	1	0.4	0.2201
A0.6	1	0.6	0.2124
A0.8	1	0.8	0.2003
B0	2	0	0.1130
B0.2	2	0.2	0.1122
B0.4	2	0.4	0.1101
B0.6	2	0.6	0.1062
B0.8	2	0.8	0.1001
C0	3	0	0.0712
C0.2	3	0.2	0.0719
C0.4	3	0.4	0.0725
C0.6	3	0.6	0.0735
C0.8	3	0.8	0.0710
D0	4	0	0.0565
D0.2	4	0.2	0.0561
D0.4	4	0.4	0.0550
D0.6	4	0.6	0.0531
D0.8	4	0.8	0.0501
E0	5	0	0.0452
E0.2	5	0.2	0.0449
E0.4	5	0.4	0.0440
E0.6	5	0.6	0.0425
E0.8	5	0.8	0.0401
F1-F4	1	0	0.2262

when the processing parameters remained the same. We also considered the cross-sectional shape of the melt track to be a rectangle and neglected the overlap in the corner. Under this assumption, the theoretical relative density of the Schwarz-P structure with no hatched toolpath was calculated as follows:

$$d_{tr} = \frac{\rho_p}{\rho_s} = \frac{w \times h \times \sum len_i}{V} \quad \text{(II)}$$

Where d_{tr} is the theoretical relative density of the Schwarz-P structure, w is the width of the melt track, h is the layer thickness, len_i is the length of the ith toolpath, and V is the volume of the hull model of the Schwarz-P structure. In this study, the layer thickness h is 0.03mm, and the melt track width w is 0.12 mm when laser power, scanning speed and laser spot diameter are 90 W, 1100 mm/s and 50 μm, respectively.

2.4. Material characterization and mechanical properties

The macrostructure of the Schwarz-P structures (A0-E0.8) was analyzed using optical microscopy (OM; HiROX RH-2000, Japan) and scanning electron microscopy (SEM). Electron backscatter diffraction (EBSD) was used to further analyze the grain structure and phase distribution of the remaining four samples (F1 – F4). The Schwarz-P samples for EBSD were mechanically polished and then argon ion-polished for 5 h at 4 kV voltage and 2 angles. The mass of each structure was measured using an analytical balance (BSS224S, Hengda, China), and the relative density d_{mr} was calculated as follows:

$$d_{mr} = \frac{m_p}{V \times \rho_s} \quad \text{(III)}$$

Where m_p is the mass of the Schwarz-P structure, V is the volume of the Schwarz-P structure, and ρ_s= 4.43g/cm^3 is the density of the dense Ti6Al4V alloy.

Static uniaxial compression experiments were performed using a cmt5305 machine based on the ISO 13314:2011 standard[22]. Compression tests were conducted at room temperature at a constant rate of 2 mm/min. Three identical samples were tested for each Schwarz-P structure. After the test, the fracture surface morphology of each sample was examined using SEM.

According to the Gibson-Ashby model, mechanical properties are related to the relative density of open-cell porous structures[23]. Equation IV gives the relationship between the elastic modulus and relative density.

$$\frac{E_p}{E_s} = C_1 \left(\frac{\rho_p}{\rho_s} \right)^{n_1} \quad \text{(IV)}$$

Where E_p is the elastic modulus of the porous structure, E_S is the elastic modulus of the bulk material, and for Ti6Al4V alloy, E_S = 110 GPa. ρ_p and ρ_s are the porous and dense material density, respectively. C_1 and n_1 are the coefficients and can be calculated by fitting the test results into Equation IV. Normally, C_1 is in the range of 0.1 to 4, and n_1 equals to 2. It must be pointed out that, compared with the real measured relative density, we thought that the theoretically calculated value is more suitable for Equation IV. The reason is detailed in section 3.1.

3. Results and discussion

3.1. Macrostructural analysis

Figures 6A–E present the manufacturing samples of Schwarz-P structures with different geometric parameters. Figures 6F–H show enlarged images of regions A1,

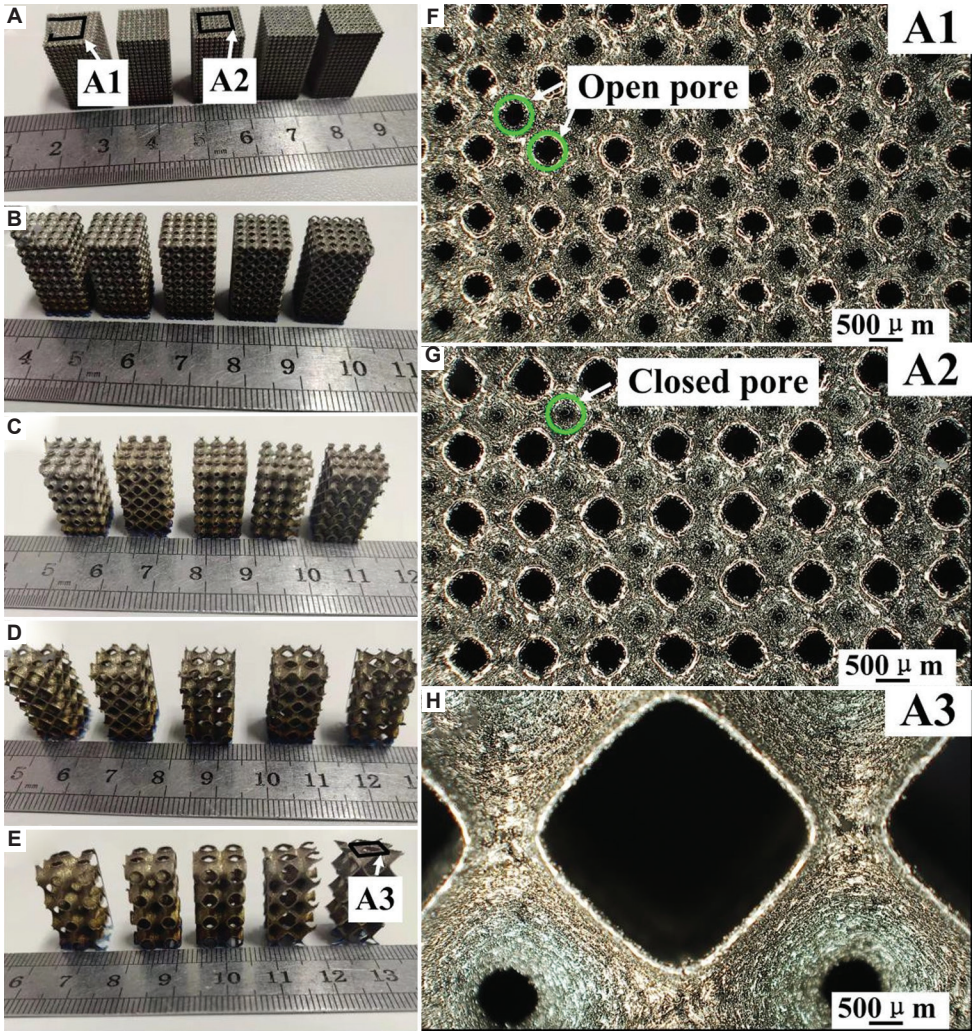

Figure 6. The manufacturing samples of Schwarz-P structures with different geometric parameters. (A) A0, A0.2, A0.4, A0.6, A0.8. (B) B0, B0.2, B0.4, B0.6, B0.8. (C) C0, C0.2, C0.4, C0.6, C0.8. (D) D0, D0.2, D04, D0.6, D0.8. (E) E0, E0.2, E0.4, E0.6, E0.8. (F), (G), and (H) show the enlarged images of regions A1, A2, and A3, respectively.

A2, and A3, respectively. As shown in Figure 6, all the Schwarz-P structures were successfully fabricated; however, inconsistent with the designs, several structures (A0.4, A0.6, and A0.8) had closed pores. Theoretically, the Schwarz-P surface divides the space into two independent regions; however, there is width to the melt track, and pores will close if the pore size is smaller than the width of the melt track, resulting in many closed cavities filled with unmelted powder particles. Typically, the width of the Ti6Al4V melt track at the given processing parameters in this study (laser power = 120 W, scanning speed = 1100 mm/s, layer thickness = 0.03 mm, and laser spot diameter = 0.05 mm) was 120 μm. However, as we found in our previous study[15], this width increased significantly in the corner of the toolpath. The closed toolpath shown by the galvanometer scanning system was not a smooth curve with G2 continuous; rather, it was a polyline with many corners/vertices. Hence, the width of the melt track of the small pore became much larger than we expected. Figure 7 depicts variations between the actual pore size and the designed geometric parameters of the Schwarz-P structure. As the shape factor increases, the minimal pore size decreases; in contrast, as the unit size increases, the minimal pore size increases. In addition, an interesting phenomenon, as shown in Figure 7J, is that the structure had some broken holes, meaning that when the unit size was >5 mm, the Schwarz-P structure did not satisfy the AM constraints.

Figure 8 presents a comparison of the theoretical and measured relative densities of the Schwarz-P structures. As shown in the figure, except for samples A0.4, A0.6, and A0.8, the theoretically calculated results are consistent with the measured results. As shown in Figure 5, samples A0.4,

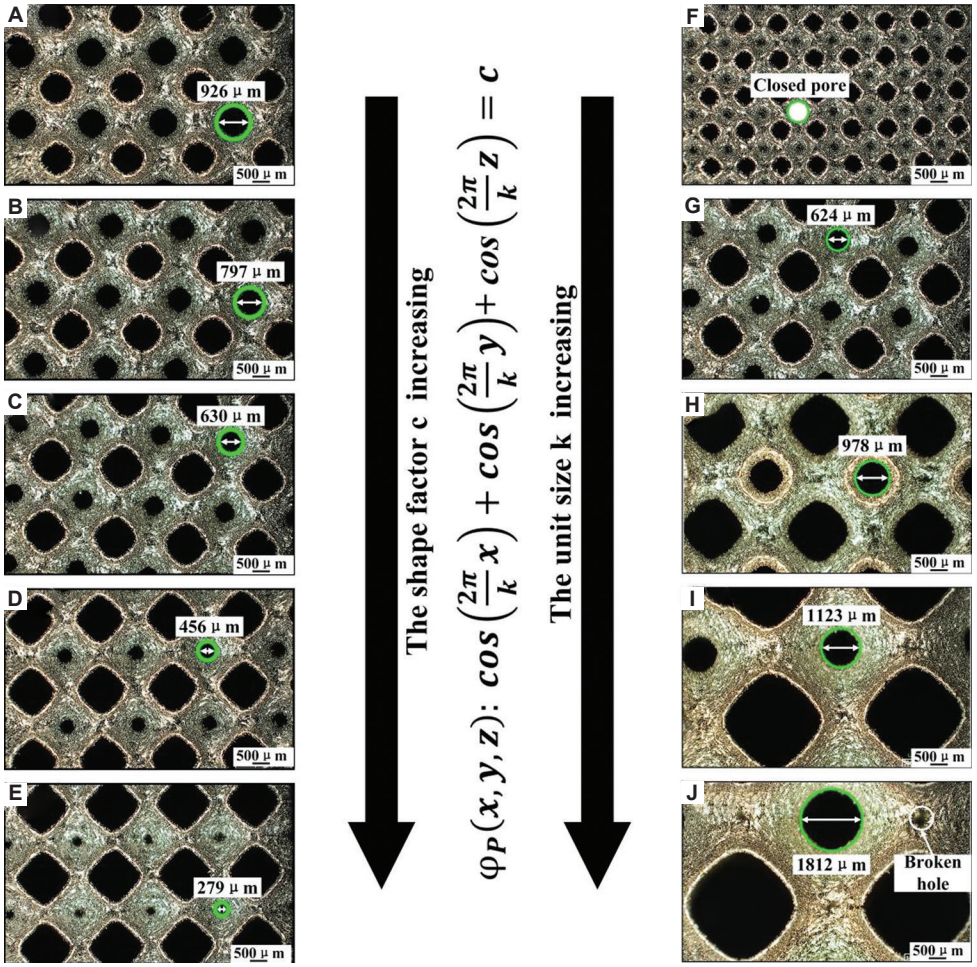

Figure 7. The variations between the real pore size and design geometric parameters of the Schwarz-P structure. (A-E) show the top views of samples B0, B0.2, B0.4, B0.6, and B0.8, respectively. (F-J) show the top views of samples A0.4, B0.4, C0.4, D0.4, and E0.4, respectively.

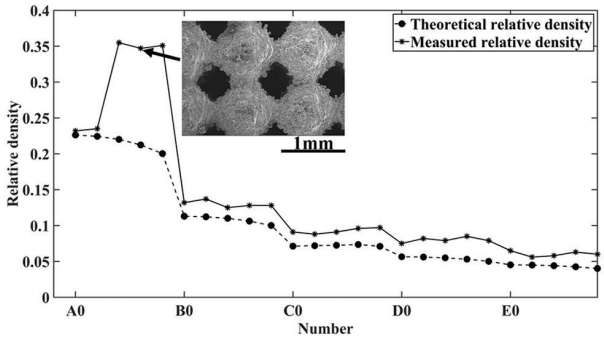

Figure 8. Comparing results of the theoretical and the measured relative density.

A0.6, and A0.8 had some closed cavities filled with unmelted powder particles, which is why the measured relative densities of these samples were much greater than the theoretically calculated results. In addition, the measured results were slightly greater than the theoretical results. This is because some semi-melted powder became attached to the surface. However, when we calculated the theoretical relative density, we used the width of the polished samples, neglecting the attached powder. Moreover, on comparing the theoretical relative densities of samples A0, B0, C0, D0, and E0 (or other samples with the same shape factor but different unit sizes), it was found that when the shape factor remained constant, the theoretical relative density of the Schwarz structure decreased rapidly with increasing unit size. On comparing the theoretical relative densities of samples A0, A0.2, A0.4, A0.6, and A0.8 (or other samples with the same unit size and different shape factors), when the unit size remained constant, the theoretical relative density decreased with increasing shape factor; however, the change was very small and almost negligible.

Therefore, we considered that the measured relative density did not reflect the actual densification of the Schwarz-P structures because the partially melted and unmelted powder particles attached to the

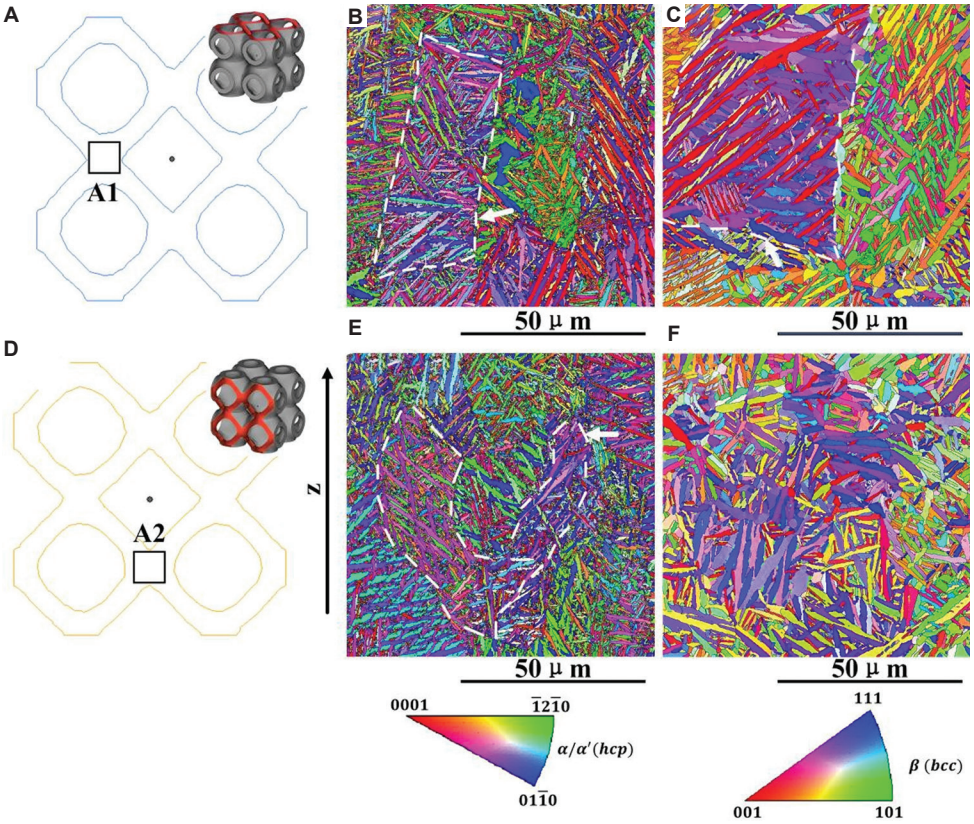

Figure 9. The EBSD orientation maps of the as-built and the heat treatment structures. (A) and (D) show the diagrams of the top and side scanning regions, respectively. (B) As-built structure, region A1. (C) Structure after stress relief heat treatment, region A1. (E) As-built structure, region A2. (F) Structure after stress relief heat treatment, region A2.

structural surface affected the measurement results. Hence, in the remainder of this study, the theoretically calculated relative density, instead of the measured value, was used.

3.2. Microstructure analysis

In general, the solidification of Ti6Al4V during printing process starts with the melted deposit, which consists of the liquid β phase. As reported by Zhao *et al.*[24], due to the high cooling rates, further cooling leads to the transformation from the β phase to martensite phase (α') phase during the LPBF process. Figure 9A and D show the scanning regions of the EBSD maps, and Figure 9B and E and Figure 8C and F show the microstructures of the as-built and heat-treated Ti6Al4V samples, respectively. As shown in Figure 9B and E, the EBSD orientation maps of the as-built Ti6Al4V samples show that the original β grains and acicular α/α' within each β grain. The white dotted lines in the figures indicate the original β grain boundaries. Compared with the results reported by Chang *et al.*[25] and Vrancken *et al.*[26], the length of the original β grains in this study is smaller (approximately 25 μm). Meanwhile, as reported by Zhao *et al.*[24], the original β columnar grains are parallel to

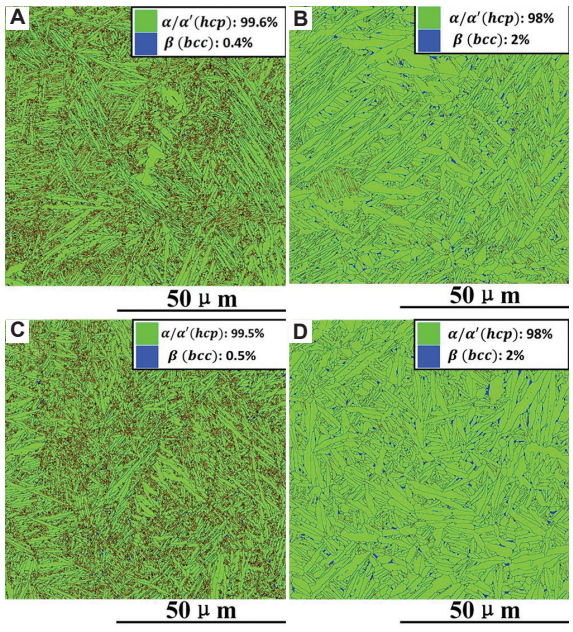

Figure 10. EBSD phase mapping of the LPBF-produced Schwarz-P structures. (A) and (C) show the phase mapping of region A1 and A2 in the as-built samples, respectively. (B) and (D) show the phase mapping of region A1 and A2 in the samples after stress relief heat treatment.

the build direction. However, as shown in Figure 9E, the orientation of the original β columnar grains was tilted, and this phenomenon is more obvious in the samples after heat treatment (Figure 9F).

Figure 10 shows the phase composition of the LPBF-produced Schwarz-P structures. As shown in Figure 9A and C, <0.5% body center β phase can be found in the as-built samples, while 2% β phase exists in the samples after stress relief heat treatment. The β phase is presented as a dot between the α/α' phase.

3.3. Mechanical performance behavior

Figure 11 shows the compressive modulus and maximum compressive stress of the Schwarz-P structures with different parameters. The structure with the largest elastic modulus is sample A0.6 (elastic modulus of 2.23 GPa), whereas that with the smallest elastic modulus is sample E0.2 (elastic modulus of 0.097 GPa). Similarly, the structure with the largest maximum compressive stress is sample A0.8 (maximum compressive stress of 101 MPa), whereas that with the smallest compressive stress is sample E0.2 (maximum compressive stress of 2.5 MPa). In addition, it can be seen from Figures 11A and B that when the shape factor was constant, the elastic modulus and maximum compressive stress of the Schwarz-P structure decreased with increasing unit size. Meanwhile, when the unit size was constant, the elastic modulus and maximum compressive stress changed very little. Comparing these results with those mentioned in Section 3.1, it is apparent that the effect of the unit size and shape factor on the elastic modulus and maximum compressive stress is consistent with the effect on the theoretical relative density.

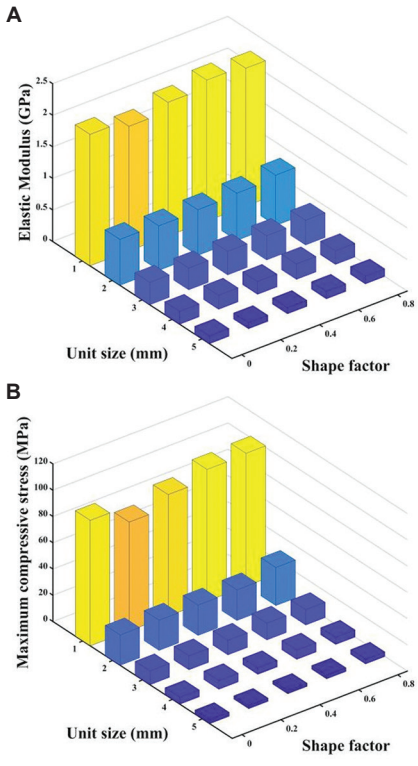

Figure 11. Compression modulus (A) and compressive stress (B) for Schwarz-P structures with different parameters.

To quantitatively investigate the relationship between the elastic modulus and the theoretical relative density, the Gibson-Ashby model was used to describe the experimental results. As mentioned above, the coefficient *n1* in the Gibson-Ashby model normally equals *t* for an open-cell structure. Two Gibson-Ashby equations were used to fit the results to better evaluate the elastic modulus of the Schwarz-P structure. As given by Equations V and VI, one has a fixed *n1* = 2, whereas the other does not. Figure 12 presents the fitting plots based on Equations V and VI, which describe the relationship between the relative elastic modulus of the LPBF-produced Ti6Al4V Schwarz-P structure with respect to the theoretical relative density. Both Gibson-Ashby equations fit well. The first fitting line for the elastic modulus (line 1, marked red in Figure 12) gives the relationship $E_p/E_s = 0.31(\rho_p/\rho_s)^{1.76}$, with a fitting R^2 value of 0.9729, whereas the second fitting line for the elastic modulus (line 2, marked blue in Figure 12) gives the relationship $E_p/E_s = 0.56(\rho_p/\rho_s)^2$, with a fitting R^2 value of 0.9546. The results indicated that the revised model (Equation V) performed better than the commonly used model (Equation VI).

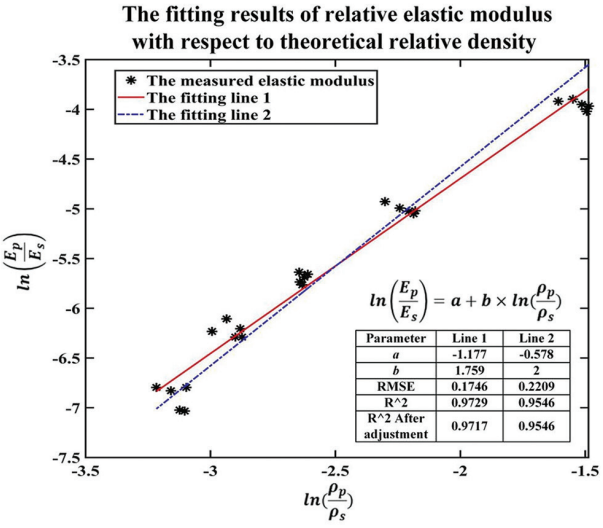

Figure 12. Fitting results of the compression modulus with respect to theoretical relative density for the Schwarz-P structures using the Gibson-Ashby model.

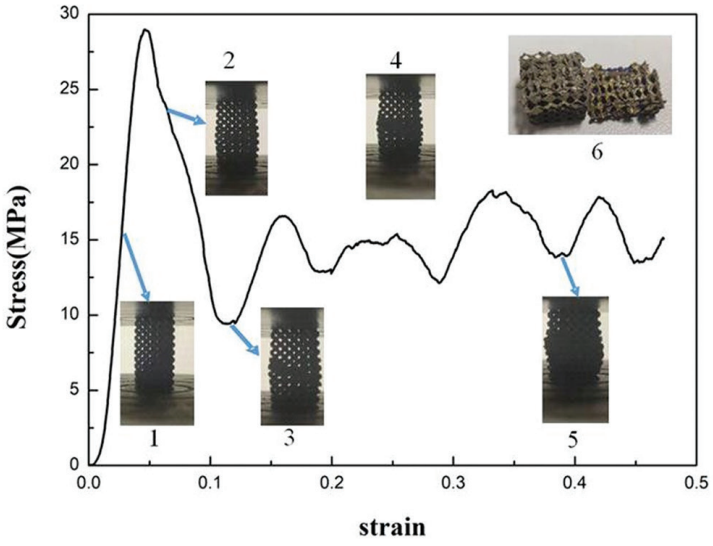

Figure 13. Deformation process of the Schwarz-P structure: sample B0.8.

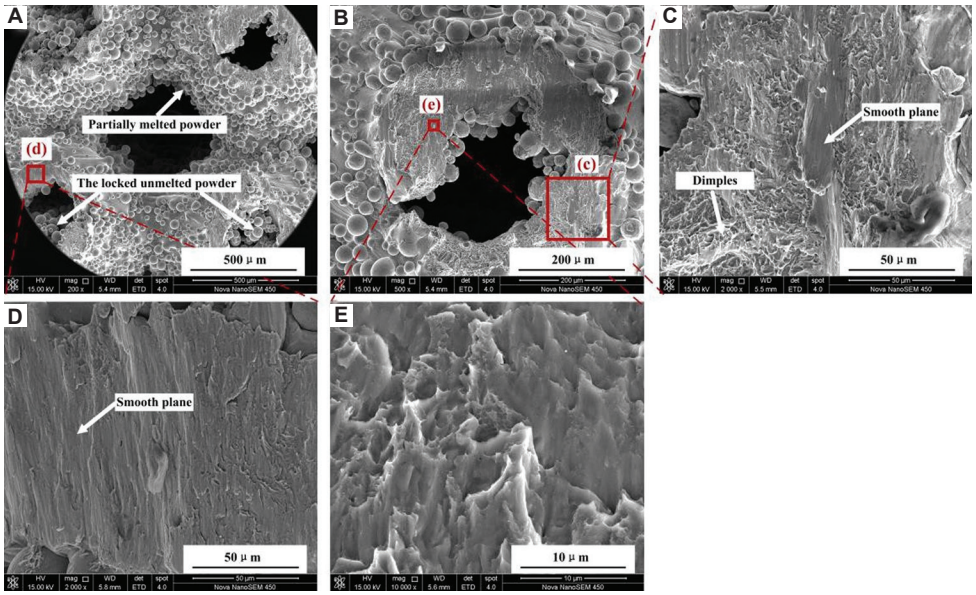

Figure 14. Fracture surface morphology of Schwarz-P structure: sample A0.6. (A) fracture macro-surface at a low magnification of ×200. (B), (C), (D), and (E) show the fracture micro-surface at high magnification of ×500, ×2000, ×2000, and ×10000, respectively.

$$\ln\left(\frac{E_p}{E_s}\right)=\ln\left(C_1\right)+n_1\times\ln\left(\frac{\rho_p}{\rho_s}\right) \quad \text{(V)}$$

$$\ln\left(\frac{E_p}{E_s}\right)=\ln\left(C_1\right)+2\ln\left(\frac{\rho_p}{\rho_s}\right) \quad \text{(VI)}$$

3.4. Compression failure mechanism

To investigate the failure mechanism of the Schwarz-P structures, the crushing behavior of the samples was recorded, and a typical sample B0.8 was chosen to explain the results. The results are shown in Figure 13. In general, the compression process had three stages:

(i) Initial elastic stage. During this stage, as the compression displacement increased, the compressive stress increased rapidly until it reached the maximum value, but the strain changed slowly. The compressive strain and stress thus exhibited a linear relationship.

(ii) Plastic plateau stage. During this stage, a localized bulging phenomenon began to occur in the middle region of the Schwarz-P structure (as shown in Figure 13, point 2). With further increases in the

compressive load, shear failure occurred at an incline angle of approximately 30° between the shear cracking propagation path and the compressive loading direction (as shown in Figure 13, points 3 – 5).

(iii) Densification stage. Unfortunately, the samples slipped and fractured, and thus loading was not continued. Figure 13, point 6, presents the final fractured Schwarz-P structure. Figure 14 shows the morphologies of the fracture surface of sample A0.6 after the static compression test. Some partially melted powder particles are attached to the surface and some unmelted powder particles are locked in the cavities. The fractured surface consists of a mixture of smooth planes and micro-sized dimples, thus exhibiting a mixed ductile and brittle failure mode.

4. Conclusions

In this study, Schwarz-P cellular structures with unit sizes ranging from 1 mm to 5 mm and shape control factors ranging from 0 to 0.8 obtained using a toolpath-based construction design were fabricated by LPBF using Ti6Al4V powder. The macrostructure, microstructure, and compression performance of these structures were investigated. The main findings are summarized as follows:

(i) The size of the open pores decreased as the shape control factor increased and increased as the unit size increased, which is consistent with the designs. However, when the unit size was 1 mm and the shape control factor was >0.4, the open pores became closed cavities, locking in unmelted powder particles. Similar to the conventional design, partially melted powder particles attached to the surface of the Schwarz-P structures were found.

(ii) Except for structures with closed cavities, the relative densities of the Schwarz-P structures calculated using the toolpath and the melt track width were consistent with the measured values. When excluding the influence of unmelted and partially melted powder particles, the calculated relative density was more suitable for the prediction of mechanical properties.

(iii) The EBSD maps indicated that the original β grains and acicular α' phase within each β grain together constituted the microstructure of the Ti6Al4V Schwarz-P structure, as reported in the literature; however, the original β grains in this study were smaller, and the orientation of the original β grains in the side surface was irregular.

(iv) The relative elastic modulus of the Schwarz-P structure can be expressed by the Gibson-Ashby model as a function of the theoretical relative density ρ_p/ρ_s: $E_p/E_s = 0.31(\rho_p/\rho_s)^{1.76}$. In addition, the fractured surface consisted of a mixture of smooth planes and micro-sized dimples, exhibiting a mixed ductile and brittle failure mode.

Acknowledgments

The authors would like to express their sincere appreciation to Mr. He Junjie, PhD candidate, from Tokyo University of Agriculture and Technology for his support on the analysis of the microstructure.

Funding

None.

Conflict of interest

The authors declare that they have no known competing financial interests or personal relationships that could have appeared to influence the work reported in this paper.

Author contributions

Conceptualization: Shujie Tan, Yicha Zhang
Formal analysis: Ziyu Wang
Funding acquisition: Liping Ding
Investigation: Shujie Tan, Xi Zhang
Methodology: Shujie Tan, Liping Ding, Yicha Zhang
Project administration: Wenliang Chen
Visualization: Xi Zhang
Writing – original draft: Shujie Tan, Xi Zhang
Writing – review & editing: Yicha Zhang

References

1. Maconachie T, Leary M, Lozanovski B, *et al*., 2019, SLM lattice structures: Properties, performance, applications and challenges. *Mater Design*, 183: 108137.

https://doi.org/10.1016/j.matdes.2019.108137

2. McGregor M, Patel S, McLachlin S, *et al*., 2021, Architectural bone parameters and the relationship to titanium lattice design for powder bed fusion additive manufacturing. *Addit Manuf*, 47: 102273.

https://doi.org/10.1016/j.addma.2021.102273

3. Feng J, Fu J, Yao X, *et al*., 2022, Triply periodic minimal surface (TPMS) porous structures: From multi-scale design, precise additive manufacturing to multidisciplinary applications. *Int J Extrem Manuf*, 4: 022001.

4. Du Plessis A, Broeckhoven C, Yadroitsava I, *et al*., 2019, Beautiful and functional: A review of biomimetic design in additive manufacturing. *Addit Manuf*, 27: 408–427.

https://doi.org/10.1016/j.addma.2019.03.033

5. Pham MS, Liu C, Todd I, *et al*., 2019, Damage-tolerant architected materials inspired by crystal microstructure. *Nature*, 565: 305–311.

https://doi.org/10.1038/s41586-018-0850-3

6. Thompson MK, Moroni G, Vaneker T, *et al*., 2016, Design for additive manufacturing: Trends, opportunities, considerations, and constraints. *CIRP Ann Manuf Technol*, 65: 737–760.

7. Vaneker T, Bernard A, Moroni G, *et al*., 2020, Design for additive manufacturing: Framework and methodology. *CIRP Annals*, 69: 578–599.

   https://doi.org/10.1016/j.cirp.2020.05.006

8. Zhang Y, Yang S, Zhao YF, 2020, Manufacturability analysis of metal laser-based powder bed fusion additive manufacturing-a survey. *Int J Adv Manuf Technol*, 110: 57–78.

9. Shi Y, Zhang Y, Baek S, *et al*., 2018, Manufacturability analysis for additive manufacturing using a novel feature recognition technique. *Comput Aided Design Appl*, 15: 941–952.

   https://doi.org/10.1080/16864360.2018.1462574

10. Yang L, Yan C, Cao W, *et al*., 2019, Compression-compression fatigue behaviour of gyroid-type triply periodic minimal surface porous structures fabricated by selective laser melting. *Acta Mater*, 181: 49–66.

    https://doi.org/10.2139/ssrn.3406935

11. Yan X, Yue S, Ge J, *et al*., 2022, Microstructural and mechanical optimization of selective laser melted Ti6Al4V lattices: Effect of hot isostatic pressing. *J Manuf Processes*, 77: 151–162.

    https://doi.org/10.1016/j.jmapro.2022.02.024

12. Ding J, Zou Q, Qu S, *et al*., 2021, STL-free design and manufacturing paradigm for high-precision powder bed fusion. *CIRP Annals*, 70: 167–170.

    https://doi.org/10.1016/j.cirp.2021.03.012

13. Feng J, Fu J, Lin Z, *et al*., 2019, Layered infill area generation from triply periodic minimal surfaces for additive manufacturing. *Comput Aided Design*, 107: 50–63.

    https://doi.org/10.1016/j.cad.2018.09.005

14. Feng J, Fu J, Shang C, *et al*., 2020, Efficient generation strategy for hierarchical porous scaffolds with freeform external geometries. *Addit Manuf*, 31: 100943.

    https://doi.org/10.1016/j.addma.2019.100943

15. Ding L, Tan S, Chen W, *et al*., 2021, Manufacturability analysis of extremely fine porous structures for selective laser melting process of Ti6Al4V alloy. *Rapid Prototyp J*, 27: 1523–1537.

    https://doi.org/10.1108/RPJ-11-2020-0280

16. Ding L, Tan S, Chen W, *et al*., 2022, Development of a manufacturability predictor for periodic cellular structures in a selective laser melting process via experiment and ANN modelling. *Virtual Phys Prototyp*, 17: 948–965.

    https://doi.org/10.1080/17452759.2022.2091461

17. Yan C, Hao L, Hussein A, *et al*., 2012, Evaluations of cellular lattice structures manufactured using selective laser melting. *Int J Mach Tools Manuf*, 62: 32–38.

    https://doi.org/10.1016/j.ijmachtools.2012.06.002

18. Yan C, Hao L, Hussein A, *et al*., 2014, Advanced lightweight 316L stainless steel cellular lattice structures fabricated via selective laser melting. *Mater Design*, 55: 533–541.

    https://doi.org/10.1016/j.matdes.2013.10.027

19. Neikter M, Huang A, Wu X, 2019, Microstructural characterization of binary microstructure pattern in selective laser-melted Ti-6Al-4V. *Int J Adv Manuf Technol*, 104: 1381–1391.

20. Zhang Y, Tan S, Ding L, *et al*., 2021, A toolpath-based layer construction method for designing & printing porous structure. *CIRP Annals*, 70: 123–126.

    https://doi.org/10.1016/j.cirp.2021.04.020

21. Tan S, Zhang X, Ding L, *et al*., 2021, An Efficient Layer Construction Method to Generate Accurate Printing Toolpaths of Periodic Cellular Structures for Selective Laser Melting Process Solid Freeform Fabrication 2021. In: *Proceedings of the 32th Annual International Solid Freeform Fabrication Symposium*.

22. International Organization for Standardization. Mechanical Testing of Metals-Ductility Testing-compression Test for Porous and Cellular Metals. Geneva: International Organization for Standardization. ISO 13314-2011.

23. Ashby MF, 2006, The properties of foams and lattices. *Philos Trans A Math Phys Eng Sci*, 364: 15–30.

    https://doi.org/10.1098/rsta.2005.1678

24. Zhao X, Li S, Zhang M, *et al*., 2016, Comparison of the microstructures and mechanical properties of Ti-6Al-4V fabricated by selective laser melting and electron beam melting. *Mater Design*, 95: 21–31.

    https://doi.org/10.1016/j.matdes.2015.12.135

25. Chang C, Huang J, Yan X, *et al*., 2020, Microstructure and mechanical deformation behavior of selective laser melted Ti6Al4V ELI alloy porous structures. *Mater Lett*, 277: 128366.

    https://doi.org/10.1016/j.matlet.2020.128366

26. Vrancken B, Thijs L, Kruth JP, *et al*., 2012, Heat treatment of Ti6Al4V produced by selective laser melting: Microstructure and mechanical properties. *J Alloys Compds*, 541: 177–185.

    https://doi.org/10.1016/j.jallcom.2012.07.022

Materials Science in Additive Manufacturing

ORIGINAL RESEARCH ARTICLE

Inconel 718-CoCrMo bimetallic structures through directed energy deposition-based additive manufacturing

Cory Groden[1], Victor Champagne[2], Susmita Bose[1], Amit Bandyopadhyay[1]*

[1]W. M. Keck Biomedical Materials Research Laboratory, School of Mechanical and Materials Engineering, Washington State University Pullman, WA 99164, USA

[2]US Army Research Laboratory, Weapons and Materials Research Directorate, Aberdeen Proving Ground, MD, USA

Abstract

Bimetallic structures and coatings through additive manufacturing (AM) have demonstrated a high degree of freedom for tailoring properties depending on the application. In this study, Inconel 718 and CoCrMo were used as both are common alloys and exhibit unique properties, such as high-temperature oxidation, wear, and fatigue resistance. Using directed energy deposition-based metal AM, bimetallic structures containing these two alloys were manufactured, and the resulting structures exhibited no intermetallic phase formation, cracking, or porosity. Scanning electron microscopy and energy dispersive spectroscopy revealed a smooth elemental transition between the two compositions. Hardness testing showed a linear transition in the interfacial zone, validating no brittle intermetallic phase formation. Compression testing and fracture surface analysis revealed that the failures were not dependent on the interface properties. High-temperature oxidation showed no distinct effect on the interface, a firmly attached chromium oxide layer on the Inconel 718 side and a loosely attached chromium oxide layer on the CoCrMo side. There was also evidence of pit formation on the Inconel 718 surface, but not on the CoCrMo. These findings confirm a stable bimetallic system in which one of the two alloys can be used on the other material to improve the structure's high-temperature oxidation or wear/corrosion resistance.

Keywords: Additive manufacturing; Three-dimensional printing; Directed energy deposition; Cobalt-chromium molybdenum alloy; Inconel 718; Bimetallic structures

***Corresponding author:**
Amit Bandyopadhyay
(amitband@wsu.edu)

Citation: Groden C, Champagne V, Bose S, *et al.,* 2022, Inconel 718-CoCrMo bimetallic structures through directed energy deposition-based additive manufacturing. *Mater Sci Add Manuf*, 1(3):18. https://doi.org/10.18063/msam.v1i3.18

Received: September 1, 2022

Accepted: September 14, 2022

Published Online: September 27, 2022

Copyright: © 2022 Author(s). This is an Open Access article distributed under the terms of the Creative Commons Attribution License, permitting distribution, and reproduction in any medium, provided the original work is properly cited.

Publisher's Note: Whoice Publishing remains neutral with regard to jurisdictional claims in published maps and institutional affiliations.

1. Introduction

Advances in metal additive manufacturing (AM) technology have allowed designing multi-material structures to impart unique and site-specific properties for various applications. For example, AM-processed FeCrAl coating on a Zr alloy increased the oxidation resistance by a factor of 50[1]. It has been reported that a 30Cr15MoY alloy steel on a C45 substrate increased the corrosion resistance of neat C45 steel[2]. For strength and thermal conductivity, adding a tungsten alloy coating to Inconel 718 increased the strength and thermal conductivity compared to pure Inconel 718[3]. A GRCop84 coating on Inconel 718 increased thermal conductivity by 300% more than pure Inconel 718[4].

Finally, for increased bioactivity, AM-processed titanium (Ti)-tantalum (Ta) bimetallic structure has shown a significant improvement in biocompatibility similar to pure Ta[5]. A recent review documents many such performance enhancements through AM-processed bimetallic and multi-material structures that highlight the innovation opportunities using AM with the next-generation metallic materials[6]. The interface between the coating and the bulk material can form various intermetallic compounds, which have been shown to increase the strength of some bimetallic systems, such as Ti6Al4V/Al12Si and Ti/Ni[7,8]. However, this interfacial behavior can be detrimental in some cases, which has prompted studies to understand better and model the behavior of these bimetallic systems[9]. In addition, research has been conducted to manufacture multi-material and bimetallic systems more efficiently to be better suited for industry[10].

Inconel 718 is a nickel-based superalloy consisting of about 55% nickel (Ni), 18% chromium (Cr), 18% iron (Fe), 5% niobium (Nb), and 3% molybdenum (Mo). This alloy is used extensively in aerospace applications due to its excellent high-temperature strength, along with corrosion and oxidation resistance[11]. Inconel 718 is a standard alloy used in AM due to its excellent weldability[12]. This alloy is particularly strong for the formation of the γ' (Ni_3Ti and Ni_3Al), the γ" (cubic Ni_3Nb), and the δ (orthorhombic Ni_3Nb) phases, all of which have been observed in heat-treated Inconel 718 samples that were printed by selective laser melting (SLM)[13]. Different heat treatments can control the amount of these phases formed in Inconel 718[14-16]. This allows manufacturers to tailor the properties of Inconel 718 depending on the application and further demonstrates the versatility of this alloy. The corrosion resistance of Inconel 718 comes from the Cr and Mo, which forms a surface passivation layer limiting oxygen flow into the bulk structure. Because of microstructural and phase evolutions, corrosion resistance for Inconel 718 also depends on the manufacturing and post-processing methods used. It has been reported that excessive carbide formation during solution treatment caused Cr and Mo depletion throughout the bulk Inconel 718[17]. Oxidation resistance is typically attributed to the Cr_2O_3 film, which prevents oxygen diffusion into the bulk structure; however, a NbO film also forms at temperatures higher than 800°C to further aid oxidation resistance[18].

Cobalt-chromium molybdenum (CoCrMo) alloy consists of around 60% cobalt, 30% Cr, and 5% Mo, with 5% being other elements such as Ti. Due to its excellent wear and corrosion resistance, this alloy is used in cutting tools and other applications requiring better wear resistance, such as articulating surfaces of biomedical implants and dental crowns[19-21]. However, this alloy's high hardness and wear resistance make it very difficult to machine[22]. As a result, many studies look at the cutting force and anisotropic effects to explain how to properly machine these alloys without compromising the alloy surface or the milling tools[23,24]. The strengthening mechanism in CoCrMo alloy comes from the various carbides, such as $Co_{23}C_6$ and Cr_6C[25]. Therefore, the properties of CoCrMo alloys can be altered using different heat treatments, which results in various carbide formations[26,27]. The oxidation resistance of CoCrMo at high temperatures is not well reported; however, the alloy's carbide forming abilities and the chromium oxide layer offer good oxidation resistance.

Since CoCrMo is wear- and corrosion-resistant and Inconel 718 is high-temperature oxidation-resistant, a coating of one of these materials may prove effective in increasing the bulk and surface properties of the bimetallic structures. In cases where a strong bulk structure is needed with high oxidation resistance, Inconel 718 coating on CoCrMo would be preferred. A CoCrMo coating on Inconel 718 could be preferred in cases where superior corrosion resistance is needed. A recent study using laser powder bed fusion (L-PBF) of Inconel 718 and CoCrMo functionally graded structure exhibited low porosity and smooth composition transitions[28]; however, there is still a knowledge gap on processing-structure-properties relationships of DED-manufactured bimetallic structures of Inconel 718 and CoCrMo. Addressing this gap is the primary focus of this research. Inconel 718 and CoCrMo bimetallic structures were manufactured by DED-based AM and were subjected to various tests for microstructure and phase analysis, hardness, compression testing, and measuring high-temperature oxidation resistance. Figure 1 outlines the processing strategies for the Inconel 718 and CoCrMo bimetallic structures using DED.

2. Materials and methods

2.1. Directed energy deposition (DED) of bimetallic structures

Inconel 718 and CoCrMo bimetallic structures were manufactured using a powder-based DED printer (FormAlloy, CA). The computer uses a G-code input file derived from a computer-aided design (CAD) file containing the shape information. This G-code input file dictates the machine parameters while printing, including speed, layer thickness, laser power, powder flow rate, and shield gas flow rate, which prevents powders from melting onto the nozzle and clogging it. These alloys were printed onto 316L stainless steel substrate. Inconel 718 powder (Powder Alloy Corporation, Ohio) was used with a particle size of 50–150 μm. CoCrMo

powder (Stellite Coatings, Goshen, IN) was used with a particle size range of 50–100 μm. The bimetallic structures were optimized until the part height was close to the theoretical height. The final parameters for each sample are listed in Table 1.

2.2. Characterization of bimetallic samples

Bimetallic samples were cut in half and underwent a typical grinding or polishing procedure. The samples were then imaged using a field emission scanning electron microscope (FESEM, FEI-SIRION, Portland, OR) to determine if any defects existed at the interface. Using the energy dispersive spectroscopy (EDS; EDAX), elemental maps were obtained to examine elemental distributions at the interface. Vicker's hardness testing (Penn Tool Co, NJ) was performed along the interface and compared to the base materials' hardness. At least 15 measurements were taken for each point. For the compression tests, an Instron servohydraulic compression tester was used to determine the stress-strain curves for the longitudinal and transverse bimetallic samples and the base materials using a strain rate of 1.3 mm/min. For the oxidation tests, a muffle furnace with no other additions was used to oxidize samples for 96 h at 800°C and then underwent the same characterization process mentioned above.

3. Results

3.1. Microstructural variations

Figure 2 shows a stereoscope image of the bimetallic sample on a 316L substrate and the SEM/EDS analysis of the interface. A small but distinct interface is formed between the CoCrMo and substrate. The same can be observed between the Inconel 718 and CoCrMo junction,

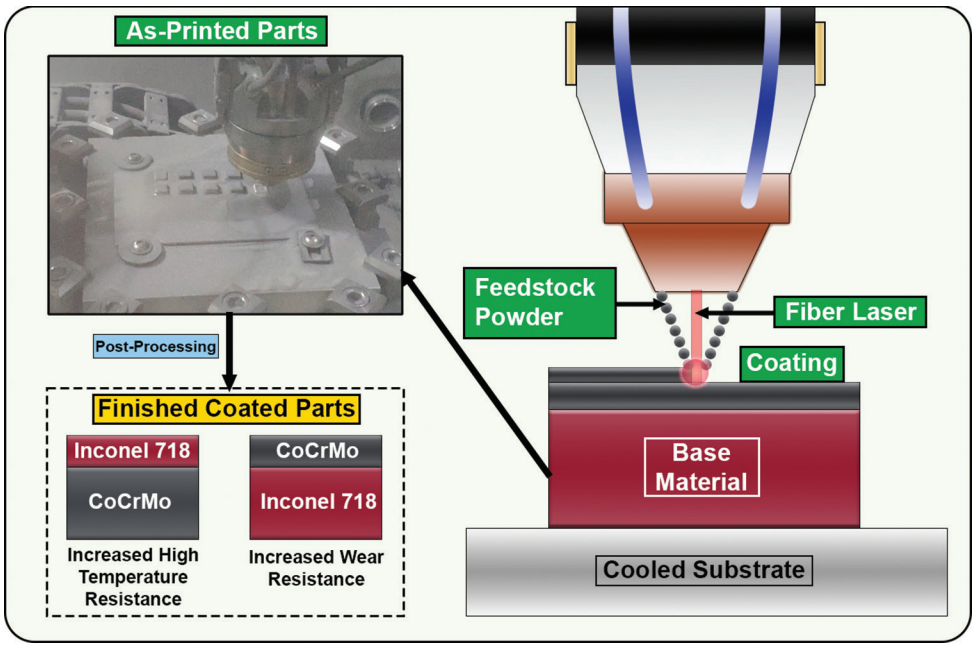

Figure 1. Processing strategies of bimetallic structures of Inconel 718-CoCrMo using laser directed energy deposition process.

Table 1. Final DED build parameters for Inconel 718, CoCrMo, and bimetallic samples

Type of sample	Inconel 718 scanning speed (mm/min)	CoCrMo scanning speed (mm/min)	Inconel 718 laser power (W)	CoCrMo laser power (W)	Inconel 718 flow rate (mm/s)	CoCrMo flow rate (m m/s)	Layer height (mm)
Oxidation and Characterization Bimetallic	1200	1600	350	350	0.5	0.6	0.1
Inconel 718 Compression	1600		350		0.5		0.1
CoCrMo Compression		600		300		0.5	0.25
Transverse Bimetallic	600	1200	300	300	0.25	0.5	0.25
Longitudinal Bimetallic	800	1200	300	300	0.3	0.5	0.2

DED: Directed energy deposition

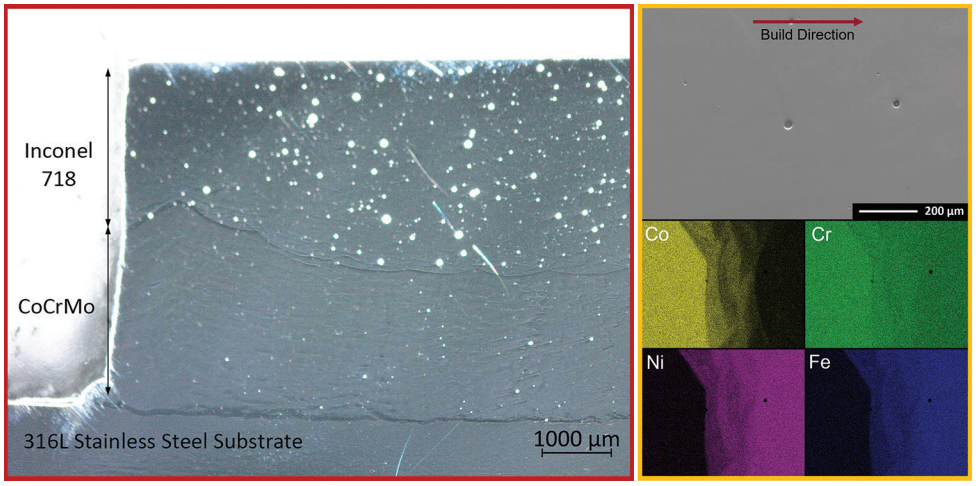

Figure 2. (Left) Inconel 718 – CoCrMo bimetallic structure. (Right) SEM/EDS analysis of the bimetallic interface. Note that the interface is not visible in the SEM micrograph, but the compositional variations mark the interface in the EDS mapping.

with the bimetallic interface appearing smaller than the substrate interface. The illuminated circles are tiny gas pores, which are more frequent and extensive in the Inconel 718 region than in the CoCrMo region. For the SEM image, a seemingly blank photo is observed with no qualitative distinction between the two materials and the interface. However, the EDS mapping indicates a relatively smooth transition between the elements, meaning there is little to no elemental segregation. No cracking or other defects are observed at the interface, which confirms that these materials are compatible[28].

3.2. Hardness

Vicker's hardness tests were conducted on polished samples and the results are shown in Figure 3. The tests show that the base hardnesses in the Inconel 718 and CoCrMo zones were about 260 HV and 430 HV, respectively. A hardness profile was established, measuring at every 50 µm distance within the interface zone until the pure alloys were reached. The profile shows a linear variation within the interface region. The linear profile confirms no brittle intermetallic phase formations and reveals that the interface is about 150 µm wide.

3.3. Compression testing

Figure 4 shows stress-strain curves for the four types of non-heat treated compression samples. The test's primary purpose was to understand the role of the interface in compressive deformation behavior. It was found that the interface properties did not limit the compressive deformation in bimetallic structures but were instead controlled by the bulk materials. The transverse bimetallic samples had the worst yield strength, with the base CoCrMo sample performing the best. The Inconel 718 samples did not fail, so the plot only displays up to 0.4 strain for that sample. The failure behavior of the two bimetallic structures is illustrated in Figure 5.

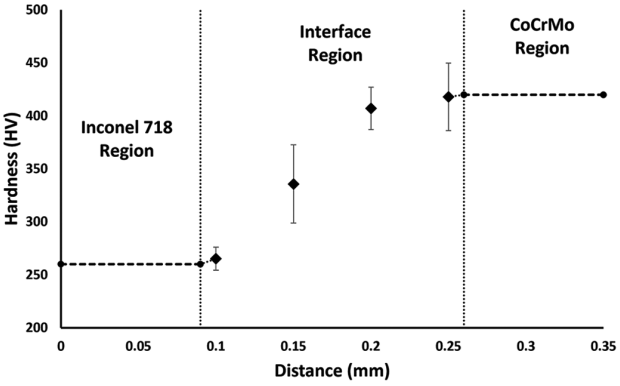

Figure 3. Vicker's hardness profile of Inconel 718-CoCrMo bimetallic structure.

3.4. Oxidation studies of bimetallic samples

For the oxidation and followed by hardness measurements, samples were tested at 800°C for 96 h. No significant variations in hardness were observed. Only a slight decrease in hardness (430 HV to 400 HV) was observed in the CoCrMo part, which occurred as a byproduct of the oxidation test since recrystallization would also occur. Figure 6 shows the SEM/EDS analysis of the oxide layer formed in each constituent. For Inconel 718, a strongly adherent chromium oxide layer was formed along with some pits. This pitting resulted from the depletion of Cr near the interface, which made the material under the oxide layer prone to the effects of oxidation. For the CoCrMo side, spalling was observed, meaning that the oxide layer was not strongly attached to the base material. Furthermore, a Cr depletion zone was not observed in the CoCrMo part.

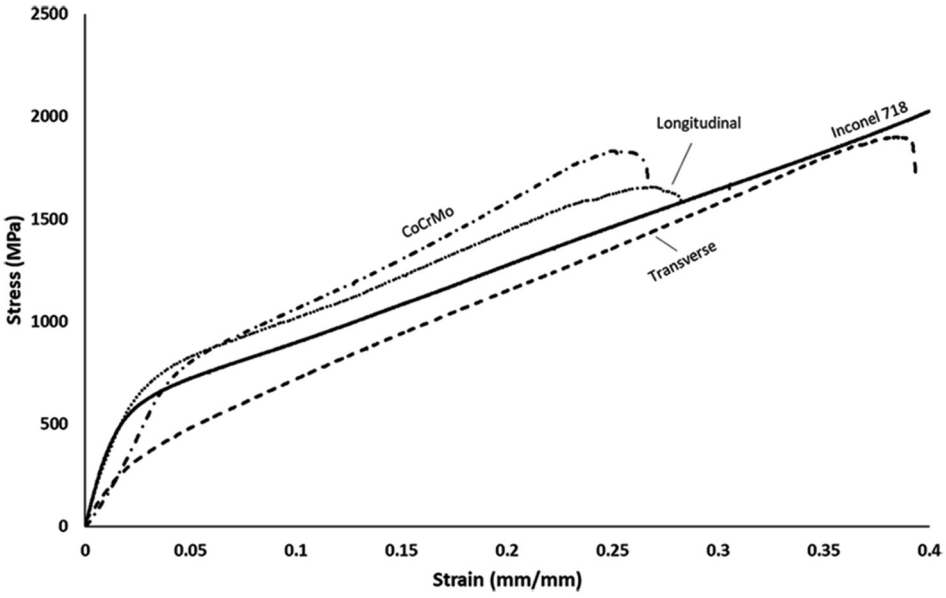

Sample	Inconel 718	CoCrMo	Transverse bimetallic	Longitudinal bimetallic
Yield strength	498±34	600±103	408±75	533±65

Figure 4. Stress-strain curves for each compression sample type. Note that only one of each sample type is shown and that the Inconel 718 base sample did not fail and therefore is only plotted until 0.4 strain.

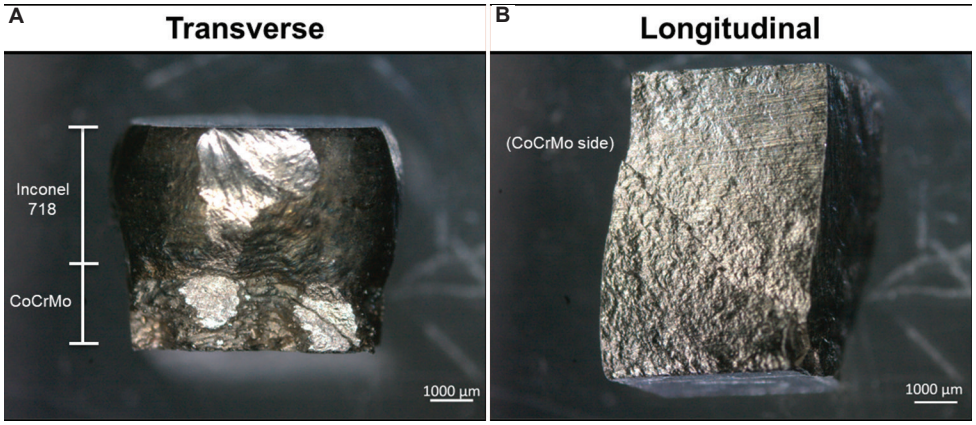

Figure 5. (A) Failure behavior of the transverse bimetallic sample. Cracking is observed in the CoCrMo part at the bottom right. **(B)** Failure behavior of the longitudinal bimetallic sample, in which there is cracking on the CoCrMo side at a 45° angle.

4. Discussion

The laser DED process is used to form bimetallic structures of Inconel 718 to CoCrMo. The results show that the Inconel 718 and CoCrMo form a stable interface. This indicates that using a coating of one or the other could tailor a structure with specific properties depending on the need, with the CoCrMo coating working better for wear and corrosion resistance applications with static conditions and with the Inconel 718 coating working better for high-temperature oxidation resistance applications with dynamic conditions. Furthermore, the microstructural findings of this study are in line with published data where functionally graded structures were printed through powder bed fusion (PBF)[28].

It is essential to discuss what coating should be used for what application. Inconel 718 coating on CoCrMo would work better in environments with dynamic conditions in high-temperature environments. This is due to the oxide layer in Inconel 718 being firmly attached, unlike

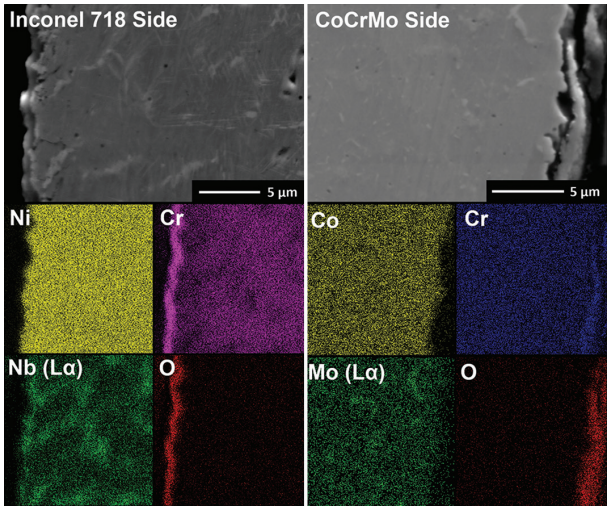

Figure 6. SEM and EDS images of the oxidation of the Inconel 718 and CoCrMo bimetallic sample. The Inconel 718 oxide layer is on the left of the micrograph, where a strongly adherent oxide layer is seen. The CoCrMo oxide layer is on the right, where spalling of the oxide layer can be seen.

the CoCrMo oxide layer. Although it was found that the CoCrMo showed less oxidation damage compared to Inconel 718, the Inconel 718 coating oxide layer would be able to resist further oxidation damage, but the coating would also be able to keep the CoCrMo oxide layer from being washed away, preventing degradation of the bulk structure. In the opposite scenario with a CoCrMo coating on Inconel 718, this structure would be best suited for corrosive environments and situations with high wear, as the corrosion and wear resistance of CoCrMo are unmatched compared to most alloys.

Wen *et al.* recently published functionally graded structures of Inconel 718 and CoCrMo printed using laser PBF[28]. In this study, we produced defect-free and low-porosity structures without any concerns related to the compatibility of the base materials. Our results also show a compatible interface between Inconel 718 and CoCrMo, even with the case of direct bimetallic transition, which is much more prone to issues arising from material incompatibility due to a sharp change in composition. The hardness of the CoCrMo part in our study compared to the FGM study differed by about 30 HV (420 HV compared to 400 HV, respectively), while the same for Inconel 718 part differed by 90 HV (360 HV compared to 270 HV). However, this difference is expected as the printing techniques are different and it is evident that different amounts of carbides formed in the FGM parts compared to the bimetallic parts due to faster cooling rates in DED. Finally, the stress-strain plots in each study showed considerable failure strain, reinforcing the notion that unwanted intermetallic phases are not a concern for these bimetallic structures.

Although oxidation kinetics are well understood for single material systems, more studies are needed to understand the oxidation resistance of coated or bimetallic systems. For single materials, the oxidation resistance can significantly vary depending on factors, such as oxide formation rate, defects, and mean free path of oxygen.[29]. The oxide layer's composition also matters significantly due to the defect density in the said oxide layer. For example, chromium oxide layers typically exhibit a very low defect density, preventing oxygen diffusion[30-32]. Material constants are typically determined experimentally by fitting a curve to the data. In the case of parabolic-type oxidation, the rate equation is given by:

$$\frac{dx}{dt} = \frac{Kp}{x}$$

Where Kp is the rate constant, and x is the scale thickness[29]. Most metallic alloys follow this parabolic behavior due to the continual formation of the oxide layer, while ceramic materials follow a more linear relationship. In the case of an alloy's thin coating, oxygen's mean free path will be significantly higher to diffuse to the bulk material under the coating. However, the constants could potentially be determined by first determining the oxidation constants for the coating, then using it as a correction curve for the coated structure. In this work, Inconel 718 coating on CoCrMo proved to be a better combination to enhance oxidation resistance of the bimetallic structure due to the strongly adherent oxide layer on Inconel 718 even after 96 h at 800°C.

5. Conclusions

Inconel 718-CoCrMo was successfully manufactured using the laser DED-based AM. No difficulty was observed in printing these structures, even during optimization, and the finished parts had low porosity without any cracking. The interface could not be distinguished using SEM imaging but was revealed in EDS mapping of elemental transitions. Hardness testing revealed a smooth yet brief transition between the two alloys. Compression testing showed that the CoCrMo had the highest yield strength of the four structures tested and determined that the compression behavior was not dependent on the bimetallic interface. Oxidation tests showed that the bimetallic interface was not affected by the high temperatures and revealed that the Inconel 718 formed a firmly attached chromium oxide layer, while the CoCrMo showed spalling of the same oxide layer.

Acknowledgments

The authors thank JCDREAM (Seattle, WA) for a capital equipment grant to purchase the directed energy deposition (DED)-based metal 3D Printer at WSU.

Funding

The authors want to acknowledge financial support from the Army Research Laboratory under grant number W911NF2020206. The views and conclusions contained in this document are those of the authors and should not be interpreted as representing the official policies, either expressed or implied, of the Army Research Laboratory or the U.S. Government. The U.S. Government is authorized to reproduce and distribute reprints for Government purposes, notwithstanding any copyright notation herein.

Conflict of interest

The authors declare no conflicts of interest.

Author contributions

Conceptualization: Victor Champagne, Amit Bandyopadhyay
Data curation: Cory Groden
Funding acquisition: Susmita Bose, Amit Bandyopadhyay
Investigation: Cory Groden
Supervision: Susmita Bose, Amit Bandyopadhyay
Writing – original draft: Cory Groden
Writing – review & editing: Victor Champagne, Susmita Bose, Amit Bandyopadhyay

References

1. Kim IH, Jung YI, Kim HG, *et al*., 2021, Oxidation-resistant coating of FeCrAl on Zr-alloy tubes using 3D printing direct energy deposition. *Surf Coat Technol*, 411: 126915.

   https://doi.org/10.1016/j.surfcoat.2021.126915

2. Shang F, Chen S, Zhou L, *et al*., 2021, Effect of laser energy volume density on wear resistance and corrosion resistance of 30Cr15MoY alloy steel coating prepared by laser direct metal deposition. *Surf Coat Technol*, 421: 127382.

   https://doi.org/10.1016/j.surfcoat.2021.127382

3. Groden C, Traxel KD, Afrouzian A, *et al*., 2022, Inconel 718-W7Ni3Fe bimetallic structures using directed energy deposition-based additive manufacturing. *Virtual Phys Prototyp* 17: 170–180.

   https://doi.org/10.1080/17452759.2022.2025673

4. Onuike B, Heer B, Bandyopadhyay A, 2018, Additive manufacturing of inconel 718-copper alloy bimetallic structure using laser engineered net shaping (LENS™). *Addit Manuf*, 21: 133–140.

   https://doi.org/10.1016/j.addma.2018.02.007

5. Traxel KD, Bandyopadhyay A, 2021, Modeling and experimental validation of additively manufactured tantalum-titanium bimetallic interfaces. *Mater Des*, 207: 109793.

   https://doi.org/10.1016/j.matdes.2021.109793

6. Bandyopadhyay A, Zhang Y, Onuike B, 2022, Additive manufacturing of bimetallic structures. *Virtual Phys Prototyp*, 17: 256–294.

   https://doi.org/10.1080/17452759.2022.2040738

7. Zhang Y, Bandyopadhyay A, 2019, Direct fabrication of bimetallic Ti6Al4V+Al12Si structures via additive manufacturing. *Addit Manuf*, 29: 100783.

   https://doi.org/10.1016/j.addma.2019.100783

8. Afrouzian A, Groden CJ, Field DP, *et al*., 2022, Additive manufacturing of Ti-Ni bimetallic structures. *Mater Des*, 215: 110461.

   https://doi.org/10.1016/j.matdes.2022.110461

9. Yao L, Huang S, Ramamurty U, *et al*., 2021, On the formation of "Fish-Scale" morphology with curved grain interfacial microstructures during selective laser melting of dissimilar alloys. *Acta Mater*, 220: 117331.

   https://doi.org/10.1016/j.actamat.2021.117331

10. Sing SL, Huang S, Goh GD, *et al*., 2021, Emerging metallic systems for additive manufacturing: *In-situ* alloying and multi-metal processing in laser powder bed fusion. *Prog Mater Sci*, 119: 100795.

    https://doi.org/10.1016/j.pmatsci.2021.100795

11. Wang Z, Wang J, Xu S, *et al*., 2022, Influence of powder characteristics on microstructure and mechanical properties of inconel 718 superalloy manufactured by direct energy deposition. *Appl Surf Sci*, 583: 152545.

    https://doi.org/10.1016/j.apsusc.2022.152545

12. Hosseini E, Popovich VA, 2019, A review of mechanical properties of additively manufactured inconel 718. *Addit Manuf*, 30: 100877.

    https://doi.org/10.1016/j.addma.2019.100877

13. Cao GH, Sun TY, Wang CH, *et al*., 2018, Investigations of Γ', Γ'' and δ precipitates in heat-treated inconel 718 alloy fabricated by selective laser melting. *Mater Charact*, 136: 398–406.

    https://doi.org/10.1016/j.matchar.2018.01.006

14. Wan HY, Zhou ZJ, Li CP, *et al*., 2018, Enhancing fatigue strength of selective laser melting-fabricated inconel 718 by tailoring heat treatment route. *Adv Eng Mater* 20: 1800307.

    https://doi.org/10.1002/adem.201800307

15. Ling LS, Yin Z, Hu Z, *et al*., 2019, Effects of the Γ''-Ni(3)Nb phase on mechanical properties of inconel 718 superalloys with different heat treatments. *Materials* (*Basel, Switzerland*), 13: 151.

    https://doi.org/10.3390/ma13010151

16. Teixeira Ó, Silva FJ, Atzeni E, 2021, Residual stresses and heat treatments of inconel 718 parts manufactured via metal laser beam powder bed fusion: An overview. *Int J Adv Manuf*

Technol, 113: 3139–3162.

https://doi.org/10.1007/s00170-021-06835-8

17. Zhang B, Xiu M, Tan YT, *et al*., 2019, Pitting corrosion of SLM inconel 718 sample under surface and heat treatments. *Appl Surf Sci*, 490: 556–567.

https://doi.org/10.1016/j.apsusc.2019.06.043

18. Li L, Gong X, Ye X, *et al*., 2018, Influence of building direction on the oxidation behavior of inconel 718 alloy fabricated by additive manufacture of electron beam melting. *Materials* (*Basel*), 11: 2549.

https://doi.org/10.3390/ma11122549

19. Hedberg YS, Qian B, Shen Z, *et al*., 2014, *In vitro* biocompatibility of CoCrMo dental alloys fabricated by selective laser melting. *Dent Mater*, 30: 525–534.

https://doi.org/10.1016/j.dental.2014.02.008

20. Wang Q, Parry M, Masri BA, *et al*., 2017, Failure mechanisms in CoCrMo modular femoral stems for revision total hip arthroplasty. *J Biomedl Mater Res B Appl Biomater*, 105: 1525–1535.

https://doi.org/10.1002/jbm.b.33693

21. Mantrala KM, Das M, Balla VK, *et al*., 2014, Laser-deposited CoCrMo alloy: Microstructure, wear, and electrochemical properties. *J Mater Res*, 29: 2021–2027.

https://doi.org/10.1557/jmr.2014.163

22. Girão DC, Béreš M, Jardini AL, *et al*., 2020, An assessment of biomedical CoCrMo alloy fabricated by direct metal laser sintering technique for implant applications. *Mater Sci Eng C*, 107: 110305.

https://doi.org/10.1016/j.msec.2019.110305

23. Dijmarescu MR, Popovici TD, Tarba IC, *et al*., 2018, An experimental study on cutting forces when machining a CoCrMo alloy. *IOP Conf Mater Sci Eng*, 400: 022019.

https://doi.org/10.1088/1757-899X/400/2/022019

24. Fernandez-Zelaia P, Nguyen V, Zhang H, *et al*., 2019, The effects of material anisotropy on secondary processing of additively manufactured CoCrMo. *Addit Manuf*, 29: 100764.

https://doi.org/10.1016/j.addma.2019.06.015

25. Bettini E, Eriksson T, Boström M, *et al*., 2011, Influence of metal carbides on dissolution behavior of biomedical CoCrMo alloy: SEM, TEM and AFM studies. *Electrochim Acta*, 56: 9413–9419.

https://doi.org/10.1016/j.electacta.2011.08.028

26. Bawane KK, Srinivasan D, Banerjee D, 2018, Microstructural evolution and mechanical properties of direct metal laser-sintered (DMLS) CoCrMo after heat treatment. *Metallurgical Mater Trans A*, 49: 3793–3811.

https://doi.org/10.1007/s11661-018-4771-4

27. Cornacchia G, Cecchel S, Battini D, *et al*., 2022, Microstructural, mechanical, and tribological characterization of selective laser melted CoCrMo alloy under different heat treatment conditions and hot isostatic pressing. *Adv Eng Mater*, 24: 2100928.

https://doi.org/10.1002/adem.202100928

28. Wen Y, Zhang B, Narayan RL, *et al*., 2021, Laser powder bed fusion of compositionally graded CoCrMo-inconel 718. *Addit Manuf*, 40: 101926.

https://doi.org/10.1016/j.addma.2021.101926

29. Khanna AS, 2018, High-temperature oxidation. In: Kutz M, editor. Handbook of Environmental Degradation of Materials. 3rd ed., Ch. 6. William Andrew Publishing, Norwich, NY, p117–132.

https://doi.org/10.1016/B978-0-323-52472-8.00006-X

30. Oje AM, Ogwu AA, 2017, Chromium oxide coatings with the potential for eliminating the risk of chromium ion release in orthopaedic implants. *R Soc Open Sci*, 4: 170218.

https://doi.org/10.1098/rsos.170218

31. Tsai SC, Huntz AM, Dolin C, 1996, Growth mechanism of Cr2O3 scales: Oxygen and chromium diffusion, oxidation kinetics and effect of yttrium. *Mater Sci Eng A*, 212: 6–13.

https://doi.org/10.1016/0921-5093(96)10173-8

32. Mayrhofer PH, Rachbauer R, Holec D, *et al*., 2014, 4.14-protective transition metal nitride coatings. In: Hashmi S, Editor-in-Chief. Comprehensive Materials Processing. Elsevier, Oxford, p355–388.

https://doi.org/10.1016/B978-0-08-096532-1.00423-4

Materials Science in Additive Manufacturing

ORIGINAL RESEARCH ARTICLE

Advanced software development of 2D and 3D model visualization for TwinPrint, a dual-arm 3D bioprinting system for multi-material printing

Shaddin AlZaid[1], Noofa Hammad[1], Hamed I. Albalawi[1,2], Zainab N. Khan[1], Eter Othman[1,2], Charlotte A. E. Hauser[1,2]*

[1]Laboratory for Nanomedicine, Division of Biological and Environmental Science and Engineering, King Abdullah University for Science and Technology, Thuwal 23955-6900, Saudi Arabia

[2]Computational Bioscience Research Center, King Abdullah University of Science and Technology, Thuwal 23955, Saudi Arabia

Abstract

This research highlights the development of a two-dimensional (2D) and three-dimensional (3D) preview software for additive manufacturing (AM). The presented software can produce a virtual representation of an actuator's path movements by reading and parsing the orders of the desired geometric code (G-code) file. It then simulates the coded sections into separate 2D layers and colored 3D objects in a graphical model. This allows users to validate the shapes before the 3D printing process. G-code is an operation language which is based on command lines of code written in an alphanumeric format. Each line of these commands controls one machining operation; this instructs the machine's motion to move in an arc, a circle, or a straight line to perform a specific shape after compiling all code lines. AM technology is widely used in most manufacturing fields (e.g., medical, chemical, and research laboratories) as a prototyping technology due to its ability to produce rapid prototyping models. 3D printing creates physical 3D models by extruding material layer by layer as 2D layers. At present, the most critical challenges in AM technology are drastically reducing prototyping materials' consumption and time spent. To address these challenges, the proposed software allows for visualization of G-code files and predicting the overall layers' shapes, allowing both structure prediction and subsequent printing error reduction.

Keywords: Geometric code preview; Three-dimensional preview; Geometric code simulator; Three-dimensional printing

***Corresponding author:**
Charlotte A. E. Hauser
(charlotte.hauser@kaust.edu.sa)

Citation: AlZaid S, Hammad N, Albalawi HI, *et al.*, 2022, Advanced software development of 2D and 3D model visualization for TwinPrint, a dual-arm 3D bioprinting system for multi-material printing. *Mater Sci Add Manuf,* 1(3):19.
https://doi.org/10.18063/msam.v1i3.19

Received: September 9, 2022

Accepted: September 21, 2022

Published Online: September 28, 2022

Copyright: © 2022 Author(s). This is an Open Access article distributed under the terms of the Creative Commons Attribution License, permitting distribution, and reproduction in any medium, provided the original work is properly cited.

Publisher's Note: Whoice Publishing remains neutral with regard to jurisdictional claims in published maps and institutional affiliations.

1. Introduction

Three-dimensional (3D) bioprinting is an additive manufacturing (AM) technology used in regenerative medicine and tissue engineering. This technique can overcome the limitations of traditional tissue replacement methods, autografts, and allografts as they often suffer from issues related to disease transmission as well as their scarcity[1]. Aside from the heterogeneous nature of native tissues, they are made of various biomolecules, different cell types, and other biomaterials; this necessitates using multiple bioinks simultaneously or sequentially to 3D print biomimetic tissues[2]. Compared with other

fabrication methods, 3D bioprinting methods that use multiple materials enable the fabrication of customized and complex tissues and organs, which facilitates the use of this technology in clinical and pharmaceutical applications[3]. According to Liu *et al.*, the spatial locations and arrangement of biocomponents in the printed constructs are highly critical to achieve functional tissues[4]. Customized computer-aided design (CAD) and 3D bioprinting give an additional advantage when used with cell-laden biomaterials, allowing for better control of the distribution of cells and biomolecules in 3D printed constructs[3]. A comprehensive review paper by Kim *et al.* discusses the various 3D bioprinting techniques in general (i.e., using a single extruded material) as well as with multiple extruded materials[3]. In addition, it shares the perspectives and future directions for developing state-of-the-art techniques of multi-material 3D bioprinting.

There are currently three broad categories, in which 3D printing techniques find themselves in: material extrusion, material jetting, and VAT polymerization[5]. As of today, extrusion-based printing is the most commonly used printing technique. Its process of usage includes the loading of biomaterials into their respective cartilages and their subsequent extrusions from a nozzle using either mechanical or pressure-based forces. Since the nozzle is held above and moved along a predetermined platform, its motion allows the user to print a 3D object visualized by a viewing program on a connected computer. Some advantages of this technique include the ability to extrude bioinks laden with high cell density counts (hence their popularity in 3D cell culturing protocols), the capacity to lay those cells in specific areas within the overall 3D structure during its creation, as well as the relative cost efficiency of this technique as far as its customizability is concerned[6].

Material jetting is another procedure in which bioprinted objects can be made, with inkjet techniques being widely used. Considered one of the earliest established bioprinting processes, this method includes a downstream droplet ejection induced by a volumetric change upstream of the nozzle[7]. The formation of the droplet is most commonly generated through piezo-electric or thermally induced bubbles. For more in-depth information, refer to other papers[8-10]. Some of the pros associated with this technique are attributed to its high printing speeds, low costs, and its contactless nature (thus avoiding contamination issues). Unfortunately, since the viscosity of the bioink cannot be above a certain value, inks laden with a high volume of cells cannot be utilized in the creation of the 3D object[6]. As such, this method, as opposed to the aforementioned extrusion-based bioprinting procedure, is not optimal for printing biologically included structures.

The last in the umbrella of 3D printing techniques is dubbed VAT polymerization. Under it falls a number of categories including stereolithography (SLA) and digital light processing (DLP)[5]. In both these technologies, a photo-initiated liquid material is solidified using a laser. To produce the overall 3D printed structure, the liquid is set against a platform which is raised after each layer of liquid is solidified by the laser[11]. The difference between SLA and DLP, however, is that the former shines the laser at specific areas to produce the layers. In contrast, DLP instead shines the laser throughout the entire area and is only selective due to a mask between the laser and liquid. The downside associated with both these techniques, unfortunately, is the inability to include cells during the printing process[11]. As such, other following protocols are needed to seed the cells in their intended locations.

One example of a bioprinter was illustrated by Liu *et al.* in which he designed a multi-material extrusion bioprinting platform that can accurately extrude and switch between several bioinks continuously and rapidly for fast complex tissue fabrication[4]. Another 3D printing device is illustrated in the research study by Miri *et al.*, within which the development of a microfluidic device that can also rapidly switch between different hydrogel bioinks while maintaining high spatial resolution is elucidated[12]. Interestingly, Ng *et al.* addressed the potential and advantages of adopting deep learning techniques into the 3D printing process; this was done in the intention of fabricating better biomimetic patient-specific tissues/organs[13]. Similarly, An *et al.* highlighted the benefits of utilizing machine learning and digital twin of human tissues to mimic the 3D printing process and maximize the bioprinting efficiency and usage of biomaterials[14].

In the standard 3D printing process, a geometric code (G-code) file (acquired from a slicer software) gives the directional map in terms of the desired 3D model's XYZ planes to the 3D printing software. In other words, the G-code file contains the geometrical description of a 3D model that allows the instruction of the 3D printer in its printing in a layer-by-layer fashion[15]. If the G-code holds any syntax or semantic errors, the 3D model might not be correctively 3D printed[16]. One way to detect G-code errors is by viewing and/or simulating its attributed 3D model based on its code; such a program is called a G-code visualizer/simulator[16]. There are already plenty of 3D printing software programs with the features of viewing the 3D model and simulating the 3D printing process; one instance of this is the Repetier-Host Software. Another example of this was by Ueng *et al.*, in which a preview system for 3D printing was developed that utilizes G-code and some graphic techniques to efficiently display

the exterior and interior structure of a 3D model before printing[16]. Similarly, in the research paper by Gahbiche *et al.*, script is built to implement the G-code commands into the finite element software; this is used to control the movements of the tool during the simulation of the sheet formation processes[17].

Over the past years, we have developed an integrated 3D bioprinting system, consisting of a robotic arm and microfluidic pumps, and have been utilizing it to 3D print biological constructs. One application was using the system with a peptide-based material inside 3D printed support molds[18,19]. Later, the system was extended to be a dual-arm printing system, called TwinPrint that controls two 3D bioprinting sets of printing arms. The motivation behind building the TwinPrint Software was to have a single software operating bioprinting devices of different structures. TwinPrint eases the tedious aspect of the printing process that deals with the usage of multiple software to control each device in a bioprinting set. For more information on TwinPrint, refer to this paper[20]. Nonetheless, the TwinPrint Software lacks a 3D model previewer, which is crucial to check G-code errors and model corrections. In the CoraPrint method that we developed for coral restoration purposes, coral skeletons were 3D printed for the coral fragments to host[21]. The asymmetrical shape of the coral adds to the complications 3D bioprinting provides, thus exemplifying this software's handiness in viewing the shapes. For this purpose, this paper proposes a 2D and 3D G-code preview software to be integrated within the TwinPrint System. The developed preview software displays the formation of the layers involved in developing the selected 3D model, layer by layer, and piles them up to form their collective 3D model.

The remainder of the paper is organized as follows: in section 2, the methodology shares how the G-code previewer software was built, starting from the procurement of the G-code to the development of the graphical user interface (GUI); in section 3, the preview software's results (which are obtained from several G-codes' 3D models) are presented alongside in-depth analyses and discussions; and finally, section 4 provides a brief summary of the work and concludes the paper.

2. Methods

The visualization software was developed to preview 3D models before they were passed over to the computer numerical control machine. This allows for visualizing the G-code text file, which contains codified movement instructions for the tool path. However, unlike a simulator which shows the exact movement of the printer in the process of fabricating the intended object layer by layer, a viewer simply shows the path of the layers of which the objects are created (i.e., there is no movement shown, simply arrows). Nonetheless, these movement commands are essential for plotting 2D and 3D objects. Previewing the 3D model before printing is crucial as it is one way to check if the loaded G-code file is of the desired model. Moreover, errors in the G-code file can be detected when viewing the 3D model. Consequently, this increases the efficiency of printing by either reducing printing errors or avoiding printing of improper shapes, saving the user both time and materials.

2.1. G-code procurement

Initially, the 3D digital model images were obtained from scanning physical objects. A CAD software, SolidWorks, was then used to re-engineer the scanned models and export them as STL files. The STL files were then transferred to a slicing software (e.g., Slic3r) to slice the 3D virtual model and from there a G-code file was provided for the given model. The G-code file was then fed to the printing software to preview and print the 3D construct. The overall process needed to 3D print using a G-code is summarized in Figure 1.

2.2. G-code parsing and coordinate calculations

A G-code parsing script was created to read the information inside the uploaded G-code file line by line. The script

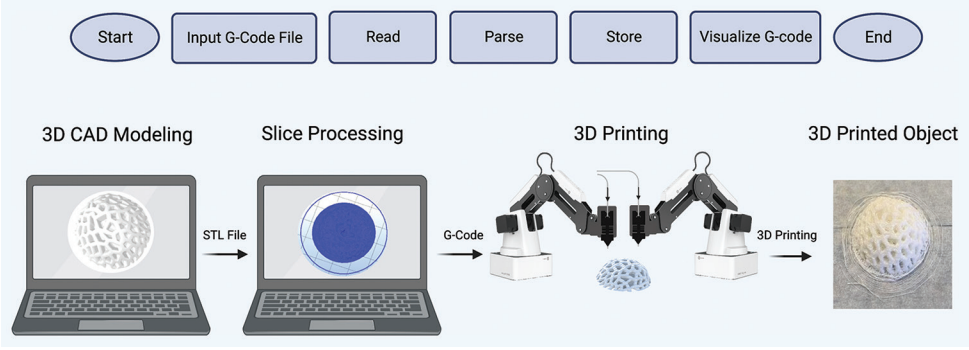

Figure 1. An overview of the three-dimensional printing process using the geometric code software.

extracts the information from the lines that contain Cartesian coordinates (X, Y, and Z) and stores this information in a file. In simple terms, if X, Y, and/or Z letters exist in a G-code line, the program extracts those lines alongside the G commands that specify the type of movement mentioned (e.g., linear or circular) and then determines whether positioning is absolute or relative. The positioning type determines how the Cartesian coordinates of the 3D construct are calculated. In case of absolute positioning, the XYZ values are specific coordinates and stored as they are. However, in relative positioning, the XYZ values of a line are added to corresponding XYZ of the previous line. Sometimes a G-code line might not have coordinate information for all XYZ; in this case, the values of the missing coordinates in a line are copied from the previous stored line information.

2.3. From G-code to visualization

The calculated XYZ coordinates and movement types were retrieved from either a.txt or.xlsx file to begin the translation process from written text lines into a 3D visualized model. The stored information represents the 3D trajectory points that form the path of the cross-section of the sliced surfaces. The sweep lines along the axes and generates the object's outer boundaries. The file is read sequentially, line by line, and an instantaneous conversion from a line to a visualized layer results in the high precision of the plotted shapes. The visualization was made using Scientific Graphics and GUI Library for Python (PyQtGraph) [22], and inspired by codes from these sources[23-25].

2.4. Software development

All the scripts and coding files used for the development of the 2D or 3D G-code preview software were written in Python Programming Language. This is also the same language used to build the TwinPrint System.

3. Results and discussion

The GUI of our program, as shown in Figure 2**,** has two main partitioned sections. The first section is used for previewing the 2D representation of the model and is shown singularly layer by layer through a white background and black lines, enabling a clear view; this can be seen in Figure 2A, 2C and 2E. The second section, likewise, shows a 3D preview by transferring the code line into path shapes as stated earlier, and shown in Figure 2B, 2D and 2F. The black lines, shown in Figure 2A and B**,** preview the shapes of the shell exteriors at those layers; they can be thought of as "the lines to be colored into" in the 3D viewing tab. Further detail of the 3D shape of the model (e.g., infills) can be seen as the "colored in" areas within the previewed 3D section (e.g., in Figure 2F). This illustration of detail represents the utility of a viewing program since shells

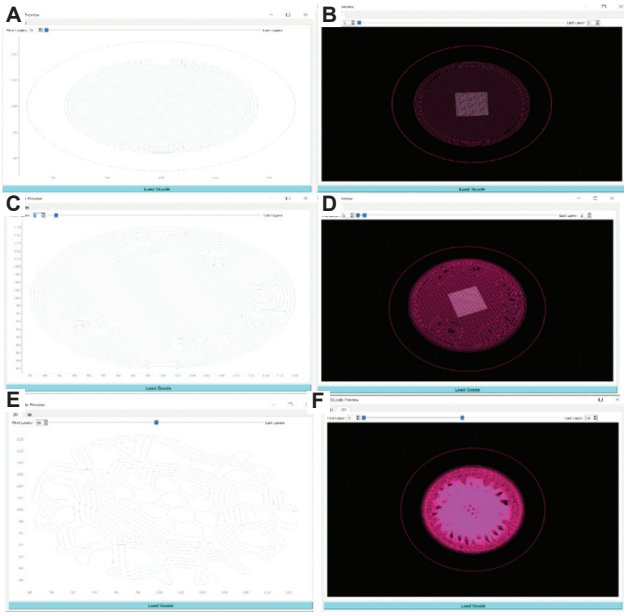

Figure 2. (A-F) Overview of graphical user interface for the two-dimensional and three-dimensional visualization sections.

remark on a model's rigidity, while infills take note of its stability, both factors of which are of high importance in 3D printing modules.

Another feature the software provides is an interactive interface with a dynamic graphics view. This interface allows the user to zoom in and out of the model, as well as to rotate around to observe different perspectives. The software also allows the isolation of specific layers to evaluate the initiating and finalizing paths (Figure 3A, 3C, and 3E) in addition to a scalable increase of layers for a path-centered view of the 3D object (Figure 3B, 3D and 3F). This comes with the ability to customize size, type, and color of the path lines. For ease of view, the user can also modify the background colors by selecting one of the two offered options. Axis labels can also be set for better navigation. Furthermore, the software is capable of visualizing 3D models with various structural complexities, ranging from very simple constructs (composed of straight lines and circles, e.g., Figure 2C) to irregular and curved structures (e. g., Figure 2D).

Another aspect accessible by plotting any given G-code's data is its capability of interactivity. In other words, such viewing measures allow the user to rotate and zoom the model and get closer looks at specific layers within it; such accessibility is shown in Figure 4.

Coupling the accessibility of viewing in the third dimension with the ability for line customization (e.g., size, type, and color) facilitates the preview of not only

single layers within the model but multiple as well. This feature is supplemented through the addition of intensifying color vibrancy as an indicator for increasing layer totals. In simpler terms, the more or brighter the colors, the more layers present in that model's area. This is illustrated in Figure 5, where colorful areas are denser with extruded materials than their less colorful counterparts (Figure 5A and 5B).

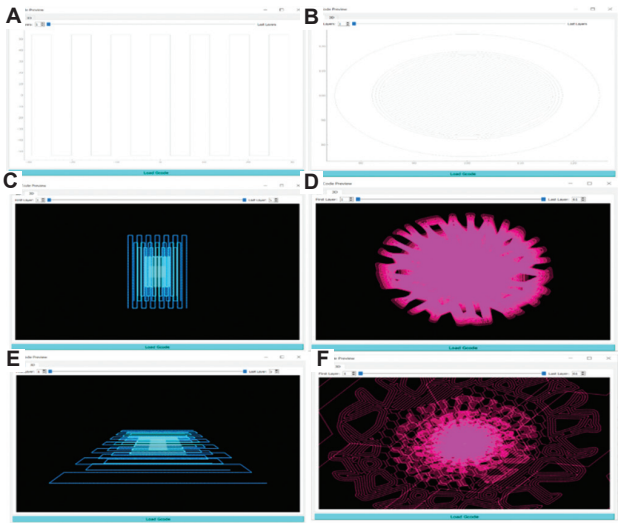

Figure 3. Visualization of single layers (A, C, and E) versus multiple layers (B, D, and F).

To demonstrate the ease of viewing complex structures' layered compositions, Figure 6 was made. In Figure 6C, the particular sequence of layers (69 through 89) was chosen and refers to the highlighted G-code command lines in Figure 6A. The visualization program started with the command line (G1 = X86.980 Y110.590 E39.71886) for layer 69 and stopped at layer 89 using the command line (G1 = X108.649 Y112.360 E7.81012). Therefore, it plotted all command lines between these two layers. This feature allows users to see the specific details of any given layer. To elucidate, this allows the user to see the process of printing intermediate layers without the consideration of preceding or following layers. This can be practical since some of the objects have multiple features, such as in the Marmalade Reef, as shown in Figure 6F. This reef demonstrates the complexity a G-code can contain and illustrates the convenience of viewing the result of 3D printing using a single command line. For instance, while Figure 6B and 6C showcase the entirety and the fraction of the printed reef, respectively, a glance at either Figure 6A or 6D shows that the individual layers contained in the reef's overall shape, regardless of their intermediate nature.

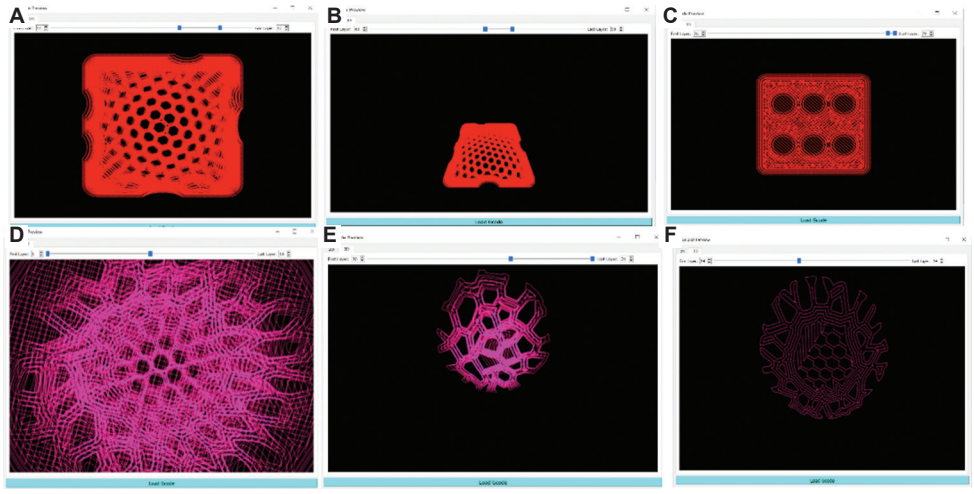

Figure 4. (A-F) Ability to zoom in and out using a three-dimensional preview.

Figure 5. (A-C) Detailed view of multiple layers (three-dimensional) and single layers (two-dimensional) visualization.

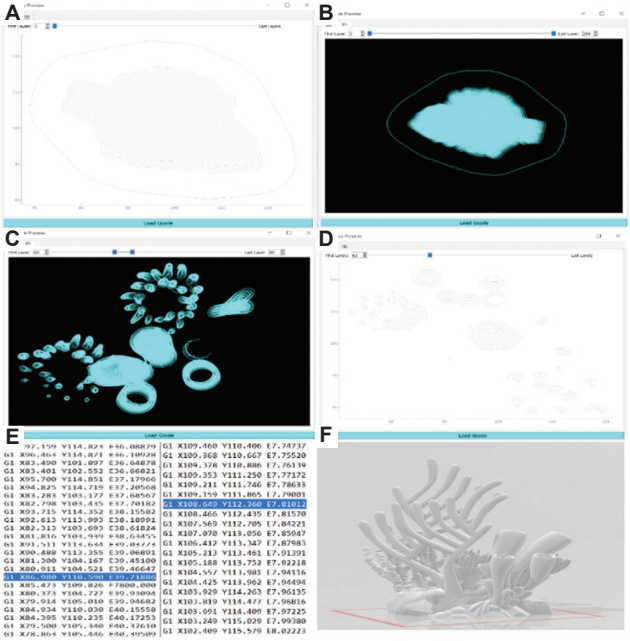

Figure 6. (A-F) Marmalade reef preview and command details for specific layers.

4. Conclusion

The proposed "2D and 3D Model Visualization Software" can visualize a G-code file by translating the commands into 2D and 3D objects before operating the machine. In the future, other features will be added, such as converting STL files into G-code, creating G-code shape paths, and modifying the current files of G-code. Adding this tool to the TwinPrint System reduces the use of several applications while printing, leading to a faster result that optimizes the printing to be as time efficient as possible while maintaining cost effectiveness. Moreover, the proposed method was optimized and improved to achieve the intended goal with the element of interactivity being added to the software.

Acknowledgments

The authors would like to acknowledge Ali Balubaid for his support.

Funding

The research reported in this publication was supported by funding from King Abdullah University of Science and Technology(KAUST).

Conflict of interest

There are no conflicts to declare.

Author contributions

Conceptualization: Zainab N. Khan, Shaddin AlZaid, Charlotte A. E. Hauser

Investigation: Shaddin AlZaid, Noofa Hammad, Zainab N. Khan

Methodology: Shaddin AlZaid, Hamed I. Albalawi

Software: Shaddin AlZaid

Visualization: Shaddin AlZaid, Hamed I. Albalawi

Writing – original draft: Shaddin AlZaid, Noofa Hammad, Hamed I. Albalawi

Writing – review & editing: Shaddin AlZaid, Noofa Hammad, Hamed I. Albalawi, Eter Othman, Charlotte A. E. Hauser.

References

1. Kim Y, Nowzari H, Rich SK, 2013, Risk of prion disease transmission through bovine-derived bone substitutes: A systematic review. *Clin Implant Dent Relat Res*, 15: 645–653.

   https://doi.org/10.1111/j.1708-8208.2011.00407.x

2. Ashammakhi N, Kaarela O, 2018, Three-dimensional bioprinting can help bone. *The J Craniofac Surg*, 29: 9–11.

   https://doi.org/10.1097/SCS.0000000000004143

3. Tavafoghi M, Darabi MA, Mahmoodi M, *et al.*, 2021, Multimaterial bioprinting and combination of processing techniques towards the fabrication of biomimetic tissues and organs. *Biofabrication*, 13: 42002.

   https://doi.org/10.1088/1758-5090/ac0b9a

4. Liu W, Zhang YS, Heinrich MA, *et al.*, 2017, Bioprinting: Rapid continuous multimaterial extrusion bioprinting (Adv. Mater. 3/2017). *Adv Mater* (*Weinheim*), 29:1604630.

   https://doi.org/10.1002/adma.201770016

5. Ng WL, Lee JM, Zhou M, *et al.*, 2020, Vat polymerization-based bioprinting process, materials, applications and regulatory challenges. *Biofabrication*, 12: 022001.

   https://doi.org/10.1088/1758-5090/ab6034

6. Jiang T, Munguia-Lopez JG, Flores-Torres S, *et al.*, 2019, Extrusion bioprinting of soft materials: An emerging technique for biological model fabrication. *Appl Phys Rev*, 6: 011310.

   https://doi.org/10.1063/1.5059393

7. Li X, Liu B, Pei B, *et al.*, 2020, Inkjet bioprinting of biomaterials. *Chem Rev*, 120: 10793–10833.

8. Tekin E, Smith PJ, Schubert US, 2008, Inkjet printing as a deposition and patterning tool for polymers and inorganic particles. *Soft Matter*, 4: 703–713.

9. Villar G, Graham AD, Bayley H, 2013, A tissue-like printed material. *Science*, 340: 48–52.

10. Xu T, Jin J, Gregory C, *et al.*, 2005, Inkjet printing of viable mammalian cells. *Biomaterials*, 26: 93–99.

11. Zhang LG, Leong K, Fisher JP, editors. 2022, 3D Bioprinting and Nanotechnology in Tissue Engineering and Regenerative Medicine. Academic Press, Cambridge, Massachusetts.

12. Miri AK, Nieto D, Iglesias L, *et al*., 2018, Bioprinting: Microfluidics-enabled multimaterial maskless stereolithographic bioprinting (Adv. Mater. 27/2018). *Adv Mater* (*Weinheim*), 30: 1870201–n/a.

https://doi.org/10.1002/adma.201870201

13. Ng WL, Chan A, Ong YS, *et al*., 2020, Deep learning for fabrication and maturation of 3D bioprinted tissues and organs. *Virtual Phys Prototyp*, 15: 340–358.

https://doi.org/10.1080/17452759.2020.1771741

14. An J, Chua CK, Mironov V, 2021, Application of machine learning in 3D bioprinting: Focus on development of big data and digital twin. *Int J Bioprint*, 7: 342.

https://doi.org/10.18063/ijb.v7i1.342

15. Bikas H, Stavropoulos P, Chryssolouris G, 2015, Additive manufacturing methods and modelling approaches: A critical review. *Int J Adv Manuf Technol*, 83: 389–405.

https://doi.org/10.1007/s00170-015-7576-2

16. Ueng SK, Chen LK, Jen SY, 2017, A Preview System for 3D Printing. In: 2017 International Conference on Applied System Innovation (ICASI), p1508–1511.

17. Gahbiche MA, Boudhaouia S, Giraud E, 2020, A finite element simulation of the incremental sheet forming process: A new method for G-code implementation. *Int J Mater Prod Technol*, 61: 68–86.

18. Khan Z, Albalawi H, Valle-Perez A, 2022, From 3D printed molds to bioprinted scaffolds: A hybrid material extrusion and vat polymerization bioprinting approach for soft matter constructs. *Mater Sci Addit Manuf*, 1: 7.

https://doi.org/10.18063/msam.v1i1.7

19. Abdelrahman S, Alsanie WF, Khan ZN, 2022, A Parkinson's disease model composed of 3D bioprinted dopaminergic neurons within a biomimetic peptide scaffold. *Biofabrication*, 14: 044103.

https://doi.org/10.1088/1758-5090/ac7eec

20. Hammad N, AlZaid S, Alwazani H, 2022, TwinPrint: A Dual-Arm Robotic System for 3D Biofabrication, Viewed August 22, 2022. In: RobotoKAUST KAUST Research Conference on Robotics and Autonomy.

21. Albalawi H, Khan ZN, Valle-Pérez AU, *et al*., 2021, Sustainable and eco-friendly coral restoration through 3D printing and fabrication. *ACS Sustain Chem Eng*, 9: 12634–12645.

https://doi.org/10.1021/acssuschemeng.1c04148

22. Lim J, 2022, Plotting with PyQtGraph Create custom plots in PyQt with PyQtGraph, 2020. Available from: https://www.pythonguis.com/tutorials/plotting-pyqtgraph [Last accessed on 2020 May 02].

23. Zhang Y, 2020, Gcode-Reader. Available from: https://github.com/zhangyaqi1989/Gcode-Reader [Last accessed on 2021 Feb 02].

24. Marvin Killing, 2014, QxtSpanSlider. Available from: https://github.com/mkilling/QxtSpanSlider.py [Last accessed on 2021 Sep 16].

25. Coolsunxu, 2021, Video_Cut. Available from: https://github.com/coolsunxu/Video_Cut/blob/main/main.py [Last accessed on 2021 Sep 22].

Materials Science in Additive Manufacturing

ORIGINAL RESEARCH ARTICLE

Increasing density and mechanical performance of binder jetting processing through bimodal particle size distribution

Ana Paula Clares[1], Yawei Gao[2], Ryan Stebbins[2], Adri C.T. van Duin[2], Guha Manogharan[1,2]*

[1]Additive Manufacturing and Design Graduate Program, The Pennsylvania State University, University Park, PA 16801, USA

[2]Department of Mechanical Engineering, The Pennsylvania State University, University Park, PA 16801, USA

Abstract

Binder jetting is an additive manufacturing (AM) technology that has gained popularity and attention in recent years for production applications in tooling, biomedical, energy, and defense sectors. When compared to other powder bed fusion-based AM methods, binder jetting processes powder feedstock without the need of an energy source during printing. This avoids defects associated with melting, residual stresses, and rapid solidification within the parts. However, one of the challenges of this process is the relatively lower densities which impacts part density, and subsequently, sintering and mechanical properties. In this study, we investigated the influence of bimodal powder size distributions (a mixture of coarse to fine particles) as a method for increasing part density and mechanical strength, and used stainless steel (SS) 316L bimodal mixtures in this case. Four unimodal and two bimodal groups were evaluated under similar AM processing conditions for sintered density measurements and flexural strengths. Our results demonstrated that bimodal size distributions showed a statistically significant increase in density by 20% and ultimate flexural strength by 170% when compared to the highest performing unimodal group. In addition to experimental findings, reactive molecular dynamics simulations showed that the presence of finer powders along with coarser particles in the bimodal particle mixture contribute to additional bonds that are stronger across the particle interfaces. Findings from this study can be used to design bimodal particle size distributions to achieve higher density and better mechanical properties in binder jetting AM process.

Keywords: Binder jetting; Bimodal powder; Mechanical strength; Molecular dynamics; 316L stainless steel; Additive manufacturing

***Corresponding author:**
Guha Manogharan
(gum53@psu.edu)

Citation: Clares AP, Gao Y, Stebbins R, *et al*., 2022, Increasing density and mechanical performance of binder jetting processing through bimodal particle size distribution. *Mater Sci Add Manuf*, 1(3): 20
https://doi.org/10.18063/msam.v1i3.20

Received: August 26, 2022

Accepted: September 15, 2022

Published Online: September 29, 2022

Copyright: © 2022 Author(s). This is an Open Access article distributed under the terms of the Creative Commons Attribution License, permitting distribution, and reproduction in any medium, provided the original work is properly cited.

Publisher's Note: Whioce Publishing remains neutral with regard to jurisdictional claims in published maps and institutional affiliations.

1. Introduction

Binder jetting was developed in the early 1990s and is one of the seven additive manufacturing (AM) technologies. Similar to direct energy deposition (DED) and laser powder bed fusion (LPBF), this technology processes powder feedstock for the fabrication of parts. The process begins with powder dispensing with a rake or blade or rotating roller to spread a thin layer of powder on a build platform. Next, the binder

is selectively deposited with an array of nozzles that eject the solution onto the powder bed. This process is repeated layer by layer until a final part is achieved to produce a "green part." On build completion, post-processing steps, such as curing, depowering, sintering, infiltration, and finishing, are necessary to achieve final densification.

Binder jetting offers multiple advantages, such as eliminating the need for support structures, powder reusability, and part nesting. In contrast to other powder AM technologies, it is a non-fusion-based process that does not rely on high energy sources (e.g., laser and electron beam) during fabrication. The only external heat present during the process is for the partial drying of the binder across each layer. The lack of elevated heat input is beneficial as it evades melting and rapid solidification defects, as well as residual stresses accumulated in other AM processed parts[1]. Binder jetting is regarded as a very flexible AM technique that offers a wide range of material selections, such as sand, ceramics, polymers, and metals[1]. Applications of binder jetting include tooling, fuel cells, scaffolds, molds, construction, and electronic antenna[2-11] due to its ability in fabricating relatively complex geometries rapidly at larger volumes, and lower machine and production costs[12]. The lack of distortions introduced to the part due to the absence of thermal gradients, and the lack of thermal crack formations makes this AM technology attractive for continuous investigation in academia and industrial applications. When compared to LPBF and DED, the number of materials investigated in binder jetting is smaller but that is increasing[13].

Despite the high popularity of binder jetting, especially for optically reflective and thermally conductive metals[14], one of its limitations is the relatively lower densities of printed parts when compared to fabrications through powder metallurgy or other metal AM processes[15]. Binder jetting as-built (green stage) parts are typically brittle, porous, and with lower mechanical properties[16]. The previous work reported average relative densities obtained of around 40 – 60% in binder jetting fabrications[16-18]. Efforts have been made to increase the overall density of printed part in post-processing, such as infiltration, hot isostatic pressing (HIP), optimization of printing process parameters, and powder properties[15]. For example, Vogt *et al.* reported a 26% increase in green density after infiltration[19] while Porter *et al.* calculated a 65% density improvement when compared to green parts during the fabrication of Al-based metal matrix nanocomposites[20]. Kumar *et al.* demonstrated that through the use of the HIP technique, a maximum density of 97% and 92% in copper parts could be achieved[21,22]. Another study showed that full densification was achieved with HIP in binder jetting of nickel-based superalloy[23]. Optimization process parameters have also been studied for density improvement. Shrestha *et al.* analyzed the impact of several process parameters (binder saturation, layer thickness, and feed-to-powder ratio) and concluded that achieving higher packing density during powder spreading is critical to achieving higher final density[24]. Lecis *et al.* also studied the influence of layer thickness, binder saturation, as well as debinding and sintering atmospheres to achieve final densities of 98%[12].

The focus of this work lies in the effects of powder properties, specifically powder size distribution during binder jetting to achieve superior part properties through higher density. Prior efforts in powder metallurgy have shown that bimodal powder mixtures can improve packing density and dimensional control after sintering[14,25]. Both coarse and fine particles are mixed (e.g., 1:3-1:6 volumetric ratios) to increase packing density through filling of fine particles into the voids created between the coarse particles[26]. Du *et al.* investigated the use of bimodal powder feedstocks in silicon carbide ceramics by achieving a 5% increase in green density when compared to unimodal powder prints[25]. Du *et al.* used spherical alumina powders to demonstrate the improvements in powder bed density and sintered density with an analytical model to find the optimal mixing fraction in bimodal mixtures[27]. Bai *et al.* experimentally evaluated the effect of bimodal copper printed parts and observed an increase of 16.2% in powder bed density and 12.3% in sintered density, depending on the variation of sinter conditions[15]. Bai *et al.* studied the impact of copper bimodal mixtures that resulted in an 8.2% improvement in powder packing density and a 4% increase in sintered density[19]. Sinterability and density improvements were also observed in bimodal size distribution in binder jetting of SS 316L but its effects on mechanical strength were not evaluated[20].

Even though the impact of bimodal distributions in green and sintered densities has been explored, there is still a need to understand the effect of bimodal particle size distribution in SS316L binder jetting and its impact on sintered density and mechanical performance. The motivation of this paper is to experimentally validate the benefits of bimodal mixtures on sintered density and mechanical performance. This effort builds on a previous computational work based on discrete element method and the effects of particle size distributions on packing density, porosity, and flowability[28]. In addition, the experimental work of this paper serves as a benchmark for the modeling work, which provides an atomistic level insight into the strengthening mechanism of the bimodal particle size distribution using the ReaxFF molecular dynamics (MD) simulations.

Section 2 describes the experimental methods with a focus on material selection, powder characterization, part fabrication and printing conditions, as well as post-

processing. Section 3 describes the characterization and evaluation techniques employed in this study. Sections 4 and 5 detail the results obtained in this study and discuss their implications, respectively. Finally, Section 6 highlights the major findings and directions for future research.

2. Experimental methods

2.1. Material selection

Nitrogen gas atomized (SS316L) 316L stainless steel powder with similar chemical compositions were obtained from two powder manufacturers, Sandvik (Stockholm, SE) and Carpenter Additive (Philadelphia, USA). Batch sampling was conducted using ELEMENTRAC ONH-p 2 and ELEMENTRAC CS-I (ELTRA, USA) for total C, S, O, N, and H content. The O%, N%, and H% content were extracted through inert gas fusion technique, while combustion was used for C% and S% concentration (Table 1).

2.2. Powder characterization

To evaluate the impact of powder size distribution, six powder size groups were prepared using a vibratory sieve (Retsch AS 200 Control, Haan DE), as shown in Table 2 for four unimodal and two bimodal distributions.

Using dynamic image analysis (DIA) technique through Microtrac MRB-CAMSIZER X2 equipment (Newtown, PA), particle size distribution and morphology were measured following the ISO 13322-2 standard[29]. As shown in Figure 1A, median particle size (D50) values for unimodal groups are around 12 µm, 22 µm, 31 µm, and 36 µm for Groups 1, 2, 3, and 4, respectively. Groups 5 and 6 consist of bimodal particle size distributions, which is a combination of coarse and fine particles. Based on literature work, a coarse fine particle size ratio of 1:3 – 1:4 is ideal for bimodal mixtures with a corresponding weight ratio of 27:73 which was evaluated to increase powder packing density[30] by mixing for 2 h in a heavy-duty shaker mixer (Turbula-WAB Group, CH). Figure 1B displays powder morphology obtained at 0.8 µm per pixel, showing high sphericity in the SS316L stainless steel powder used in this work. Some surface defects and satellites were observed as well, which could be beneficial for powder flowability.

Table 1. Chemical composition of as sourced SS316L powders

Powder manufacturer	C%	S%	O%	N%	H (ppm)
Carpenter Additive	0.014	0.005	0.040	0.090	5.490
Sandvik Osprey	0.013	0.004	0.149	0.145	16.720

Table 2. Powder size groups (µm)

	Groups	D10	D50	D90
Unimodal distribution	10 µm	5.3	12.5	22.6
	20 µm	16.3	22.1	29.8
	30 µm	22.1	31.3	41.8
	40 µm	25.7	36.4	48.3
Bimodal distribution	30 (73%)+10 µm	10.6	26.8	39.0
	40 (73%)+10 µm	10.7	32.7	47.4

2.3. Part fabrication and printing parameters

An ExOne (North Huntingdon, PA) Innovent + binder jetting machine with 30 µm print resolution was used for the fabrication of all parts. BA005 aqueous-based binder (supplied by ExOne) was deposited which uses polyvinylpyrrolidone (PVP) polymer as a bonding agent. A total of six builds were printed corresponding to each powder size group. To evaluate and compare the mechanical strength of the unimodal and the bimodal distributions used, 31.7 mm × 12.7 mm × 6.35 mm bars were fabricated as per the ASTM B528-99 standard. To evaluate the sintered density in the fabricated parts (unimodal vs. bimodal), 7 mm (D) × 20 mm (L) cylinders were printed, as shown in Figure 2.

To isolate the effects of build layout and orientation, a total of five bars and four cylinders were printed per build and placed in different locations. The bars were fabricated perpendicular to the load direction within the build platform, as shown in Figure 3.

Several studies have noted that process-related parameters affect part density and mechanical performance[24,31]. Table 3 provides an overview of the process parameters that were utilized for the fabrication of all SS316L samples in this study. Layer thickness varied slightly across groups, as this is a variable directly related to the powder size. It is recommended that the thickness of the layers should be around 3 times the particle diameter for higher packing density and a smooth surface finish[32]. Another parameter that slightly varied across groups was the recoat speed, which is the speed at which the hopper traverses the build while dispensing powder[33]. It can be observed that a lower speed (mm/s) was utilized for finer particles because of the difficulty in powder dispensing due to clumping and agglomeration. In addition, bed drying time, which is the time the heat lamp takes to pass over the deposited binder for drying, was adjusted between groups due to differences in particle sizes. Observations of part bleeding and layer delamination guided the selection of bed drying time.

2.4. Post-processing

Following green part fabrication, all samples were cured in an oven at 200°C for 5 h, followed by manual

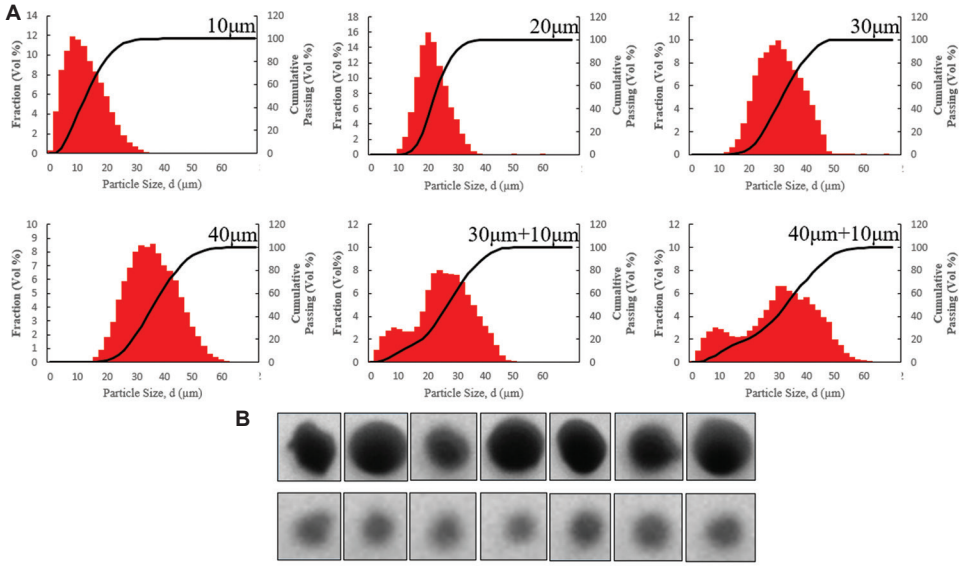

Figure 1. (A) Powder size distributions of SS316L groups. (B) Powder morphology.

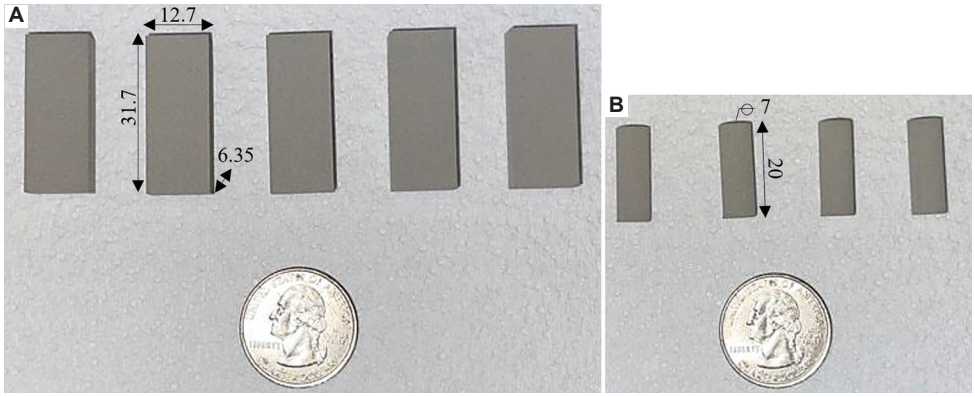

Figure 2. Example of green 10 μm group size samples. (A) Bars (mm). (B) Cylinders (mm).

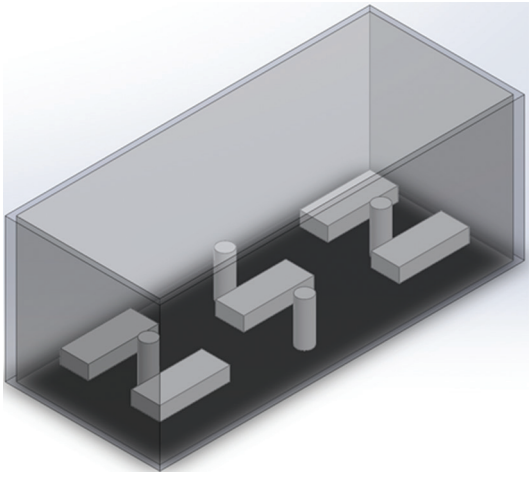

Figure 3. Build layout for each powder size group.

Table 3. Printing process parameters

Parameter	Particle size groups					
	10 μm	20 μm	30 μm	40 μm	30+10 μm	40+10 μm
Layer thickness (μm)	Ranged from 100 to 115					
Desired saturation (%)	65 in all size groups					
Rotation speed (rpm)	500 in all size groups					
Traverse speed (mm/s)	3 in all size groups					
Recoat speed (mm/s)	30	30	60	60	60	60
Bed temperature (°C)	55 in all size groups					
Bed drying time (s)	5	5	10	10	15	15

depowdering and removal from the build box. Finally, all samples were sintered in a fully inert atmosphere filled with argon gas. A tube furnace (Carbolite Gero Ltd.) was used with the following temperature profile, as shown in Figure 4: (i) 3°C/min ramp to 700°C, 60 min dwell; (ii) 3°C/min ramp to 1120°C, 140 min dwell; (iii) cool down at 3°C/min to 850°C, 90 min and to 300°C, 183 min; and (iv) cool down at 3°C/min to room temperature. A similar sinter cycle can be observed in previous SS316L binder jetting work[24].

3. Part evaluation techniques

3.1. Sintered density

Sintered density was calculated for all cylinder samples from each group (n = 4) using both physical and micro-X-ray computed tomography (XCT) methods. Specimen dimensions were recorded using a digital caliper (10 µm accuracy) for the cylinder dimensions and a digital scale (0.1 mg) for weight recordings. In Equation I, the formula used for caliper density calculations is shown, where $m_{cylinder}$ is the total mass of the cylinder and $v_{cylinder}$ is the volume using the radius and height of the cylinder. This value was later divided by the theoretical density of SS316L stainless steel (8.00 g/cm^3) for relative density % present in the printed part.

$$\rho_{sintered} = \frac{m_{cylinder}}{v_{cylinder}} \quad \text{(I)}$$

On collecting sintered data from all printed samples (n = 4/group), a more precise calculation of density was further explored using XCT on one sample per group size. This technique was selected as it is a non-invasive tool that enables the evaluation of internal features of printed parts. A GE Vtomex L300 CT scanner with a microfocus tube was used. Scans were collected using a 250kV 40 µA X-ray beam with 10 µm voxel resolution. Raw XCT data were collected as 16-bit tiff stack files and imported for processing into ImageJ software for image preparation and gray scale correction. AVIZO was used for the visualization and analysis of XCT data. Segmentation and thresholding of the data were performed to extract the material (SS316L) of the printed cylinder. The total volume of the solid cylinders (without accounting for porosity) was calculated using AVIZO's internal tool. Figure 5 shows the printed cylinders from the XCT scans segmented and displayed in AVIZO. The higher part resolution achieved with 10 µm can be observed along with segmented porosity, which is shown in black.

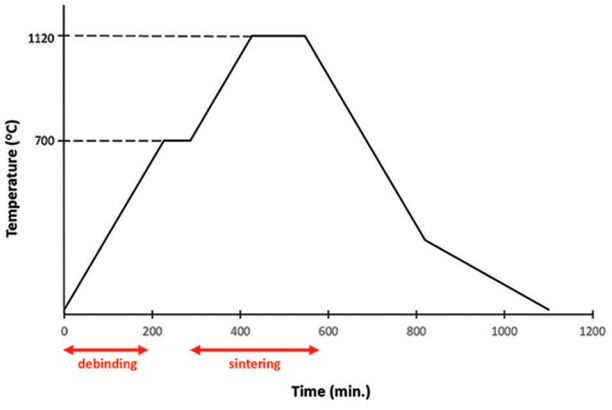

Figure 4. Time-temperature profile used for sintering SS316L samples.

3.2. Mechanical testing

Sintered test coupons (n = 5/group size) were subjected to ultimate flexural strength (UFS) 3-point bending test as per ASTM B528-16 standard at 2.5 mm/min loading rate until complete rupture in an MTS Landmark 22 Kip servo hydraulic test. UFS and flexural modulus (FM) described in Equation II were computed based on F, L, w, t – force required to rupture, span distance, specimen width, thickness, and slope of the line tangent to the load displacement curve, respectively.

$$\sigma_{\max flex} = \frac{3FL}{2wt^2} \quad \text{(II)}$$

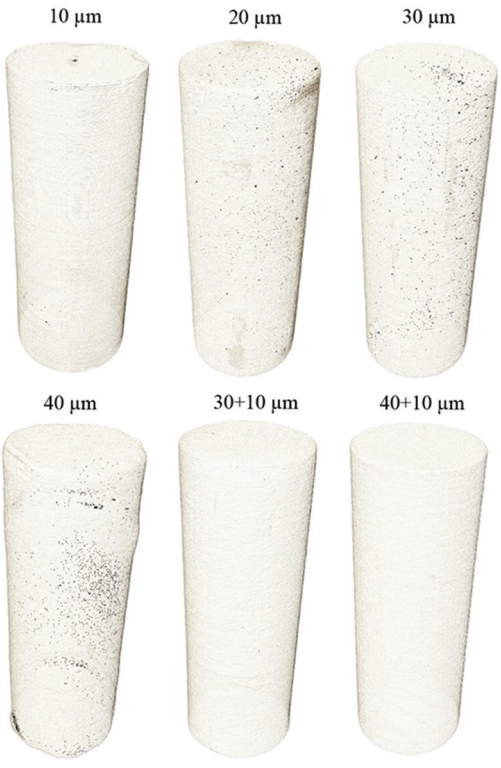

Figure 5. Pores reduced in bimodal powder size groups as observed from X-ray computed tomography results.

3.3. Statistical analysis

Statistical analysis was performed on density values and UFS to determine any statistical differences between groups. Both sintered density (n = 4) and UFS (n = 5) results were compared based on powder size groups (six groups). A Ryan-Joiner test (similar to Shapiro–Wilk) was performed (α = 0.05) in Minitab to verify for normal distribution before Bartlett's test for equal variance. One-way analysis of variance (ANOVA; α = 0.05) was performed, along with a Tukey multiple comparison test to compare group means. If the normality test failed, a Kruskal–Wallis non-parametric test was run in Python to evaluate the statistical difference in median values between groups. A Dunn's test, with a Bonferroni correction, was applied to identify the statistically different groups and to reduce family-wise error rate and Type I errors.

3.4. ReaxFF MD simulations

ReaxFF MD simulations are a force field-based atomistic modeling method. The smooth bond order transition for bond breaking and formation enables ReaxFF to model the solid/liquid and solid/solid chemical reactions in the binder jetting additive manufacturing process. In a previous work by the authors, the solid-liquid interactions between Cr-oxide in SS particles and binder solutions were modeled with a system that contains Cr-oxide nanoparticles, diethylene glycol, and water molecules[25]. The simulation results provided a molecular level explanation of the strengthening mechanism from print to the sintering stages. In another study by the authors, two sizes of particles were prepared to model the bimodal particle size distribution[26]. The particles have a Fe-Cr_2O_3 core-shell structure. The ReaxFF MD simulations were carried out at room temperature, 120°C, and 1120°C to compare the bimodal and unimodal particle size distribution regarding the chemical and physical evolution at the print, curing, and sintering stages, respectively. Rupture strengths were computed after the system reaches equilibrium at each temperature. More details regarding the simulations can be found in this paper[34]. In this work, we compared the rupture strengths of sintered products computed with the ReaxFF potential from Gao *et al.*[34] with experimental measured by the 3-point flexural test.

4. Results

4.1. Sintered density

Sintered density (n = 4 cylinders measured with calipers) corresponding to each of the six particle size distribution groups is shown in Figure 6. A visible trend within the unimodal groups is observed, showing a decrease in density as the particle sizes increase up to 40 μm. The 40 μm density was found to be 5.11% and 6.77% larger than the 20 and 30 μm groups, respectively. The 30 + 10 and 40 + 10 μm bimodal groups displayed a much higher density than any of the unimodal groups with average relative densities of 71.83% and 71.57%. In addition, the 30 + 10 and 40 + 10 μm bimodal groups showed a 20.18% and 19.74% increase in sintered density when compared to the highest density group of 10 μm unimodal powders.

The Ryan-Joiner test showed that the sintered density data presented were not normally distributed. Because of this, a Kruskal–Wallis (α = 0.05) non-parametric test was performed, showing $P < 0.05$. This value indicated that due to the statistical difference between median values of each group, particle size distribution does have a statistical impact on the sintered density results obtained through this study. A Dunn's test with Bonferroni correction found that the 30 μm group was the only group that was statistically lower than both bimodal groups, as shown in Figure 6.

Additional density measurements were calculated using XCT data. Although minor differences can be observed in the obtained XCT densities when compared to physical measurements (8.2%), the trends are consistent with each other. For instance, the highest density was still achieved in bimodal groups at 74.82% and 76.99% followed by the unimodal 10 μm at 66.80%, as shown in Figure 7.

4.2. Three-point bending

UFS results (n = 5 bars) from each group, obtained from the 3-point bending test, are shown in Figure 8. A clear decreasing trend in UFS with an increase in particle size among the unimodal group can be observed, which agrees with the results found with the sintered density in Section 4.1. However, unlike the density trend reported previously, which saw a slight increase in 40 μm density compared to the 20 μm and 30 μm, a continuous decrease in UFS from 10 μm to 40 μm was observed in this study.

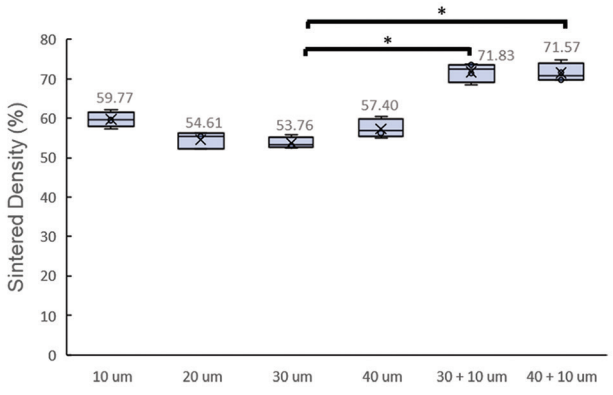

Figure 6. Sintered density values across unimodal and bimodal particle size groups. *P = 0.01 – 0.05.

The Ryan-Joiner test also indicated that the UFS data were not normally distributed. The Kruskal–Wallis (α = 0.05) non-parametric test was performed. It was found that both bimodal groups were statistically higher than the 30 µm and 40 µm group, as shown in Figure 8. Due to the size limitations of the tube furnaces used for sintering, only three bars were sintered at a time. It was suspected that variation in sintering conditions both within and across particle groups could be present, as shown in Table 4. This may be an influencing factor on why statistical differences between some of the unimodal and bimodal groups were not observed, despite the 168.3% and 173.4% increase in UFS from the 10 µm to the 30 + 10 and 40 + 10 µm groups, respectively. Results gathered from samples that were sintered in the same batch were used to see the impact different sintered runs had on the UFS. As shown in Table S1 (in Supplementary File), analysis of UFS of particle size groups sintered in the same batch resulted in lower relative standard deviation (RSD). This indicates significant variations in strength between sintered groups.

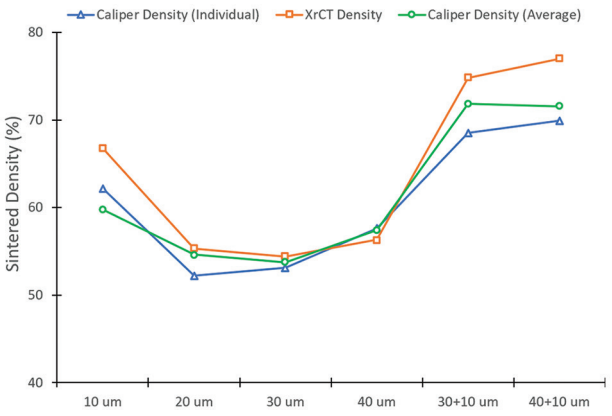

Figure 7. Relationship and trend between all particle groups with respect to X-ray computed tomography, caliper measured (individual) density, and caliper measured (average) density.

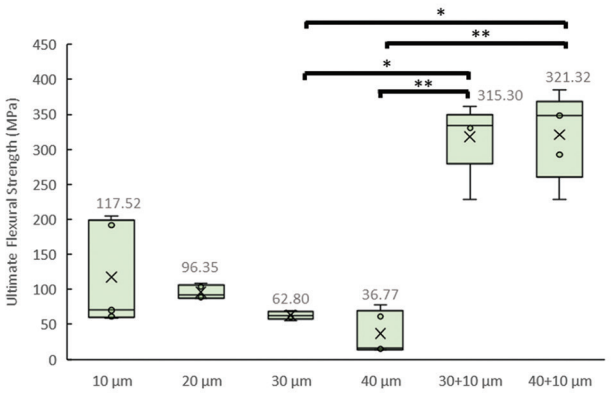

Figure 8. Ultimate flexural strength (UFS) shows that bimodal particles have higher flexural strength. *P = 0.01 – 0.05 and **P < 0.01.

However, when both the truncated and full datasets were compared, as shown in Figure 8 and Figure S1 (in Supplementary File), a similar trend can be seen but with different statistical significance.

According to our previously reported MD simulations, the fine powders filling the interparticle voids can contribute extra bonds to connecting the coarse particles after sintering[26]. As a result, the rupture strengths are enhanced in the bimodal particle mixture than in the unimodal particle size mixture. It should be noted that the rupture strength observed in the ReaxFF-MD simulations was improved by 40.9%, which was much lower than the >170% measured improvements demonstrated in the 3-point bending tests. This could be attributed to the lower number of fine particles in the MD simulation.

5. Discussion

Based on the findings from this study, it can be observed that bimodal distribution feedstock achieves higher density and mechanical properties for SS316L. Our work showed a statistically significant increase in sintered density with the introduction of bimodal groups when compared to unimodal distributions, which is in agreement with prior reports[4,19,20]. The improvement in density after sintering conditions could be attributed to better filling effects that could result in more contact and necking, which is beneficial for sintering and shrinkage reduction. To the best of our knowledge, this is the first study that reports a statistically significant increase of more than 20% in sintered density in the bimodal particle size distribution.

The increase in density observed with our bimodal results aligns with Du *et al.*'s findings when studying silicon carbide in which a 5% increase in bimodal green density was observed when compared with the unimodal distributions[25]. Du *et al.* analyzed different coarse powder fractions (%) for bimodal mixing and found the highest density values of 70 – 75% coarse particles in the mixture, which is comparable to the 73% used in this study. The appropriate selection of a coarse-to-fine ratio has been shown to impact part density. The ratio used in this study

Table 4. Summary results across particle groups

Group	Sintered density (%)			Ultimate flexural strength (MPa)		
	Mean	Std.	RSD	Mean	Std.	RSD
10 µm	59.77	1.98	3.31%	117.50	74.20	63.15%
20 µm	54.61	2.12	3.88%	96.35	9.81	10.18%
30 µm	53.76	1.43	2.66%	62.80	5.78	9.20%
40 µm	57.40	2.33	4.06%	36.80	30.80	83.70%
30+10 µm	71.83	2.47	3.44%	315.30	59.05	18.74%
40+10 µm	71.57	2.36	3.30%	321.30	61.80	19.02%

has been found to achieve high packing density in other reported studies. Bai *et al.* demonstrated that although higher sintered density was always achieved in bimodal distributions, different mixing ratios (1:3 – 1:6) would result in different values[30].

As observed in Figure 6, a clear trend of decrease in density with an increase in particle size within unimodal groups can be observed. Similar results have been reported in the literature in other metals and ceramics[2,35-37]. Finer particles are known to enhance the sintering process due to the initial necking when compared with coarser particles. In addition, the increase in surface energy and contact area associated with finer particles favors sinterability due to a higher particle bonding rate. In this study, density decreased with an increasing particle size up until the 40 µm group, where a slight increase in density was observed. We attribute this possible outlier to variations in sintering conditions associated with non-uniform inert atmospheres at the tail ends of the tube furnace (Figure 9A). Temperature data were tracked and gathered during each of the sinter runs, which indicated that an identical heating profile was followed for all samples. It has been reported that the density of SS316L metal injection molding parts was impacted by different gas atmospheres as well as other sintering factors[38]. Other papers have discussed the effects of the sintering atmosphere on SS316L[39]. As tube furnaces only have a relatively small hot zone, any minor differences in the precise placement of the samples in the alumina crucible could have caused this observation. Future studies will include real-time monitoring of gas flow rate and development of a jig to precisely repeat the placement of sintering samples within the crucible.

During the sintering stage of a binder jetting process, off-gassing takes place as the binder is evaporated from the part (debinding). A higher gas flow rate might be beneficial for uniformly carrying these chemicals out of the furnace chamber and away from the part. As shown in Figure 9, the differences between sintered runs of the same particle group have different colorations, indicating a slight difference in the gas atmosphere or flow rate. In addition, as shown in Figure 9A, gas flow lines are seen in only one of the samples, indicating that the possible impact sample position might have on result variability. The truncated data contain samples only sintered at the same time, resulting in much lower standard deviations, as shown in Table S1 (in Supplementary File). This is believed to be a further evidence that the higher density seen with the 40 µm cylinders might be caused by the higher amount of surface oxides. After performing data analysis on all sintered density values, the results showed no statistical difference between the 40 µm and any other unimodal groups. In summary, the bimodal groups have a higher density when compared to the unimodal groups.

Figure 9. Different sinter runs for the same particle size group. *Top right bar corresponds to a different group.

In general, a higher density results in higher mechanical strength because of the detrimental impact of porosity during mechanical loading. Jost *et al.* also found that the ductility and strain at ultimate tensile strength for SS316L manufactured through powder bed fusion method were negatively impacted by porosity[40]. Our results presented in Figure 8 agree with the claim that higher density (found in bimodal groups) corresponds to higher UFS. As previously mentioned, the 40 µm group saw a slight deviation from the observed density trend within the unimodal group. Conclusions about this phenomenon rely on the possibility of surface porosity or open porosity present with that group. Because the sintered density was calculated using physical measurements, the bulk volume (including open and closed pores) was used. Future investigations should rely on more advanced sintered density measurements, such as the Archimedes method or He pycnometry, for more precise measurement.

The surface porosity might have resulted in higher calculated density but lower strength. Reports of surface defects and roughness's impact on mechanical performance are highlighted in Masuo *et al.*'s work[41]. Overall, no statistical difference was found between unimodal groups. The increase in UFS of bimodal particle size group when compared to unimodal groups is highly statically significant. Mechanical values presented with this work can be compared with a literature investigation where Shrestha *et al.* reported a maximum UFS of 90.10 MPa using binder jetting SS316L with similar sintering profile with only unimodal distributions.

Finally, the relative density (density calculated/theoretical density) was low (the highest sintered density achieved was around 72%) when compared to densities achieved by other studies. Based on the literature reports, sintered density in binder jetting has in some cases reached around 95% depending on the specific material and the process parameters used. A reduction in density may be a consequence of insufficient sintering conditions, such as low sintered temperatures used and possible part expansion

due to debinding caused by outgassing[19]. A higher sinter temperature should be considered to facilitate mass transport and increase the part density[42]. In addition, this study did not optimize binder saturation, rolling speed, and other process parameters. Based on other reported studies, higher density values have been obtained by appropriately selecting specific process and thermal parameters that would enhance the printing performance[2,14]. Future work should focus on finding different parameters and adjusting them for density increases, as well as investigating the impact of sintering profiles and their effect on bimodal distributions as they are directly affected by powder properties and packing state.

6. Conclusions

The goal of this study was to evaluate the impact bimodal distributions in binder jetting of SS316L feedstock. Six different particle distributions, that is, four unimodal (10 μm, 20 μm, 30 μm, and 40 μm) and two bimodal (30 + 10 μm and 40 + 10 μm), were compared. An ExOne Innovent + was used to print four cylinders and five bars per particle size group. The samples were cured and sintered; cylinders were used to calculate density and bars were used for 3-point bending using weight and XCT data. Density and UFS (through 3-point bending tests) were used to compare the impact of the particle distribution. The measured UFS was compared with the MD simulations using the ReaxFF potential. Based on the results, the main conclusions are as follows:

(i) A bimodal powder distribution is preferred over unimodal distribution in binder jetting of SS316L, for higher density and preferred mechanical performance.

(ii) Bimodal groups were statistically denser than the unimodal groups, achieving an average increase in density of 20%.

(iii) Bimodal groups showed a higher UFS than the unimodal groups. Both the 30 + 10 μm and 40+10 μm groups had an average increase of 170% in UFS when compared to the 10 μm group, which saw the highest UFS out of all unimodal groups. According to the MD simulations, the fine powders in the bimodal groups filling the interstitial space provided extra bonds to strengthen the sintered part.

(iv) UFS followed the same trend observed in ReaxFF-MD simulation of bimodal powder size distribution. The improvements in mechanical strength was greater than predicted MD simulation results which could be attributed to higher number of fine particles in ASTM standard size samples when compared to MD simulations.

(v) In the bimodal groups of this study, statistical differences in density and UFS between the groups were not observed.

(vi) It was found that in unimodal powders, density decreases as particle size increases, despite the lack of statistical differences within the unimodal group. The 10 μm group had the highest density and was found to be the only group having statistically higher particle size compared to the 30 μm group (by 11.18%). This indicates that finer particles could result in higher density within unimodal particle sizes.

(vii) UFS followed a similar trend to density within the unimodal group; as particle size increases, UFS decreases. The 10 μm group was found to have statistically higher UFS than the rest of the unimodal groups.

(viii) Slight variation in the trend among observed unimodal density trend and across groups in UFS could have been caused by variability during sintering.

Future work should optimize the printing parameters of the bimodal groups to achieve the highest possible density and UFS. In addition to different sintering profiles and sample position, the effects of gas flow rate during sintering should be further investigated. Finally, the effect of powder binder interaction in bimodal distributions could be investigated both through MD simulation and experimental efforts, including in-process monitoring.

Acknowledgments

The authors acknowledge the support from the ExOne Company, The Pennsylvania State University, Tim Stecko, and Verder Scientific for their assistance.

Funding

This work was funded by NSF CAREER CMMI #1944120 and partially by Manufacturing PA program.

Conflict of interest

There are no conflicts of interest to declare.

Author contributions

Conceptualization: Ana Paula Clares, Adri C.T. van Duin, and Guha Manogharan
Formal analysis: Ana Paula Clares and Ryan Stebbins
Funding acquisition: Guha Manogharan
Investigation: Ana Paula Clares
Methodology: Ana Paula Clares
Project Administration: Guha Manogharan

Resources: Guha Manogharan
Supervision: Adri C.T. van Duin and Guha Manogharan
Writing – original draft: Ana Paula Clares, Yawei Gao, and Ryan Stebbins
Writing – review & editing: Adri C.T. van Duin and Guha Manogharan.

References

1. Mirzababaei S, Pasebani S, 2019, A review on binder jet additive manufacturing of 316L stainless steel. *J Manuf Mater Process*, 3: 82.

   https://doi.org/10.3390/JMMP3030082

2. Bai Y, Williams C, 2015, An exploration of binder jetting of copper. *Rapid Prototyp J*, 21: 177–185.

   https://doi.org/10.1108/RPJ-12-2014-0180

3. Liravi F, Vlasea M, 2018, Powder bed binder jetting additive manufacturing of silicone structures. *Addit Manuf*, 21: 112–124.

   https://doi.org/10.1016/j.addma.2018.02.017

4. Sama SR, Badamo T, Manogharan G, 2020, Case studies on integrating 3D sand-printing technology into the production portfolio of a sand-casting foundry. *Int J Met*, 14: 12–24.

   https://doi.org/10.1007/s40962-019-00340-1

5. Mariani M, Beltrami R, Brusa P, *et al.*, 2021, 3D printing of fine alumina powders by binder jetting. *J Eur Ceram Soc*, 41: 5307–5315.

   https://doi.org/10.1016/j.jeurceramsoc.2021.04.006

6. Cramer CL, Aguirre TG, Wieber NR, *et al.*, 2020, Binder jet printed WC infiltrated with pre-made melt of WC and Co. *Int J Refract Met Hard Mater*, 87: 105137.

   https://doi.org/10.1016/j.ijrmhm.2019.105137

7. Manogharan G, Kioko M, Linkous C, 2015, Binder jetting: A novel solid oxide fuel-cell fabrication process and evaluation. *JOM*, 67: 660–667.

   https://doi.org/10.1007/s11837-015-1296-9

8. Ke D, Bose S, 2018, Effects of pore distribution and chemistry on physical, mechanical, and biological properties of tricalcium phosphate scaffolds by binder-jet 3D printing. *Addit Manuf*, 22: 111–117.

   https://doi.org/10.1016/j.addma.2018.04.020

9. Martinez D, Bate C, Manogharan GP, 2020, Towards functionally graded sand molds for metal casting: Engineering thermo-mechanical properties using 3D sand printing. *JOM*, 72: 1340–1354.

   https://doi.org/10.1007/s11837-019-03975-x

10. Xia M, Sanjayan J, 2016, Method of formulating geopolymer for 3D printing for construction applications. *Mater Des*, 110: 382–390.

    https://doi.org/10.1016/j.matdes.2016.07.136

11. Rojas-Nastrucci EA, Nussbaum JT, Crane NB, *et al.*, 2017, Ka-band characterization of binder jetting for 3-D printing of metallic rectangular waveguide circuits and antennas. *IEEE Trans Microw Theory Tech*, 65: 3099–3108.

    https://doi.org/10.1109/TMTT.2017.2730839

12. Lecis N, Mariani M, Beltrami R, *et al.*, 2021, Effects of process parameters, debinding and sintering on the microstructure of 316L stainless steel produced by binder jetting. *Mater Sci Eng A*, 828: 142108.

    https://doi.org/10.1016/J.MSEA.2021.142108

13. Li M, Du W, Elwany A, *et al.*, 2019, Binder Jetting Additive Manufacturing of Metals: A Literature Review. Vol. 1. In: ASME 2019 14th International Manufacturing Science and Engineering Conference.

    https://doi.org/10.1115/MSEC2019-2994

14. Bai Y, Wagner G, Williams CB, 2015, Effect of bimodal powder mixture on powder packing density and sintered density in binder jetting of metals: In Annual International Solid Freeform Fabrication Symposium (2015), 62.

15. Li M, Du W, Elwany A, *et al.*, 2020, Metal binder jetting additive manufacturing: A literature review. *J Manuf Sci Eng Trans ASME*, 142: 090801.

    https://doi.org/10.1115/1.4047430/1084395

16. Gibson I, Rosen D, Stucker B, *et al.*, 2020, Binder jetting. In: *Additive Manufacturing Technologies*., Champaign: Springer International Publishing. p237–252.

17. Ziaee M, Tridas EM, Crane NB, 2017, Binder-jet printing of fine stainless steel powder with varied final density. *JOM*, 69: 592–596.

    https://doi.org/10.1007/s11837-016-2177-6

18. Meenashisundaram GK, Xu Z, Nai ML, *et al.*, 2020, Binder jetting additive manufacturing of high porosity 316L stainless steel metal foams. *Materials*, 13: 3744.

    https://doi.org/10.3390/MA13173744

19. Vogt J, Friedrich H, Stepanyan M, *et al.*, 2021, Improved green and sintered density of alumina parts fabricated by binder jetting and subsequent slurry infiltration. *Prog Addit Manuf*, 7: 161–171.

    https://doi.org/10.1007/S40964-021-00222-1

20. Porter Q, Pei Z, Ma C, 2022, Binder jetting and infiltration of metal matrix nanocomposites. *J Manuf Sci Eng*, 144: 074502.

    https://doi.org/10.1115/1.4053156

21. Kumar AY, Bai Y, Eklund A, *et al.*, 2018, The effects of hot isostatic pressing on parts fabricated by binder jetting additive manufacturing. *Addit Manuf*, 24: 115–124.

    https://doi.org/10.1016/J.ADDMA.2018.09.021

22. Kumar A, Bai Y, Eklund A, *et al.*, 2017, Effects of hot isostatic

pressing on copper parts fabricated via binder jetting. *Procedia Manuf*, 10: 935–944.

https://doi.org/10.1016/J.PROMFG.2017.07.084

23. Dahmen T, Henriksen NG, Dahl KV, *et al.*, 2021, Densification, microstructure, and mechanical properties of heat-treated MAR-M247 fabricated by binder jetting. *Addit Manuf*, 39: 101912.

https://doi.org/10.1016/J.ADDMA.2021.101912

24. Shrestha S, Manogharan G, 2017, Optimization of binder jetting using taguchi method. *JOM*, 69: 491–497.

https://doi.org/10.1007/s11837-016-2231-4

25. Du W, Singh M, Singh D, 2020, Binder jetting additive manufacturing of silicon carbide ceramics: Development of bimodal powder feedstocks by modeling and experimental methods. *Ceram Int*, 46: 19701–19707.

https://doi.org/10.1016/j.ceramint.2020.04.098

26. Du W, Ren X, Chen Y, *et al.*, 2018, Model Guided Mixing of Ceramic Powders with Graded Particle Sizes in Binder Jetting Additive Manufacturing. Vol. 1. In: ASME 2018 13th International Manufacturing Science and Engineering Conference. p9.

https://doi.org/10.1115/MSEC2018-6651

27. Du W, Roa J, Hong J, *et al.*, 2021, Binder jetting additive manufacturing: Effect of particle size distribution on density. *J Manuf Sci Eng*, 143: 091002.

https://doi.org/10.1115/1.4050306

28. Clares AP, Manogharan G, (2021), Discrete-element Simulation of Powder Spreading Process in Binder Jetting, and the Effects of Powder Size. In: ASME 2021 16th International Manufacturing Science and Engineering Conference.

29. Standard, ASTM, 2012, ISO/ASTM 52900: 2015 Additive manufacturing-General principles-terminology. ASTM F2792-10e1.

30. Bai Y, Wagner G, Williams CB, 2017, Effect of particle size distribution on powder packing and sintering in binder jetting additive manufacturing of metals. *J Manuf Sci Eng Trans ASME*, 139: 081019.

https://doi.org/10.1115/1.4036640

31. Chen H, Zhao YF, 2016, Process parameters optimization for improving surface quality and manufacturing accuracy of binder jetting additive manufacturing process. *Rapid Prototyp J*, 22: 527–538.

https://doi.org/10.1108/RPJ-11-2014-0149/FULL/PDF

32. Utela B, Storti D, Anderson R, *et al.*, 2008, A review of process development steps for new material systems in three dimensional printing (3DP). *J Manuf Process*, 10: 96–104.

https://doi.org/10.1016/J.JMAPRO.2009.03.002

33. Mostafaei A, Elliott AM, Barnes JE, *et al.*, 2020, Binder jet 3D printing-Process parameters, materials, properties, and challenges. *Prog Mater Sci*, 119: 100707.

https://doi.org/10.1016/j.pmatsci.2020.100707

34. Gao Y, Clares AP, Manogharan G, *et al.*, 2022, A reactive molecular dynamics study of bi-modal particle size distribution in binder-jetting additive manufacturing using stainless-steel powders. *Phys Chem Chem Phys*, 24: 11603–11615.

https://doi.org/10.1039/D2CP00630H.

35. Miyanaji H, Momenzadeh N, Yang L, 2019, Effect of powder characteristics on parts fabricated via binder jetting process. *Rapid Prototyp J*, 25: 332–342.

https://doi.org/10.1108/RPJ-03-2018-0069/FULL/PDF

36. Verlee B, Dormal T, Lecomte-Beckers J, 2013, Density and porosity control of sintered 316L stainless steel parts produced by additive manufacturing. *Powder Metallurgy*, 55: 260–267.

https://doi.org/10.1179/0032589912Z.00000000082

37. Miao G, Du W, Moghadasi M, *et al.*, 2020, Ceramic binder jetting additive manufacturing: Effects of granulation on properties of feedstock powder and printed and sintered parts. *Addit Manuf*, 36: 101542.

https://doi.org/10.1016/j.addma.2020.101542

38. Ji CH, Loh NH, Khor KA, *et al.*, 2001, Sintering study of 316L stainless steel metal injection molding parts using Taguchi method: Final density. *Mater Sci Eng A*, 311: 74–82.

https://doi.org/10.1016/S0921-5093(01)00942-X

39. Sridhar TM, Mudali UK, Subbaiyan M, 2003, Sintering atmosphere and temperature effects on hydroxyapatite coated type 316L stainless steel. *Corros Sci*, 45: 2337–2359.

https://doi.org/10.1016/S0010-938X(03)00063-5

40. Jost EW, Miers JC, Robbins A, *et al.*, 2021, Effects of spatial energy distribution-induced porosity on mechanical properties of laser powder bed fusion 316L stainless steel. *Addit Manuf*, 39: 101875.

https://doi.org/10.1016/J.ADDMA.2021.101875

41. Masuo H, Tanaka Y, Morokoshi S, *et al.*, 2017, Effects of defects, surface roughness and HIP on fatigue strength of Ti-6Al-4V manufactured by additive manufacturing. *Procedia Struct Integr*, 7: 19–26.

https://doi.org/10.1016/J.PROSTR.2017.11.055

42. Du W, Ren X, Pei Z, *et al.*, 2020, Ceramic binder jetting additive manufacturing: a literature review on density. *J Manuf Sci Eng*, 142: 040801.

https://doi.org/10.1115/1.4046248

Author Guidelines

Before submitting for publication, please ensure that your paper and other supplementary files have been prepared and formatted in accordance with the guidelines below.

Submission structure, general style and format

Materials Science in Additive Manufacturing requests that every new submission should be made and accompanied by 3 separate core files, namely manuscript, title page and back matter, and cover letter, whereas resubmission of revision file should be accompanied by 4 separate core files, namely manuscript, title page and back matter, cover letter, and response/rebuttal letter (collectively known as the revision file). Provision of supplementary files and/or confidential accessory files is optional or dependent on the nature of study and findings relevance. The table below briefly summarizes the type of files in a submission, their respective requirements and included items:

Type of file	File format	Requirements	Included items
(1) Manuscript	DOC or DOCX	- Use 1.5-spacing and format text in one column - Use page numbers and continuous line numbers - Font and size: Times New Roman, 12 - Insert tables and figures at the back of manuscript	- Manuscript title - Abstract (for original research article, review article and perspective article) - Keywords - Text - References - Tables (including caption and legend) - Figures (including caption and legend)
(2) Title page and back matter *	DOC or DOCX	- Use 1.5-spacing and format text in one column - Font and size: Times New Roman, 12	**<u>On the first page (title page):</u>** - Manuscript title - Authorship list (first and last names must be spelled out) - Author's affiliation, including department, institution, city, state, postal code, and country (indicated with superscript number) - Corresponding author information, including asterisk indication, mailing address and email - Indication of equally contributing authors (if any) with dagger symbol **<u>On the second page (back matter):</u>** - Acknowledgments - Funding - Conflict of interest (mandatory) - Author contributions (formatted as per CRediT) - Further disclosure about presentation of essential findings in conference(s) and/or upload of the paper to a preprint server
(3) Cover letter	DOC or DOCX	- Use 1.5-spacing and format text in one column - Font and size: Times New Roman, 12	- A brief explanation of what was previously known, the conceptual advancement with the findings and its significance to broad readership - A statement that "neither the manuscript nor any significant part of it is under consideration for publication elsewhere or has appeared elsewhere in a manner that could be construed as a prior or duplication of the same work" with author confirmation - If any, associated accession numbers or DOIs of the corresponding preprint version of the submission - [Optional] Name, affiliation and email address of up to 4 academically qualified (recommended) reviewers and/or name and affiliation of individuals who should be excluded from reviewing the submitted works on the grounds of conflict of interest
(4) Supplementary files		- Supplementary files should **not exceed 20 MB** in total (15MB individual file limit)	

- Supplementary tables or figures	DOC or DOCX	- Use 1.5-spacing and format text in one column - Use page numbers and continuous line numbers - Font and size: Times New Roman, 12 - Include both supplementary tables (editable) and figures (in JPEG, PNG or TIFF format) in the same file	- Supplementary tables - Supplementary figures
- Data set	XLS or XLSX	- All data should be neatly presented using consistent fonts	
- Videos	MP4	- If necessary, trim the video clip to focus only on essential parts, such as experimental procedures and findings or observation that can only be demonstrated using video(s) - Avoid unnecessary narrations that can be presented in written form	
(5) Confidential accessory files			
- Sample consent form (for human research only)	DOC, DOCX, PDF, JPEG, PNG or TIFF	- This is a sample, unsigned consent form that should bear the institution letterhead	
- Research ethics proof (for human and/or animal research only)	DOC, DOCX, PDF, JPEG, PNG or TIFF	- Ideally, this document should contain the essential research ethics information, such as ethics approval identifiers and the name of Institutional Ethics Review Board or Institutional Review Board - The research described in **original research article** should match the proposed research or significantly fit within the framework of the specification stipulated in the research ethics proof	
(6) Response/rebuttal letter (only applicable to revisions)	DOC or DOCX	- All comments/feedback and responses/rebuttals must be clearly and concisely presented	- Reviewers' comments and feedback - Authors' responses

[#] Ideally, all information given in the title page and back matter file, except for the manuscript title, should remain the same from the point of submission to paper acceptance. Thus, authors are responsible to ensure that all information therein is accurate before making submission. Refer to **Authorship and Author Information** for more information about *Materials Science in Additive Manufacturing*'s authorship policy.

Submitting authors should refer to the relevant sections in the following for more detailed information.

Author metadata during submission

During the submission process, the submitting author must ensure that all particulars of author information, including full name, affiliation, and email address, are given in the author metadata column of the submission system. These particulars must exactly reflect those on the title page of the submission; this includes the author order of the authorship list. Provide authors' ORCID ID, if available.

Article types

(1) Original research article

An original research article is based on original, basic and applied research and/or analysis. This type of article aims to describe significant and novel research. Authors of original research articles must confirm that the essential findings presented have never been published or under consideration elsewhere.

This article type typically has at least 5 tables and/or figures in total, approximately 40 references, and 7,000 words (inclusive of Abstract and References).

(2) Review article

A review article provides scholarly survey as well as balanced summarization and highlights of recent developments in a research field or emerging/future trends. Authors should ensure that all perspectives from different works are linked in balanced and cohesive manner, taking into consideration different schools of thought.

This article type typically has at least 5 tables and/or figures in total, approximately 70 references, and 7,000 words (inclusive of Abstract and References).

(3) Perspective article

A perspective article contains the author's scholarly opinions on a particular subject area or topic. Unlike a review, a perspective article covers a more specific part of the field, aiming to provide new insights into the subject matter. However, these perspectives or opinions should be objective in line with the spirit of academia. A good perspective piece should stimulate further discussions and initiate novel experiments.

This article type typically has 5 tables and/or figures in total, approximately 70 references, and 7,000 words (inclusive of Abstract and References).

(4) Letters

This article type is a collection of unsolicited letters from the readers who wish to comment on specific articles published in *Materials Science in Additive Manufacturing* or another field-related journal. Alternatively, a letter can be written on an unrelated topic of interest to the journal's readership.

Ideally, a letter should present an in-depth, scholarly re-analysis of a previously published article in *Materials Science in Additive Manufacturing* or in another field-related journal, accompanied by the reader's constructive insights and comments. Letters containing new ideas, supporting data or data criticizing the indicated article may be subjected to peer review at editors' discretion. Authors should specify the intended recipient of the letters, i.e., Editor or specific author(s).

This article type typically has no more than 3 tables and/or figures in total, no more than 20 references, and 2,000 words (inclusive of References). No Abstract is required.

(5) Editorial

An editorial piece is a solicited, concise commentary that highlights prominent topics in particular issue. Alternatively, an editorial represents the official opinions of the editors on the journal or special issue.

An editorial piece should not exceed 1,000 words (inclusive of References). Typically, an Abstract is not required and only 1 figure or table is allowed.

(6) Erratum

Authors should contact the editors of *Materials Science in Additive Manufacturing* (editor.msam@whioce.com) if certain errors made by the journal are found. The editors will evaluate the impact of the errors and decide on the appropriate course of action. Any corrections to a paper are published at the sole discretion of the editors.

(7) Corrigendum

Authors should contact the editors of *Materials Science in Additive Manufacturing* (editor.msam@whioce.com) if certain errors made by the authors are found. The editors will evaluate the impact of the errors and decide on the appropriate course of action. Any corrections to a paper are published at the sole discretion of the editors.

Language

All submissions must be written entirely in good American English. Spelling and use of punctuations should conform to conventions in American English. Clarity and conciseness are critical requirements for publications; therefore, submissions that are not clearly written will be returned to authors. Authors must ensure that their manuscripts are submit-ready or publish-ready before making submission. The articles published in *Materials Science in Additive Manufacturing* are in adherence with the publishable standards of academic and scientific writing.

Please note that utilizing a language editing service is not a guarantee of acceptance.

Letter capitalization

Use sentence case capitalization in all aspects of the submission. In sentence case, most major and minor words are lowercase (proper nouns, including name of organizations and name of guidelines, are an exception in that they are always capitalized for the first letter of each word, except for minor words, such as conjunctions and short prepositions). The first letter of the first word should always be uppercase.

Manuscript title

The title should capture the conceptual significance for a broad audience. The title should not be more than 50 words and should be able to give readers an overall view of the paper's significance. Titles should avoid using uncommon jargons, abbreviations and punctuation.

Abstract

The purpose of abstract is to provide sufficient information and capture essential findings and/or messages of the paper. The length of an abstract should be in the range of 200-400 words. The abstract should be **unstructured**. Abstract is only needed in original research article, review article, and perspective article.

Keywords

Each submission should be accompanied by 3-6 keywords. Avoid using abbreviations and acronyms in keywords, unless they are established standard keywords. Separate keywords with semi-colons (i.e, term1; term2; term3).

Abbreviations and acronyms

Define abbreviations and acronyms upon their first appearance, **separately**, in the abstract, main text, table legends, and figure captions and legends.

Sections in article

(1) Section headings

Section headings should be in boldface. Examples of section headings of different levels are shown in the following:

Primary level : **1. Heart disease**

Secondary level : **1.3. Risk factors for heart disease**

Tertiary level : **1.3.2. Hypertension**

Authors are suggested **NOT** to introduce further sub-sections after the tertiary level section (e.g., **1.3.2.1. High-salt diet**).

(2) Special sectioning requirements for an original research article

- **Introduction.** The introduction should provide a background that gives a broad readership an overall outlook of the field and the research performed. It tackles a problem and states its important regarding with the significance of the study. Introduction can conclude with a brief statement of the aim of the work and a comment about whether that aim was achieved.

- **Materials and Methods.** This section provides the general experimental design and methodologies used. The aim is to provide enough detail to for other investigators to fully replicate the results. It is also required to facilitate better understanding of the results obtained. Protocols and procedures for new methods must be included in detail for the reproducibility of the experiments. Informed consent should be obtained from patients or parents before the experiments start and should be mentioned in this section. For human and/or research, research ethics information, such as ethics approval identifiers and the name of Institutional Ethics Review Board or Institutional Review Board, should be indicated in this section.

- **Results.** This section focuses on the results and findings of the experiments performed. After (statistical) analysis, all results, including tables and figures, must be neatly presented. If necessary, this section can be sub-divided into multiple topical sub-sections.

- **Discussion.** This section should provide the significance of the results and identify the impact of the research in a broader context. It should not be redundant or similar to the content of the results section.

- **Conclusion.** Use this section for interpretation only, and not to summarize information already presented in the text or abstract.

It is acceptable to merge both Results and Discussion as a single section.

Unit of measurements

Use SI units.

Data and image processing

Post-acquisition processing of images, photos and figures should be kept minimum to ensure that the final figures accurately reflect the original data as it was captured and/or produced. Any alterations should be applied to the entire image. Any kind of alteration, including but not limited to brightness, contrast and color balance, has to be clearly stated in the figure legend and in Materials and Methods section. For simulated or model figures, the software used for production, editing, and/or processing should be mentioned. Presenting images in the same figure must be made apparent and should be explicitly indicated in the appropriate figure legends.

Data comparisons should only be made from comparative experiments (or data from the same experiment). Same piece of data or figure should not be used in multiple instances, unless the images/data describe different aspects of the same experiment (reasons must be stated, wherever appropriate, in this regard). If inappropriate image/data manipulation is identified after publication, the editors reserve the right to ask for the original data and, if that is not satisfactory, to issue a correction or retract the paper, as appropriate.

Chemical compounds

Materials Science in Additive Manufacturing requires authors to fulfill the requirements below while reporting and/or describing a chemical compound in articles:

Scenario	Requirements
Naming chemical compounds	Use either IUPAC conventions or common names such as cholesterol and cephalosporins
Reporting a new chemical compound	Provide the exact structure of the compound as well as sufficient data regarding the purity and identity of the compound
Reporting the use of a known chemical compound	Provide sufficient data regarding the source, purity and identity of the compound

Figures

Include all figures, including photographs, scanned images, graphs, charts and schematic diagrams, at the back of manuscript. Avoid unnecessary decorative effects (e.g., 3D graphs) and minimize image processing (e.g., changes in brightness and contrast applied uniformly for the entire figure should be avoided or minimized). All images should be set against white background.

All figures should be numbered (e.g., **Figure 1**, **Figure 2**) in boldface. Label all figures (e.g., axis, structures), and add caption (a brief title) and legend as a description of the illustration below each figure. Explain all symbols and abbreviations used. Each figure should have a brief title (also known as caption) that describes the entire figure without citing specific panels, followed by a legend, which is either the description of each panel or further description about the single image. Identify each panel with uppercase letters in parenthesis (e.g. (A), (B), (C), etc.) Figures must be cited in chronological manner in the text.

The preferred file formats for any separately submitted figure(s) are JPEG, PNG and TIFF. All figures should be of optimal resolution. Optimal resolutions preferred are 300 dots per inch (dpi) for RBG colored, 600 dpi for grayscale and 1,200 dpi for line art. Although there is no file-size limitation imposed, authors are highly encouraged to compress their figures to an ideal size without unduly affecting the legibility and resolution of figures.

If necessary, the editors may request author(s) to supply high-resolution and/or unprocessed images after submission or paper acceptance for pre-screening/review and production purposes, respectively.

Tables

Include all tables at the back of manuscript. Editable tables created using Microsoft Word are preferred. A table should be accompanied by a caption on top of it. Captions and legends should be concise. All tables should be numbered (e.g. **Table 1**, **Table 2**) in boldface. Explain all symbols and abbreviations used. Tables must be cited in chronological manner in the text.

Lists and math formulae

Lists and math formulae should be properly aligned and included within the main body of the manuscript. List them using Roman numerals in parenthesis (e.g. (I), (II), (III), (IV), etc.) Lists and math formulae must be cited in chronological manner in the text.

Lists and math formulae should be given in editable text and not as images. Use the solidus (/) for small fractional terms, e.g., X/Y. In principle, variables should be italicized. Powers of e are often more conveniently denoted by exp.

Footnotes

Do not use footnotes.

In-text citations

Reference citations in the text should be numbered consecutively in superscript square brackets. Some examples:

- Negotiation research spans many disciplines[3,4].
- This result was later contradicted by Becker and Seligman[5].
- This effect has been widely studied[1–3,7].

Do not include citations in the Abstract.

Personal communications and unpublished works can only be used in the manuscript and are not to be placed in the References section. Authors are advised to limit such usage to the minimum. These should be made identifiable by stating the authors, year of personal communications or unpublished works, and the words “personal communication” or “unpublished” in parenthesis, e.g., (Smith J, 2000, unpublished).

References

This section is compulsory and should be placed at the end of all manuscripts. Do not use footnotes or endnotes as a substitute for a reference list. The list of references should only include works that are cited in the text and that have been published or accepted for publication. Personal communications and unpublished works should be excluded from this section.

Authors being referenced are listed with their surname or last name followed by their initials. All references should be numbered (e.g. 1, 2, 3, and so on) and sequenced according to the order they appear as the in-text citations. References (especially journal article’s) should follow the general pattern: author(s), followed by year of publication, title of publication, abbreviated journal name in italics, volume number, issue number in parenthesis and lastly, page range or article ID. If the referred article has more than 3 authors, list only the first 3 authors and abbreviate the remaining authors as italicized “*et al*.” (meaning "and others"). Use of DOI is highly encouraged; include DOI, if available, after the page range or article ID. Examples of references for different types of publications are as follows:

(1) Journals

Journal article (print) with 1-3 authors:

Younger P, 2004, Using the internet to conduct a literature search. *Nurs Stand*, 19(6): 45–51.

Journal article (print) with more than 3 authors:

Gamelin FX, Baquet G, Berthoin S, *et al*., 2009, Effect of high intensity intermittent training on heart rate variability in prepubescent children. *Eur J Appl Physiol,* 105(1): 731–738.

Journal article (online) with 1-3 authors:

Jackson D, Firtko A, Edenborough M, 2007, Personal resilience as a strategy for surviving and thriving in the face of workplace adversity: A literature review. *J Adv Nurs*, 60(1): 1–9. http://doi.org/10.1111/j.1365-2648.2007.04412.x

Journal article (online) with more than 3 authors:

Hargreave M, Jensen A, Nielsen TSS, *et al*., 2015, Maternal use of fertility drugs and risk of cancer in children — A nationwide population-based cohort study in Denmark. *Int J Cancer*, 136(8): 1931–1939. http://doi.org/10.1002/ijc.29235

(2) Books

Book with 1-3 authors:

Schneider Z, Whitehead D, Elliott D, 2007, *Nursing and Midwifery Research: Methods and Appraisal for Evidence-based Practice*, 3rd edn, Elsevier Australia, Marrickville, NSW, 112–130.

Book with more than 3 authors

Davis M, Charles L, Curry MJ, *et al*., 2003, *Challenging Spatial Norms*, Routledge, London, 12–30.

Chapter or article in book

Knowles MS, (eds) 1986, Independent study, in *Using Learning Contracts*, Jossey-Bass, San Francisco, 89–96.

(3) Preprints

Preprint article with 1-3 authors:

Ulgen A, Gurkut O, Li W, 2019, Potential Predictive Factors for Breast Cancer Subtypes from a North Cyprus Cohort Analysis. *medRxiv*. https://doi.org/10.1101/19010181

Preprint article with more than 3 authors:

Wu S, Sun P, Li R, *et al*., 2020, Epidemiological Development of Novel Coronavirus Pneumonia in China and Its Forecast. *medRxiv*. https://doi.org/10.1101/2020.02.21.20026229

(4) Others

Proceedings of meetings and symposiums, conference papers:

Chang SS, Liaw L, Ruppenhofer J, (eds) 2000, *Proceedings of the twenty-fifth annual meeting of the Berkeley Linguistics Society, February 12–15, 1999: General session and parasession on loan word phenomena*. Berkeley Linguistics Society, Berkeley, 12–13.

Conference proceedings (from electronic database):

Wang T, Cook C, Derby B, 2009, Fabrication of a glucose biosensor by piezoelectric inkjet printing. *Proceedings of the Third International Conference on Sensor Technologies and Applications, 2009 (SENSORCOM-M'09)*, 82–85.

Online document with author names:

Este J, Warren C, Connor L, *et al*., 2008, Life in the clickstream: The future of journalism, Media Entertainment and Arts Alliance, viewed May 27, 2009, http://www.alliance.org.au/documents/ foj_report_final.pdf

Online document without author name:

Developing an argument, n.d., viewed March 30, 2009, http://web.princeton.edu/sites/writing/Writing_Center/WCWritingResources.htm

Thesis/Dissertation:

Gale L, 2000, The relationship between leadership and employee empowerment for successful total quality management, thesis, *Australasian Digital Thesis database*, University of Western Sydney, 110–130.

Standards:

Standards Australia Online, 2006, Glass in buildings: selection and installation, AS 1288-2006, amended January 31, 2008, *SAI Global database*, viewed May 19, 2009.

Government report:

National Commission of Audit, 1996, *Report to the Commonwealth Government*, Australian Government Publishing Service, Canberra.

Government report (online):

Department of Health and Ageing, 2008, Ageing and aged care in Australia, viewed November 10, 2008, http://www.health.gov.au/internet/main/publishing.nsf/Content/ageing

No author:

Guide to agricultural meteorological practices, 1981, 2nd ed, Secretariat of the World Meteorological Organization, Geneva, 10–20.

Note: When referencing an entry from a dictionary or an encyclopedia with no author there is no requirement to include the source in the reference list. In these cases, only cite the title and year of the source in-text. For an authored dictionary/encyclopedia, treat the source as an authored book.

Acknowledgments*

*This should be included in the title page and back matter file

This is an optional section where authors can acknowledge people and/or institutions that provided non-financial support and/or helped with the research and/or preparation of the manuscript. Examples of non-financial support include externally-supplied equipment/biological sources, writing assistance, administrative support, and contributions from non-authors.

Funding*

*This should be included in the title page and back matter file

Authors should declare all financial support and sources that were used to perform the research, analysis, and/or article publication. Financial supports are generally in the form of grants, royalties, consulting fees and others.

Conflict of interest*

*This should be included in the title page and back matter file

At the time of submission, authors must declare any (potential) conflicts or competing interests with any institutes, organizations or agencies that might influence the integrity of results or objective interpretation of their submitted works. For more information, see our **Conflict of Interest** policy.

Author contributions*

*This should be included in the title page and back matter file

This section should be included in original research articles and review articles. In *Materials Science in Additive Manufacturing*, we encourage authors to use **Contributor Roles Taxonomy (CRediT)** in describing each contributor's specific contribution to the scholarly output in the Author Contributions section.

Definitions of each contributor role as per CRediT are as follows:

Contributor role	Definition
Conceptualization	Ideas; formulation or evolution of overarching research goals and aims.
Data curation	Management activities to annotate (produce metadata), scrub data and maintain research data (including software code, where it is necessary for interpreting the data itself) for initial use and later re-use.
Formal analysis	Application of statistical, mathematical, computational, or other formal techniques to analyze or synthesize study data.
Funding acquisition	Acquisition of the financial support for the project leading to this publication.
Investigation	Conducting a research and investigation process, specifically performing the experiments, or data/evidence collection.
Methodology	Development or design of methodology; creation of models.
Project administration	Management and coordination responsibility for the research activity planning and execution.
Resources	Provision of study materials, reagents, materials, patients, laboratory samples, animals, instrumentation, computing resources, or other analysis tools.
Software	Programming, software development; designing computer programs; implementation of the computer code and supporting algorithms; testing of existing code components.
Supervision	Oversight and leadership responsibility for the research activity planning and execution, including mentorship external to the core team.
Validation	Verification, whether as a part of the activity or separate, of the overall replication/reproducibility of results/experiments and other research outputs.
Visualization	Preparation, creation and/or presentation of the published work, specifically visualization/data presentation.
Writing – original draft	Preparation, creation and/or presentation of the published work, specifically writing the initial draft (including substantive translation).
Writing – review & editing	Preparation, creation and/or presentation of the published work by those from the original research group, specifically critical review, commentary or revision – including pre- or post-publication stages.

Below shows a sample Author Contributions section written based on the CRediT:

Conceptualization: Ali Jackson, Helen Meyer
Investigation: Ali Jackson, Tom Lewis-Hans, Han Xiang
Formal analysis: Han Xiang
Writing – original draft: Ali Jackson
Writing – review & editing: Helen Meyer, Joshua O'Brien

Supplementary files

This section is optional and contains all materials and figures that are excluded from the manuscript. These materials, figures or additional information are relevant to the manuscript but remain non-essential to readers' understanding of the manuscript's main content. All supplementary information should be submitted as a separate file during submission.

Supplementary figures and tables should be submitted in a single, separate supplementary file, and must be numbered, for example, **Figure S1** and **Table S1**. All tables must be editable (preferably created from Microsoft Word). The acceptable formats of images and illustrations used in figures are JPEG, PNG and TIFF. Citations of these items must be appropriately referenced in the manuscript in chronological manner,

for instance, “Additional information can be found in **Table S1**.” Note the additional letter **S** helps distinguish the normal from supplementary items.

Data set file are usually prepared using Microsoft Excel (in XLS or XLSX format).

Videos (MP4 format), with a constituent maximum size of 15 MB, can be uploaded as part of the supplementary file.

Revision and response/rebuttal letter

If the editorial decision for a submission is major revision or minor revision, authors are advised to revise the manuscript (and possibly, the supplementary files) as per the review reports and resubmit the revision file, including the manuscript, title page and back matter, cover letter, and response/rebuttal letter, before the due date.

Revisions should be done on the latest version of the manuscript (or in some rare cases, edited manuscript provided by the editor) with the track change on. The revisions made should be described and/or clarified in the response/rebuttal letter; ideally, explanation about the revisions should be made clear with the help of page number and line number. If authors do not agree with reviewers’ comments and suggestions, rebut their points with strong evidence and reasonable arguments.

Materials Science in Additive Manufacturing

Special Issue Alerts

Invitation for Special Issue Proposals

Organizing and editing for a Special Issue helps Guest Editors gain editorial experience and improve academic profile, in addition to being a part of organizing scientific communication of contemporary topics.

If you are published researcher and have an idea for a Special Issue, please write in via email to our Special Issue Commissioning Editor (felicia_wang@whioce.com). Please provide your CV, professional profile page and a topic of interest in your email. Our colleague will guide you in the process of writing a Special Issue proposal.

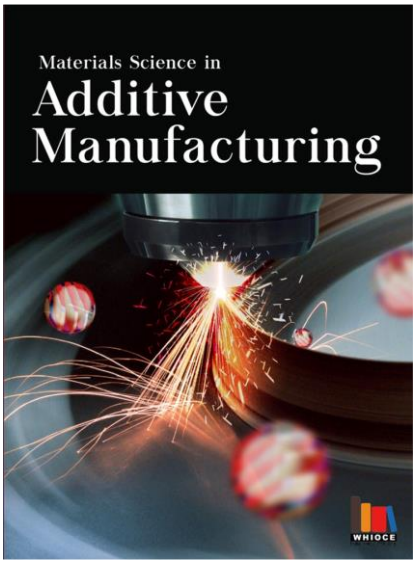

Frequently Asked Questions

1. **Are Special Issue submissions processed in the same way how Regular Issue papers are being pre-screened and reviewed?**
   Yes, all full-length article submissions to a Special Issue will go through the same editorial and peer-review process. The distinct difference here is that the Guest Editors will replace the usual editors and get involved in the making professional decisions on papers after peer review. Note that the specific roles of a Guest Editor could vary across Special Issues.

2. **How many Guest Editors are required to organize a Special Issue?**
   There is no fixed number; however, we suggest no more than 4 Guest Editors per Special Issue. More importantly, all Guest Editors should have excellent publication track records and demonstrated expertise in the topic(s) being proposed.

3. **Is the Special Issue governed by important deadlines?**
   Yes.

Benefits of Being A Guest Editor

- A chance to get involved in the conception and development of a specialty, contemporary topic that is of interest to the readers
- A chance to expand your professional network to the scholars and researchers who are similarly involved in the research of specialty topic
- A chance to hone your editorial skills
- A chance to gain first-hand experience of editing a thematic issue publication, which is a very valuable experience for those who aspire to edit their own journal in future
- A chance to improve your academic profile and help establish your academic influence within your discipline

OUR JOURNALS

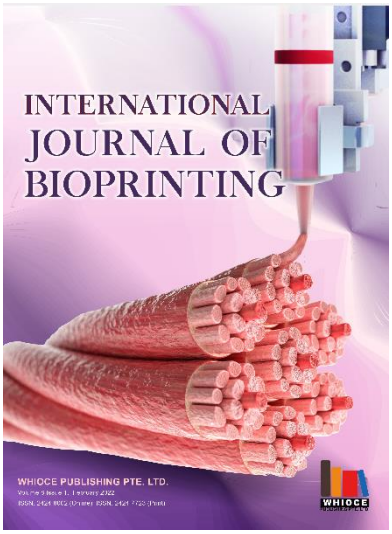

International Journal of Bioprinting is an international journal covering the technology, science and clinical application of the broadly defined field of bioprinting. Bioprinting is defined as the use of 3D printing technology with materials that incorporate viable living cells or biological elements to produce tissue or biotechnological products.

We are interested in the scientific topics spanning all stages of bioprinting process from concept creation to fabrication and beyond. Knowledge generated in these researches must be related to bioprinting.

The journal publishes original research articles on basic and applied research as well as associated social implications of this research. The journal also publishes brief commentaries and reviews. Articles focusing on the practical applications of 3D-printed products are similarly welcome.

The *Journal of Clinical and Translational Research* is an open access, peer-reviewed, multidisciplinary scientific journal that publishes studies with at least an ex vivo, in vivo, or clinical component. The published research is centered on any clearly defined clinical problem, which may comprise a disease or the basis of disease, a form of therapy or intervention, and clinical diagnostics or prognostics. Articles (original research, reviews, technical reports, medical hypotheses, commissioned articles, special issue articles, and editorials) are published continuously online. The key features of this journal are:

- Open access
- No submission or publication fees
- Reputable international editorial board
- Easy and fast submissions - no formatting rules ("your paper, your way")
- No word count or reference restrictions
- Double blind review process to minimize bias
- Rapid online publication of articles upon acceptance
- Outlet for academic institutions and industry

Start a new journal

Write to us via email if you are interested to start a new journal with Whioce Publishing. Please attach your CV, professional profile page and a brief pitch proposal in your email. We shall inform you of our decision whether we are interested to collaborate in starting a new journal.

Contact: info@whioce.com

Whioce Publishing Pte. Ltd.
Publishing Office:
8 Burn Road, #15-03 Trivex, Singapore 369977.

Editorial Office:
30-2, Jalan BS 1/2, Olive Hill Business Park, 43300 Seri Kembangan, Selangor. Malaysia.

msam.editor@whioce.com

https://msam.whioce.com/index.php/MSAM/index